Fakultät für Medizin

The role of metavinculin in force transduction at cell adhesion sites

Verena Anna Maria Caterina Kanoldt

Vollständiger Abdruck der von der Fakultät für Medizin der Technischen Universität München zur Erlangung des akademischen Grades eines Doktors der Naturwissenschaften genehmigten Dissertation.

Vorsitzender: Prof. Dr. Heiko Lickert

Prüfende der Dissertation:

1. Prof. Dr. Dr. Stefan Engelhardt
2. Prof. Dr. Matthias Rief

Die Dissertation wurde am 07.04.2021 bei der Technischen Universität München eingereicht und durch die Fakultät für Medizin am 10.08.2021 angenommen.

DISSERTATION ZUR ERLANGUNG DES DOKTORGRADES DER FAKULTÄT FÜR MEDIZIN AN DER TECHNISCHEN UNIVERSITÄT MÜNCHEN

THE ROLE OF METAVINCULIN IN FORCE TRANSDUCTION AT CELL ADHESION SITES

Verena Anna Maria Caterina Kanoldt

2021

Durchgeführt am Max-Planck-Institut für Biochemie

und der Westfälischen Wilhelms Universität Münster

max-planck-institut für biochemie

WWU

ZUSAMMENFASSUNG

Das Zelladhäsionsprotein Vinkulin wird ubiquitär exprimiert und spielt eine zentrale Rolle in der Regulierung der Kraftübertragung. Im Vergleich zu Vinkulin weist seine muskelspezifische Spleißisoform Metavinkulin eine unterschiedlich ausgeprägte Aktivität in der Aktinfilamentbindung und -bündelung auf. Weiterhin wurde die Deaktivierung und Mutation von Metavinkulin mit Kardiomyopathien assoziiert, was zusammen auf eine spezifische Rolle der Spleißisoform in der Kraftfortpflanzung hinweist. Indessen bleibt die Funktion von Metavinkulin in der Mechanotransduktion und seine Rolle in Herzmuskelstörungen noch unklar. In dieser Dissertation wird die Mechanik von Metavinkulin mit einem Set von FRET-basierte Kraftsensoren in Zellen untersucht, die einen Kraftbereich von 1-11 pN abdecken. Die FLIM-Experimente in lebenden Zellen zeigen, dass Metavinkulinmoleküle unter größeren Kräften stehen als Vinkulin, wohingegen die mechanische Last nur von einem kleineren Anteil der Metavinkulinbindungen getragen wird. Dieser Spleißisoform-spezifische Unterschied in der Kraftübertragung ist unabhängig von der Aktivierung von (Meta)Vinkulin und verändert die Kraftweiterleitung durch das Fokaladhäsionsprotein Talin. Zusätzlich wurde die Folge des Verlustes oder der R975W Mutation in Metavinkulin in zwei entsprechenden Mausmodellen untersucht. Unerwarteterweise zeigten die Metavinkulin Knockout-Mäuse eine normale hypertrophe Antwort unter normalen und pathologischen Konditionen eines Quer Aorta Verengung Modells (TAC). Nicht destotrotz führte die R975W Mutation zu einem reduzierten mutierten Metavinculin-Proteingehalt in verschiedenen Muskelgeweben, was auf einen potentiell schädlichen Effekt der Mutation für die Integrität des Muskelgewebes hindeutet. Zusammen weisen die Ergebnisse darauf hin, dass die Kraftübertragung in Zelladhäsionen durch die zwei Vinkulinspleißisoformen unterschiedlich moduliert wird, während Metavinkulin eine subtilere Rolle in der Herzmuskelfunktion zu spielen scheint als zuvor angenommen.

SUMMARY

Vinculin is a ubiquitously expressed cell adhesion protein which plays a pivotal role in the regulation of force transduction. Its muscle-specific splice isoform metavinculin displays a distinct actin filament binding and bundling activity as compared to vinculin. Furthermore, deletion and mutation of metavinculin were associated with cardiomyopathies, together indicating a specific role of the splice isoform in force propagation. However, the function of metavinculin in mechanotransduction and its role in heart muscle disorders still remains unclear. In this thesis the mechanics of metavinculin were studied in cells using a set of FRET-based tension sensors covering a force range of 1-11 pN. The live cell FLIM experiments revealed that metavinculin molecules bear higher molecular forces than vinculin, whereas only a smaller fraction of metavinculin linkages carries the mechanical load. This splice isoform-specific difference in force transduction is independent of (meta)vinculin activation and alters force propagation across the focal adhesion protein talin. Additionally, the consequence of metavinculin loss and R975W mutation was analyzed in two respective mouse models. Unexpectedly, metavinculin knock-out animals displayed a normal hypertrophic response under normal and pathological conditions of a transverse aortic constriction model. Nevertheless, the introduction of the R975W mutation led to reduced protein levels of mutated metavinculin in several muscle tissues, suggesting a potential detrimental effect of the mutation for muscle tissue integrity. Together, these results indicate that force transduction in cell adhesion sites is differentially modulated by the two vinculin splice isoforms, whereas metavinculin seems to play a more subtle role than previously anticipated in heart muscle function.

LIST OF PUBLICATIONS

Kanoldt, Verena; Fischer, Lisa; Grashoff, Carsten (2019): Unforgettable force - crosstalk and memory of mechanosensitive structures. In *Biol Chem* 400 (6), pp. 687–698. DOI: 10.1515/hsz-2018-0328.

Kanoldt, Verena; Kluger, Carleen; Barz, Christiane; Schweizer, Anna-Lena; Ramanujam, Deepak; Windgasse, Lukas et al. (2020): Metavinculin modulates force transduction in cell adhesion sites. In *Nat Commun* 11 (1), p. 6403. DOI: 10.1038/s41467-020-20125-z.

ABBREVIATIONS

aa	amino acid
α-cat	α-catenin
Actn1	α-actinin
Acta1	actin alpha 1
AFM	atomic force microscopy
AJ	adherens junction
Amp	ampicillin
APS	ammonium persulfate
ARP 2/3	actin related protein 2/3
ATP	Adenosine triphosphate
BAC	bacterial artificial chromosome
β-cat	β-catenin
BCA	bicinchoninic acid
bp	basepair
BSA	bovine serum albumin
Cad	cadherin
cDNA	complementary deoxyribonucleic acid
CiP	calf intestine alkaline phosphatase
CMV	Cytomegalovirus
CO	cardiac output
Col1a1	collagen type I alpha 1 chain
Col1a2	collagen type I alpha 2 chain
Col3a1	collagen type III alpha 1 chain
Con-TS	vinculin no-force control
CP	cytoplasm
Ct	cycle threshold
Cx43	connexin-43
DAPI	4',6-diamidino-2-phenylindole
DCM	dilated cardiomyopathy
ddH_2O	distilled and purified water
dH_2O	distilled water
Dmd	dystrophin
DMSO	dimethyl sulfoxide
DNA	deoxyribonucleic acid
dNTP	deoxyribonucleoside triphosphate
DTT	Dithiothreitol
E	embryonic day
E. coli	Escherichia coli
ECM	extracellular matrix
EDTA	ethlyenediaminetetraacetic acid
EF	ejection fraction
EGTA	ethylene glycol-bis(β-aminoethyl ether)-N,N,N',N'-tetraacetic acid
ES	embryonic stem
F40	flagelliform
F7	stable seven aa linker
FA	focal adhesion
F-actin	filamentous actin
FAK	focal adhesion kinase
FBS	fetal bovine serum
FCS	fluorescence correlation spectroscopy
Fig	figure
Fiji	Fiji is just ImageJ
FL	ferredoxin-like fold
FLAMES	fluorescence lifetime analysis and merge software
FLIM	fluorescence lifetime imaging microscopy
Flp	flippase recognition target
FN	fibronectin
FRAP	fluorescence recovery after photobleaching
FRET	Förster resonance energy transfer
FRT	flippase recognition target
FS	fractional shortening
GA	gastrocnemius
GFP	green fluorescent protein
HBS	HEPES buffered saline
HCM	hypertrophic cardiomyopathy
HEK	human embryonic kidney
HEPES	4-(2-hydroxyethyl)-1-piperazineethanesulfonic acid
HF	high fidelity
HP35	villin head piece
HP35st	stable villin head piece
HR	Comparison of heart rate
HRP	horesradish peroxidase
IC	mechanosensitive ion channels
ICD	intercalated disk
Ig	immunoglobulin
Itg α /β	Iintegrin α /β
Itg β1	β1 integrin
Itgβ1D	integrin β1 D
kDa	kilo Dalton

KO	knockout
kPa	kilo Pascal
KS	Kolmogorov-Smirnov
LB	lysogeny broth
LINC	linker of nuceoskeleton and cytoskeleton
LSSmOrange	Large Stoke Shift monomeric Orange
M-B	metavinculin BFP
mCherry	monomeric Cherry
mKate2	monomeric Kate2
mRNA	messenger ribonucleic acid
MTFM	molecular tension-based fluorescence microscopy
mTFP1	monomeric teal fluorescent protein 1
M-TS	metavinculin tension sensor
M-V	metavinculin-Venus
MW	molecular weight
Myh6	myosin heavy chain 6
Myh7	myosin heavy chain 7
n.s.	not significant
NC	nuclear complex
N-cad	N-cadherin, neural cadherin
Nppa	Natriuretic peptide A precursor
Nppb	Natriuretic peptide B precursor
OD	optical density
P	pellet fraction
p120-cat	p120-catenin
PAA	polyacrylamide
PAGE	polyacrylamide gel electrophoresis
Palld	paladin
Pax	paxillin
PBS	phosphate buffered saline
PCR	polymerase chain reaction
PEG	polyethylen glycol
PFA	paraformaldehyde
pLL	poly-L-Lysine
PVDF	polyvinylidenfluorid
qRT-PCR	Quantitative real time polymerase chain reaction
RNA	ribonucleic acid
ROCK	Rho-associated protein kinase
ROI	region of interest
RT	room temperature
S	soluble fraction
s.c.	subcutaneous
SDS	sodium dodecyl sulphate
SV	stroke volume
T	total fraction
TAC	transverse aortic constriction
TAE	Tris-acetate-EDTA
TagBFP	tagged blue fluorescent protein
TAZ	transcriptional coactivator with PDZ-binding motif
TBS	Tris-buffered saline
TBS-T	Tris-buffered saline with Tween-20
TCSPC	time-correlated single photon counting
TEMED	N,N,N',N'-tetramethylethylenediamine
TL	tibia length
Tln1	talin-1
tln1$^{-/-}$tln2$^{-/-}$	talin-deficient mouse kidney fibroblasts
Tln2	talin-2
Tln-Con	talin no-force control
Tln-TS	talin tension sensor
Tln-Y	talin donor-only lifetime control
TS module	tension sensor module
TSS	Transformation and storage solution
Tub	tubulin
UV	ultraviolet
VASP	vasodilator-stimulated phosphoprotein
V-B	vinculin BFP
vinc$^{(-/-)}$	Vinculin-deficient mouse embryonic fibroblasts
vinc$^{(fl/fl)}$	parental cell line
V-TS	vinculin tension sensor
V-V	vinculin-Venus
VW	ventricular weight
V-Y	vinculin donor-only lifetime control
WB	Western blot
YAP	Yes-associated protein
Ypet	yellow fluorescent protein engineered for efficient energy transfer
Zyx	zyxin

TABLE OF CONTENTS

1 INTRODUCTION

1.1 MECHANOBIOLOGY

Cells and tissues are constantly exposed to mechanical stimuli. For example, myocytes are subdued to contraction and stretching in the working muscle (Magid and Law 1985); endothelial cells lining the blood vessels are exposed to fluid shear stress generated by blood flow, as well as to stretch induced by blood pressure (Hahn and Schwartz 2009); and chondrocytes are subjected to compressive forces in the articular cartilage (Freeman et al. 1994). Different organs in the body of mammals have characteristic stiffnesses ranging from the soft brain tissue (0.2–1.0 kPa) to the stiffer muscle tissue (8–12 kPa) to the rigid bone (25–40 kPa) (Irianto et al. 2016). Seeding mesenchymal cells onto substrates with according stiffness gives rise to neuronal, myocyte- and osteoblast-like cells (Engler et al. 2006). Similarly, culturing muscle stem cells on 12 kPa soft substrates before implantation in injured tibia muscle leads to successful differentiation into mature myocytes, whereas pre-culture on rigid plastic dishes prevents regeneration of the muscle tissue (Gilbert et al. 2010). Therefore, major efforts are made in tissue engineering to develop scaffolds with tunable mechanical properties to control cell behavior (Xia et al. 2017).

The process of converting mechanical cues into biochemically relevant signals is termed mechano-transduction and it is critical for many biological processes such as embryogenesis, development and tissue homeostasis. For example, in embryogenesis mechanical fluid flow is induced and sensed by specialized cilia in the ventral node, which is important for the establishment of left–right asymmetry in the embryo (Pennekamp et al. 2015). Moreover, extracellular matrix (ECM) stiffness and cell adhesion influence cell cycle progression and tissue architecture, both of which are compromised in cancer (Levental et al. 2009). Furthermore, gravity and locomotion stimulate local bone remodeling and an imbalance in this process was shown to result in osteoporosis (Hemmatian et al. 2017). Finally, blood flow is essential for correct heart development and disturbances in flow lead to various cardiovascular diseases such as atherosclerosis (Orr et al. 2006).

1.1.1 The cell – a mechanosensitive entity

The ability of cells to sense and translate mechanical cues is based on multiple subcellular structures, which together turn effectively the whole cell into a mechanosensitive object. The three major cytoskeletal networks – actin filaments, intermediate filaments and microtubules – respond to mechanical cues by altered polymerization kinetics, branching, growth direction or binding affinity to interactors (Harris et al. 2018; Brangwynne et al. 2007). These networks are connected to adhesion structures, such as focal adhesions (FAs), adherens junctions (AJs) and desmosomes, which not only transduce mechanical signals, but are also reinforced upon tension and regulate enzymatic and transcriptional activity (Geiger et al. 2009; Rubsam et al. 2017). Similarly, the plasma membrane transmits changes in tension, shear or bending leading to remodeling of the underlying cortical actin network (Gauthier et al. 2012; Mueller et al. 2017) and opening of embedded stretch-activated ion channels (Martinac 2011). Even the nucleus receives mechanical cues transduced by the LINC complex (linker of nucleoskeleton and cytoskeleton), which connects the inner nuclear lamin cytoskeleton to the cytoplasmic one, leading to modified gene transcription activity and chromatin organization (Kirby and Lammerding 2018).

Mammalian cells employ several mechanisms to orchestrate the various signals transmitted by these distinct mechanosensitive structures (Figure 1). Physical interconnection via the cytoskeleton allows an almost instantaneous transmission of mechanical cues between spatially separated mechanosensitive structures such as the extracellular space and the nucleus, leading to alteration of gene expression (Lombardi et al. 2011). Adaptor proteins shared by different mechanosensitive structures such as vinculin in FAs and AJs (Bays et al. 2014), as well as converging signal transduction cascades like the ERK signaling pathway modulated by mechanosensitive ion channel Piezo and FA receptor integrin (Gudipaty et al. 2017; Schwartz and Assoian 2001), further contribute to the integration of mechanical cues. Last but not least, feedback through transcriptional regulation, such as the re-localization of the transcription factors YAP (Yes-associated protein) and TAZ (transcriptional co-activator of PDZ-binding motif) from the cytosol into the nucleus upon extracellular mechanical cues, lead to long-term changes in protein expression (Dupont et al. 2011). Together these mechanisms allow the integration of mechanical cues at different time and length scales to generated a highly specific and spatially controlled mechanoresponse (Kanoldt et al. 2019).

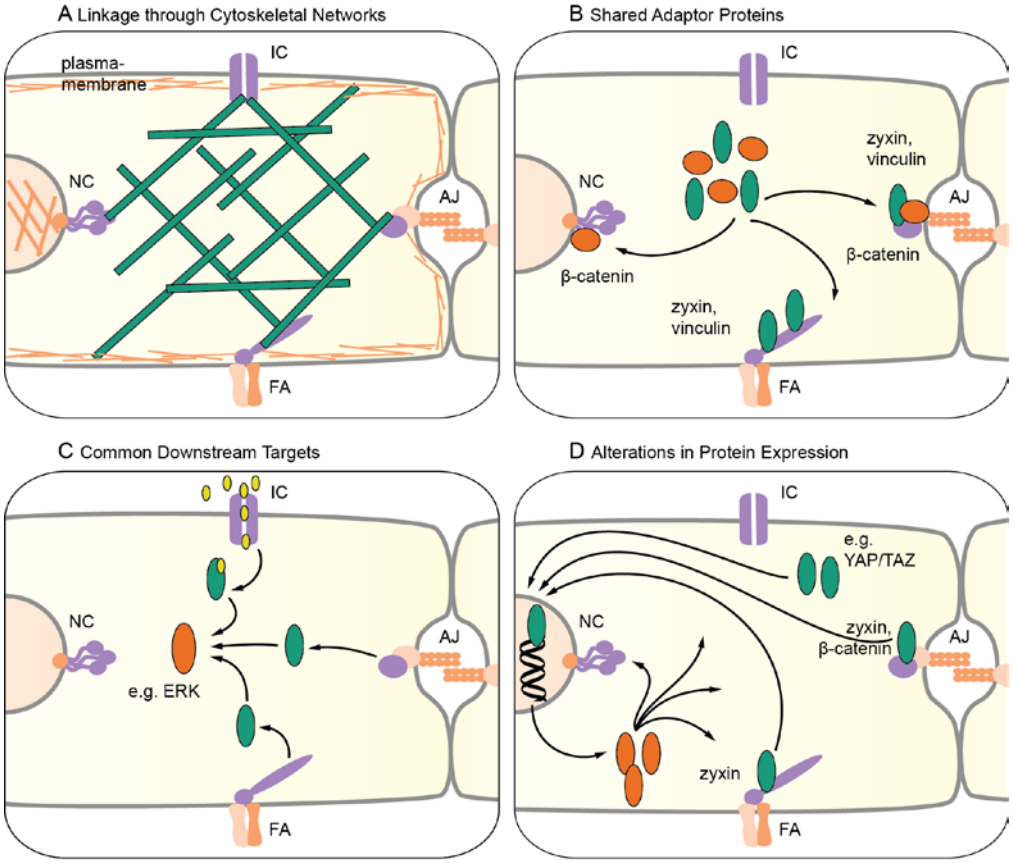

FIGURE 1: MECHANICAL CROSSTALK IN MAMMALIAN CELLS. (a) Mechanical linkage of distinct mechanosensitive structures through the internal cytoskeleton, cortical actin and the plasma membrane allows crosstalk through physical linkage. **(b)** Sharing common adaptor proteins as well as **(c)** interfering signaling cascades allow different mechanosensitive structures to interact. **(d)** Transcriptional regulators translocated upon mechanical stimuli into the nucleus may initiate altered protein expression feeding back on central elements of mechanosensitive complexes. Mechanosensitive structures: nuclear complex (NC), mechanosensitive ion channel (IC), adhesion junction (AJ) and focal adhesion (FA). Figure reproduced from Kanoldt et al. 2019.

1.1.2 Mechanotransduction in focal adhesions

The macromolecular complexes FAs (Figure 2a and c) connect the ECM to the intracellular actin cytoskeleton not only providing anchorage, but also allowing the cell to sense the chemical composition and mechanical properties of the ECM (Sun et al. 2016). The FA is arranged in three spatially and functionally distinct compartments: the integrin signaling layer, the force-transducing layer and the actin-regulatory layer (Kanchanawong et al. 2010). The actin regulatory layer is defined by proteins like zyxin and vasodilator-stimulated phosphoprotein (VASP), as well as actin filament crosslinker α-actinin, which are recruited to the FA upon mechanical stress to modify actin cytoskeletal dynamics (Hoffman et al. 2012). The integrin signaling layer is defined by the cell surface receptors integrins, which bind to a wide range of ECM proteins such as fibronectin (FN), vitronectin, collagens and laminins. The 18 α- and 8 β-integrin subunits expressed in mammalian cells form 24 functionally distinct heterodimeric transmembrane receptors providing specificity in FA assembly and signal propagation. Particularly the short integrin tail domain serves as an intracellular signaling hub recruiting more than 50 proteins and is bound by adaptor proteins like focal adhesion kinase (FAK) and paxillin as well as the integrin-activators kindlin and talin (Hynes 2002; Ringer et al. 2017a).

The ubiquitously expressed protein talin provides a direct link between the integrins and the actin cytoskeleton and acts as a scaffold for force-dependent recruitment of vinculin (Roberts and Critchley 2009). While the globular N-terminal head of talin binds to integrin, its large flexible C-terminal rod interacts with actin and contains up to 11 cryptic vinculin binding sites. Mechanical tension applied across the integrin–talin–actin linkage induces conformational changes in talin, thereby facilitating vinculin binding (Gingras et al. 2005; del Rio et al. 2009; Riveline et al. 2001). Recent *in vitro* studies revealed, that vinculin binding locks talin in an active conformation consequently stabilizing FAs (Yao et al. 2014a). Also, the reinforcing vinculin linkages were found to be directionally asymmetric and stabilized by force in a catch-bond dependent manner (Huang et al. 2017; Kluger et al. 2020). Therefore, both talin and vinculin act as mechanical regulators and characterize the force-transduction layer.

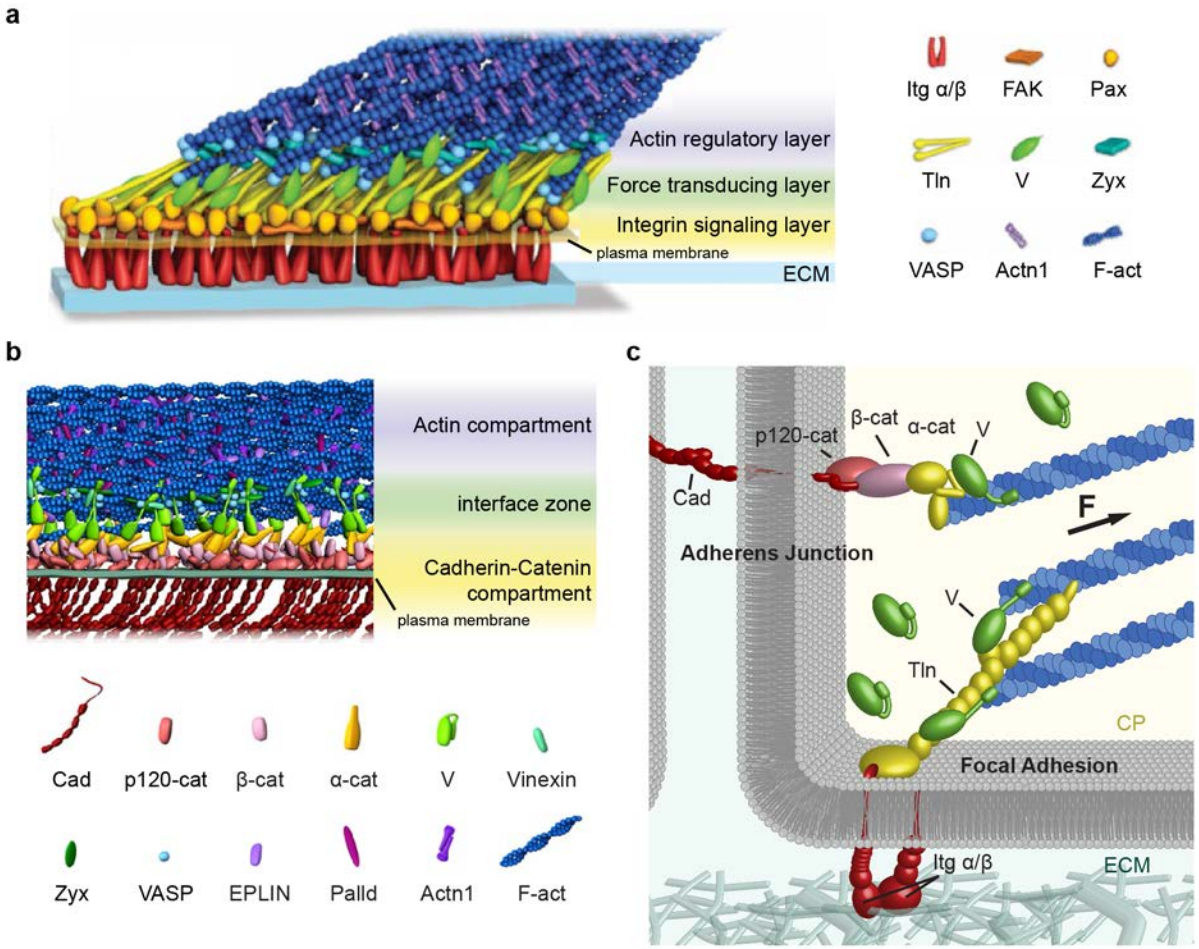

FIGURE 2: FORCE TRANSDUCTION IN CELL JUNCTIONS. Both, AJ and FA, are shaped by a distinct nanoscale architecture: **(a)** The integrin signaling layer in FAs is formed by the integrin cell surface receptors (Itg α /β) and signaling proteins like paxillin (Pax) and FAK. The direct connection of integrin to the actin cytoskeleton is mediated by talin (Tln) and reinforced by vinculin (V), which together define the force-transducing layer. Proteins such as zyxin (Zyx), VASP and α-actinin (Actn1) modulate the actin cytoskeleton in the actin-regulatory layer. **(b)** In the cadherin–catenin compartment of AJs, the cytoplasmic tail of the cell surface receptors cadherins (Cad) is bound by the catenin protein family comprising p120-catenin (p120-cat), β-catenin (β-cat) and α-catenin (α-cat) mediating the connection to the actin cytoskeleton. Vinculin (V) reinforces this connection in the interface zone and modulates the position of the actin regulatory proteins zyxin (Zyx), VASP and Vinexin. The actin cytoskeletal compartment contains further actin binding proteins such EPLIN, paladin (Palld) and α-actinin (Actn1). **(c)** AJs connecting the actin cytoskeleton of two neighboring cells and FAs anchoring the cell to the extra cellular matrix (ECM), share a conceptually similar mechanism of force transduction: a force-induced conformational change in α-cat or Tln, respectively, allows the reinforcement of the connection to the actin cytoskeleton by vinculin binding. Cytoplasm (CP), actin cytoskeleton depicted in blue. Note: the illustrations do not depict protein stoichiometry or lateral organization. The modified figures are reproduced from Kanchanawong et al. 2010 (a) and Bertocchi et al. 2017 (b).

1.1.3 Mechanotransduction in adherens junctions

Intercellular cohesion is mediated by AJs (Figure 2b and c), which connect the intracellular actin cytoskeleton of neighboring cells by cadherin–catenin linkages. This connection serves not only as physical link but also as signaling hub and mediates the mechanical coordination between cells, which is central to cell migration, morphogenetic processes and embryogenesis (Halbleib and Nelson 2006; Wozniak and Chen 2009). Similarly to FAs, also AJs are shaped by a multi-compartment nanoscale architecture comprising a membrane-proximal cadherin–catenin compartment, an interface zone and the actin regulatory compartment (Bertocchi et al. 2017).

The cadherin–catenin compartment is characterized by the AJ core complex consisting of the cell surface receptors cadherins and the catenin protein family (Hartsock and Nelson 2008). The extracellular domains of cadherins form Ca^{2+}-dependent homophilic interactions *in trans* to connect apposing cell surfaces. Additional interactions *in cis* lead to receptor clustering and consequently reinforcement of the intercellular connection (Harrison et al. 2011). The cytoplasmic tail of cadherin recruits a multitude of adaptor proteins and serves as a scaffold for catenin protein assembly: While association with p120-catenin regulates cadherin turnover at the plasma membrane, β-catenin mediates the link between cadherins and α-catenin.

The ternary cadherin–β-catenin–α-catenin complex is essential for AJ formation and mediates the connection to the actin cytoskeleton – a catch bond interaction that requires force to be observed *in vitro* (Buckley et al. 2014; Rangarajan and Izard 2012). While also other connections such as α-catenin–EPLIN–actin have been implicated in force transduction at AJs (Abe and Takeichi 2008), the direct connection of α-catenin to actin reinforced by vinculin defines the interface zone of AJs: Similarly to talin in FA, α-catenin contains one autoinhibited binding site for vinculin in its central adhesion modulation domain. Exposition of the buried α-helix upon force-induced unfolding triggers 1:1 binding of vinculin to the unfurled vinculin binding domain of α-catenin (Yonemura et al. 2010; Rangarajan and Izard 2012). This interaction prevents refolding of α-catenin even after force release, thereby stabilizing α-catenin in its open conformation (Yao et al. 2014b). Vinculin is essential for the fine tuning of the mechanoresponse in AJs and modulates the position of actin polymerization proteins like zyxin and VASP (Thomas et al. 2013; Bertocchi et al. 2017). Therefore, FAs und AJs not only share the common adaptor protein vinculin that enables crosstalk between the two mechanosensitive structures (Bays et al. 2014), but also the conceptual analogy of a force-sensing mechanism in force sensing: force-induced conformational changes allow reinforcement of cell surface receptor–to–actin cytoskeleton connections by vinculin, even though at different stoichiometry potentially reflecting the diverse mechanical context of cell–matrix and cell–cell adhesions (Hoffman et al. 2011).

1.2 VINCULIN AND ITS SPLICE ISOFORM METAVINCULIN

Vinculin is a ubiquitously expressed protein involved in several mechanotransduction processes. Its recruitment to AJs and FAs is regulated by internal actomyosin-dependent contraction (Huveneers et al. 2012; Le Duc et al. 2010), as well as by externally applied stress probed in form of stretching of cell doublets (Thomas et al. 2013), bead-twisting (Barry et al. 2014) or tweaking of extracellular matrix stiffness (Pasapera et al. 2010). Even though vinculin is not required for AJ and FA formation, it is essential for the establishment of cell polarity and, consequently, directional cell migration (Carisey et al. 2013; Bays and DeMali 2017), efficient epithelial barrier formation (Twiss et al. 2012) and cell-stiffening response (Le Duc et al. 2010). The splice variant metavinculin is co-expressed with vinculin in mammalian muscle tissue and encodes an additional 68 amino acid (aa) insert in its tail domain located between exon 18 and 19 (Koteliansky et al. 1992; Moiseyeva et al. 1993). Even though mutation and loss of metavinculin has been associated with cardiomyopathies (see also 1.3.3), comparably few studies were focused on this splice isoform.

1.2.1 Structure and activation of (meta)vinculin

The structure of vinculin (116 kDa) is largely similar to metavinculin (124 kDa) and comprises a globular head domain (95 kDa) connected by a flexible proline-rich linker (61 aa) to the tail domain (30 kDa) (Bays and DeMali 2017; Rangarajan et al. 2010; Ziegler et al. 2006). The vinculin head binds many proteins including talin (Johnson and Craig 1994), β-catenin (Yamada et al. 2005), α-catenin (Weiss et al. 1998) and α-actinin (Kroemker et al. 1994), while the unstructured linker region binds vasodilator-stimulated phosphoprotein (VASP; Brindle et al. 1996), ponsin (Mandai et al. 1999), vinexin (Kioka et al. 1999), and actin related protein 2/3 (Arp2/3; DeMali et al. 2002). The vinculin tail domain consists of an N-terminal strap (879–895 aa), a five-helix bundle (896–1045aa) and a C-terminal hairpin (1047–1066 aa; Bakolitsa et al. 1999) and binds to phosphatidylinositol 4,5-bisphosphate (PIP_2), paxillin (Wood et al. 1994), raver1 (Hüttelmaier et al. 2001) and actin (Hüttelmaier et al. 1997). Compared to its splice isoform, metavinculin shows a stronger affinity for the RNA-binding protein raver1, which is translocated to costameres upon muscle differentiation bearing vinculin mRNA and can bind metavinculin in its inactive state (Lee et al. 2012; Lee et al. 2009). Crystal structure analysis of metavinculin revealed that the 68 aa insert, located between aa 914 and aa 915, replaces the partially homologous N-terminal strap and H1 helix of the vinculin tail domain while contemporarily pushing out the original sequence to become part of the unstructured linker. The resulting new helix H1' harbors the most severe cardiomyopathy-associated missense mutation, R975W, whereas the L954del mutation and the mildest mutation, A934V, are located in the replaced extended coil and the preceding unstructured loop, respectively (Rangarajan et al. 2010; see 1.3.3). This newly formed

metavinculin tail domain and the elongated linker are the basis for the unique functions of metavinculin.

Both splice isoforms exist in an open active and a closed autoinhibited state, in which the head and tail domain are binding tightly to each other by two extensive hydrophobic interactions (Cohen et al. 2005). Most probably because of the elongated linker, the affinity of the head to tail interaction is considerably weaker in metavinculin, which is reflected in a higher affinity for talin accompanied by decreased turnover rates in the FA (Witt et al. 2004; Thoss et al. 2013; Kluger 2016). The cardiomyopathy-associated R975W mutation seems to reduce the affinity of the head to tail interaction even further (Rangarajan et al. 2010; Thoss et al. 2013). Several studies have shown the importance of the autoinhibitory regulation of vinculin for FA dynamics. The A50I point mutation in the head domain of vinculin strengthens autoinhibition and reduces the binding affinity of vinculin to talin and α-catenin (Bakolitsa et al. 2004; Diez et al. 2011). Contrarily, the charge–to–alanine mutations N773A and E775A (HTI) in the head domain of vinculin lead to an increase in vinculin activation, similarly to the corresponding point mutations D974A, K975A, R976A and R978A in the tail domain (T12; Cohen et al. 2005; Cohen et al. 2006).

While vinculin resides in its large cytoplasmic pool in a closed conformation (Lee and Otto 1997), studies applying a FRET-activation sensor revealed that the conformational state of vinculin is altered upon recruitment to cell–cell and cell–matrix junctions: adhesive puncta at the periphery of spreading cells comprise activated vinculin, while a switch to the inactive conformation precedes FA disassembly during membrane retraction, and fully established FAs show variable vinculin conformation (Chen et al. 2005). Chorev et al. (2018) recently proposed a third putatively force-bearing semi-open conformation mediated by a sequential 2-step unlocking mechanism and discovered different transition dynamics for vinculin and metavinculin resulting in potentially distinct force transduction. Although the mechanism of activation of the two splice isoforms is not yet fully understood and theories range from two ligand activation, to activation by phosphorylation, and, most recently, by mechanical tension (Bays and DeMali 2017; Ziegler et al. 2006), it might play a role in splice isoform-specific function.

1.2.2 The role of meta(vinculin) in actin organization

Vinculin mediates the functional link of the FA to the actin cytoskeleton and modifies the actin filament structure by promoting actin polymerization, capping barbed ends, as well as recruiting actin modulatory proteins such as Arp2/3 and VASP (Wen et al. 2009; Le Clainche et al. 2010; Bays and DeMali 2017). The vinculin–actin interaction is important for the regulation of filamentous actin (F-actin) organization and dynamics in lamellipodia, as well as frequency and rate of FA maturation (Thievessen et al. 2013; Humphries et al. 2007). Two distinct actin monomer binding surfaces located on helix H2 and H3 of the vinculin tail have been identified and were implied in binding of two adjacent actin monomers of filamentous actin (Janssen et al. 2006). Mutational studies resulting in small reductions in actin binding supported this model (Jannie et al. 2015; Cohen et al. 2006; Shen et al. 2011); however, point mutations outside those regions in helix H4 perturbed vinculin binding to actin to a greater extent (Thievessen et al. 2013; Thompson et al. 2014): V(I997A) and V(V1001A) resulted in a 50% and 30% reduction in actin binding, respectively, while notably V(I997A) was accompanied by a reduction in PIP_2 binding as well. A recent cryo-EM study by Kim et al. (2016) further supported the alternative actin-binding interface located on helix H4 and H5.

Binding of vinculin to F-actin induces a conformational change in its tail domain that enables the protein to dimerize and bundle actin filaments (Janssen et al. 2006; Johnson and Craig 2000; Hüttelmaier et al. 1997). Monomeric (meta)vinculin has been found to form homo- and hetero-oligomers *in vitro* as well, however, dimer-formation upon actin-binding appears structurally different and is favored over actin-independent dimerization (Shen et al. 2011; Johnson and Craig 2000). Likewise, distinct oligomerization of (meta)vinculin is induced by PIP_2, which is upregulated at the plasma membrane at cell adhesion sites and recruits and activates a variety of actin regulatory proteins (Bakolitsa et al. 1999; Ling et al. 2006). Whereas metavinculin shows a weaker binding affinity to PIP_2 (Witt et al. 2004), a recent crystallographic study revealed a PIP_2-induced asymmetric or symmetric homodimer for vinculin or metavinculin tail respectively, leading to binding of the membrane by the two splice isoforms in opposite orientation thus influencing actin organization (Chinthalapudi et al. 2014; Chinthalapudi et al. 2016).

The interrelated mechanism of actin binding and actin bundling is still not deciphered, especially because a structural model of the actin-induced vinculin dimer is missing, however, the N-terminus as well as the C-terminal hairpin of the vinculin tail were shown to be involved. Deletion of the last 5 aa was shown to ablate the capacity of vinculin to bundle actin, whereas actin-binding remained intact. Moreover, expression of the deletion mutant in cells led to spreading defects and impaired cell stiffening response upon application of force using magnetic tweezers (Shen et al. 2011). The N-terminal strap of vinculin was shown to unfurl and the entire helix H1 to be displaced from the its tail upon actin binding, which seemed to be required for bundling activity (Bakolitsa et al. 2004; Kim et al. 2016).

Intriguingly, an analogous displacement of helix H1' was observed for metavinculin leading to an indistinguishable interaction with actin. Still, the bundling capacity of metavinculin was shown to differ greatly from vinculin in *in vitro* experiments. In contrast to vinculin tail, which bundles actin into thick filaments, metavinculin tail induces fine mesh-like networks of F-actin (Rüdiger et al. 1998; Rangarajan et al. 2010) presumably causing altered cell stiffening response (Lee et al. 2019). This difference has been attributed to the displaced helix H1 sterically preventing dimerization and associated to a potential capacity of metavinculin to sever or tune the flexibility of actin-filaments thereby modulating the actin network architecture (Janssen et al. 2012; Oztug Durer et al. 2015; Sarker et al. 2019).

Interestingly, point mutations or deletions associated with cardiomyopathies (see 1.3.3) formed actin bundles resembling the vinculin tail-induced actin organization with a propensity correlating to disease severity (Olson et al. 2002). The presence of metavinculin at sub-stoichiometric ratios was further observed to inhibit vinculin tail-mediated actin bundling, whereas the cardiomyopathy mutants failed to do so (Kim et al. 2016; Sarker et al. 2019). Since the two splice isoforms are co-expressed in muscle tissue, this might reflect a role of metavinculin to tune actin organization in the muscle, which is perturbed upon mutation.

1.3 METAVINCULIN AND MECHANOBIOLOGY OF THE HEART

1.3.1 Mechanobiology of the heart

The heart pumps blood through the body thereby supplying oxygen, various nutrients and biochemical signaling compounds to the diverse tissues and organs of our body. During each heart beat mechanical work is performed: The cardiomyocytes of the heart chamber are stretched as the blood flows in and subsequently contracted during ejection against arterial resistance (Sequeira et al. 2014). The cytoskeletal architecture and its mechanosensitive elements react to extra- and intracellular stimuli and actively regulate cardiac morphogenesis.

Already during embryogenesis, mechanical cues together with morphogenetic signals are required for correct development of the heart. Processes such as vascularization, valvulogenesis, heart looping and ventricle chamber size are sensitive to pressure and shear stress generated by blood flow (Majkut et al. 2014). The cardiac tissue undergoes mechanical stiffening starting at <0.2 kPa (Young modulus) in the embryonic cardiac tube to a value >20 kPa at birth (Majkut et al. 2013). Indeed, the first coordinated heart beat occurs in the embryonic cardiac tube (E9 in the mouse) and is potentially purely based on the contractions of cardiac progenitor cells coordinated by their mechanosensitive ion channels upon increased stiffness of the ECM during development (Gaetani et al. 2020). During mechanical maturation, differentiation of the myocardial cells into contractile cardiomyocytes is reflected by a rapid increase in rate of contraction and is constantly matched by growing stiffness of the heart tissue to provide the contractile optimum. *In vitro* studies on isolated tissue and cardiomyocytes of chicken confirmed that optimal stiffness of the heart tissue is required for heart beat and sarcomere registration (Majkut et al. 2013) – valuable knowledge for *in vitro* cardiac tissue engineering and development of regenerative medicine (Gaetani et al. 2020).

The ECM is produced by cardiac fibroblasts and is the main driver of mechanical stiffening. Fibronectin is mostly expressed during embryonic development, whereas elastin is upregulated in the adult heart. Collagen contributes to passive mechanics and helps to limit the expansion of the heart during diastole protecting myocytes from overstretch, while during systole it sustains myocyte alignment and force transmission (Fomovsky et al. 2010). Collagen I is highly abundant in the developing as well as the adult heart (90%), but cross-linking and density is increased in the latter and the ratio of collagen I to III is reduced (Gaetani et al. 2020). Pathological changes in protein composition and cross-linking of the ECM are characterized by aberrant myocardial stiffening and interstitial fibrosis, defined as diffuse collagen fiber accumulation within the cardiac interstitium, as well as extensive collagen-rich scar formation upon e.g. cardiac infarct (González et al. 2019). Maladaptive stiffening of the tissue produces cellular mechanical damage, inflammation, and ultimately myocardial fibrosis, which are

paralleled by changes in actomyosin contractility as well as cytoskeletal protein adaptation (Gaetani et al. 2020).

The rod-shaped cardiomyocytes are connected to each other at their bipolar ends by intercalated discs (ICD). The ICDs comprise three types of interdependently working cell contacts, which together enable the highly orchestrated integration of sarcomeric shortening into cellular contraction: the AJs (see also 1.1.3) form the anchor of the actin filaments of myofibrils and therefore transmit the contractile forces between cells; the desmosomes connect the intermediate filaments of neighboring cells and protect the cardiomyocytes from contractile stress as well as abrasive forces; and the gap junctions connect the cytoplasm of adjacent cells and mediate the transfer of metabolites and ions, thereby allowing the propagation of electrical stimuli for coordinated heart contraction (Zhao et al. 2019). Furthermore, the Z-discs of the cardiomyocytes are connected to the ECM at their lateral sides by costameres, which are composed of the dystrophin–glycoprotein and the integrin–vinculin–talin complexes (see also 1.1.2) and ensure homogenous sarcomere length in contracting and resting cells (Belkin 1996). Exclusive localization of ICD and costamere components is observed only after birth, when the need for an dramatic increase in mechanical performance of the heart is met by a conversion from the fetal to the adult structure of the sarcomeres, a reduction in proliferation accompanied by an increase in cardiomyocyte volume and a polygonal to rod-like shape change (Ehler 2016; Hirschy et al. 2006). In humans, segregation of AJs and desmosomes to the short ends of cardiomyocytes was observed one year after birth, whereas full gap junction restriction was detected only much later (Vreeker et al. 2014).

Thus, the heart constantly adapts to changing mechanical needs during development and challenges presented during lifetime of an individual. In the healthy heart, pressure overload causes thickening of ventricular chambers due to increased cross-sectional area of the ventricular myocytes in consequence to parallel addition of myofibrils (=concentric hypertrophy). Contrarily, volume overload leads to addition of sarcomeres in series resulting in lengthening of ventricular myocytes concurrent with thinning of the ventricular wall, dilation of the chamber and elevated wall stress (=eccentric hypertrophy). Failure in response to such extracellular stimuli due to e.g. genetic mutations in proteins of the sarcomeres and cell–cell adhesions – including AJs and costameres – result in hypertrophic (HCM) or dilated cardiomyopathies (DCM), which are both associated with lost segregation of ICD and costamere markers, reduced contractility, and eventual heart failure (McCain and Parker 2011; Ehler 2016). In order to correct misfunction in disease or take advantage for tissue engineering, we first have to understand force transduction at the cellular level.

1.3.2 Cell adhesions and their role in cardiomyopathy

The importance of cell–cell adhesion proteins for correct heart function has been recognized and several transgenic mouse models have been already generated to investigate the role of specific key proteins of these mechanosensitive structures. Hereinafter, a selection of cell–cell adhesion proteins involved in cardiac function and pathology is presented and the role of deletion and mutations in vinculin is discussed in detail in section 1.3.3.

In the ICD, the major desmosomal proteins, such as plakophilin, plakoglobin, desmoglein, desmocolin and desmoplakin, are common targets for mutations causing inherited heart disease. Desmoplakin expression in cardiomyocytes, for example, is crucial for heart integrity as cardiac-specific introduction of different point mutations into the head domain of desmoplakin was shown to be embryonic lethal due to major defects in heart development (Zhao et al. 2019; Yang et al. 2006). In comparison, AJ proteins have not been studied extensively for mutations related to cardiomyopathies. Neural (N)-cadherin, the sole cadherin expressed in the heart, is essential for cardiac development and its deletion in mice is embryonic lethal (E10) due to severe cardiac adhesion defects and malformation of the heart tube, amongst others. Its cardiac specific excision in the adult myocardium led to the dissolution of ICDs followed by arrythmia-induced death after two months (Radice et al. 1997; Kostetskii et al. 2005). On the other hand, overexpression of N-cadherin in transgenic mice caused altered ICD structure with redistribution of vinculin and also led to DCM.

Cardiac-specific ablation of α-E-catenin results in progressive DCM, ultrastructural defects in ICD and loss of vinculin from the ICD, as well as a predisposition to ventricular free wall rupture after myocardial infarction (Sheikh et al. 2006). Studying the role of β-catenin in the heart is more complicated, since it is not only part of the AJ structure but also acts as nuclear transcription factor in the Wnt signaling pathway. β-catenin plays an important role in embryonic development including the differentiation of cardiac progenitor cells. It was shown to act as regulator of physiological hypertrophic growth in adult cardiomyocytes and might be detrimental to pathological hypertrophy (Manring et al. 2018). Knockout of β-catenin is embryonic lethal (E7), whereas the lack of β-catenin in adult cardiomyocytes is most probably compensated by an upregulation of p120-catenin (Haegel et al. 1995). On the other hand, targeted ablation of β-catenin in cardiomyocytes led to a blunted hypertrophic response upon pathological stress, which was attributed to its altered transcriptional activity (Chen 2006). Furthermore, stabilization of β-catenin created by transgenic expression of a non-degradable form of β-catenin is detrimental and leads to DCM (Hirschy et al. 2010).

The deletion of costamere marker integrin β1 is embryonic lethal shortly after implantation (E5.5) and cardiomyocyte-specific reduction in the heart leads to cardiac fibrosis, depressed heart function and

intolerance to hemodynamic loading resulting in development of DCM (Shai et al. 2002; Stephens et al. 1995; Fässler and Meyer 1995). Mutations in the DGC protein dystrophin cause Duchenne's or Becker's muscular dystrophy and are also involved in the development of DCM, although the associated skeletal muscle phenotype is more severe (Elsherif et al. 2008). Interestingly, combined deletion of the costamere markers dystrophin and integrin β1 in cardiomyocytes causes increased mortality following pregnancy-induced volume overload in peri- and postpartum female mice accompanied by severe myocardial necrosis, fibrosis and calcification.

Vertebrates express two talin isoforms, which cannot completely compensate for each other (Gough and Goult 2018). Whereas talin-1 is ubiquitously expressed, talin-2 distribution is restricted and the isoform is found at high levels in e.g. muscle tissue, brain and kidney (Monkley et al. 2001). The embryonic heart expresses both isoforms, but talin-2 becomes the predominant isoform in adult cardiomyocytes and displays a higher binding affinity to the muscle-specific integrin isoform integrin β1D as well as actin (Anthis et al. 2010; Koteliansky et al. 1991; Senetar et al. 2007). Even though talin-1 is essential for development (Monkley et al. 2000), its role in adult myocardium seems to be limited, since cardiac-specific talin-1 knockout mice display normal basal cardiac structure and function. These mice show even a beneficial remodeling response upon pressure overload and a delay in onset of cardiac failure, although talin-1 is normally upregulated upon cardiac stress (Manso et al. 2013). Global talin-2 ablation on the other hand, leads to a mild skeletal myopathy related to defective myotendinous junction integrity, but no cardiac phenotype, even though muscle-specific integrin β1D isoform expression levels were decreased to 50% (Conti et al. 2009). However, additional cardiomyocyte specific deletion of talin-1 causes cardiac dysfunction and death 6 months after birth, accompanied by loss of costamere integrity (Manso et al. 2017). Taken together, the studies presented above emphasize the importance of specific functions of protein isoforms, a balanced protein composition of cell–cell adhesions as well as a limited response upon stress for the maintenance of cardiac integrity.

1.3.3 (Meta)vinculin in physiology and disease

In the muscle tissue of vertebrates, metavinculin is co-expressed with vinculin at different molar ratios. While metavinculin is highly expressed in smooth muscle tissue, such as aorta wall and myometrium (30–40%), and in the skeletal muscle (up to 15–25%), expression in the heart was observed at a comparably lower degree, ranging from only traces up to 18% of the total vinculin amount (Witt et al. 2004; Belkin et al. 1988b; Feramisco et al. 1982). Expression of metavinculin is upregulated together with talin-2 during muscle differentiation of human aortic smooth muscle cells, as well as human skeletal muscle myoblasts, and the mouse muscle cell line C2C12 in comparison to relatively low and stable vinculin and talin-1 levels (Koteliansky et al. 1991; Senetar et al. 2007). Furthermore, studies involving hindlimb suspension in mice and muscle loading in healthy young humans revealed a positive correlation of metavinculin expression and muscle load (Li et al. 2013; Chopard et al. 2002).

Metavinculin was found to co-localize with vinculin at cell attachment sites. In skeletal muscle, vinculin and metavinculin co-localize in myotendinous junctions and costameres, however, metavinculin was found to be restricted to fast twitch skeletal fiber types (Thoss et al. 2013; Pardo et al. 1983). Both splice isoforms are found in dense plaques, which are the cell–cell interaction sites of smooth muscle cells in, for example, the urinary bladder or the myometrium of the uterus (Pardo et al. 1983). In the heart, (meta)vinculin is found in the ICDs at the N-cadherin-based AJ as well as in the costameres at the integrin–talin–actin complexes, which are located directly above the Z–line. When primary muscle cells are taken into cell culture, the two isoforms are detected in FAs; however, metavinculin expression is progressively lost over time concordant with a loss of cell contractility (Belkin et al. 1988a; Koteliansky et al. 1991; Thompson et al. 2013).

Vinculin is an essential protein for normal embryonic development, as its global deletion in mice is embryonic lethal at E10 due to aberrant neuronal tube closure and failure of proper heart tube fusion amongst others (Xu et al. 1998). Furthermore, vinculin is an essential protein for development and muscle contraction in nematodes, which like drosophila do not express metavinculin (Barstead and Waterston 1991). Mass spectrometry analysis comparing adult and aged monkey and rat myocardial proteome revealed an age-associated upregulation of vinculin and its overexpression in drosophila was found to be beneficial increasing life span to 150% (Kaushik et al. 2015). In the adult heart, heterozygous deletion of vinculin and metavinculin together does not lead to altered heart function, but ultrastructural defects in ICDs and susceptibility to mechanical stress induced by pressure overload in the heart (Zemljic-Harpf et al. 2004). Cardiomyocyte-specific excision of both splice isoforms led to either sudden death in 49% of mice younger than 3 months of age, or dilated cardiomyopathy with

conduction defects in early adulthood preceded by abnormalities in the ICDs, which were characterized by reduced N-cadherin and integrin β1D expression, as well as mislocalized connexin-43 (Zemljic-Harpf et al. 2007). Together, these studies emphasize the importance of (meta)vinculin for the integrity of cardiac physiology.

Mutations specific to the 68 aa insert of metavinculin, as well as absence of this splice isoform, were associated with cardiomyopathies. Metavinculin deficiency attributed to a defect in alternative mRNA splicing was found in a 21-year-old patient with DCM showing irregular ICD structure (Maeda et al. 1997). The pathologically most severe mutation R975W was detected in a 52- and a 42-year-old patient with DCM as well as HCM. Immunohistochemical and ultrastructural analysis of the resected myocardia showed a reduction of (meta)vinculin in ICDs, whereas costamere staining was maintained in the specimen of the HCM patient. In addition, the same studies identified the A934V mutation, which, however, is also present in healthy control patients (Olson et al. 2002; Vasile et al. 2006). Furthermore, a 3-bp deletion (L954del) was identified in a 39-year-old patient with DCM creating a truncated metavinculin version (Olson et al. 2002). *In vitro* studies of all three mutants revealed that the mutations altered actin filament cross-linking organization correlating with the severity of the cardiac phenotype of the patients harboring the respective mutation (see also 1.2.3.). Therefore, metavinculin seems to play a distinct role in heart function, which needs to be investigated further *in vivo.*

1.4 MEASURING FORCES IN CELL BIOLOGY

The relevance of mechanical forces in biology has been increasingly recognized in the recent years. In order to gain a better understanding of the molecular processes involved in mechanotransduction, forces relevant to the biological system need to be measured and quantified. Consequently, several methods have been developed to analyze forces on the single molecule level (Freikamp et al. 2017). *In vitro* force spectroscopy techniques include optical tweezers, magnetic tweezers and atomic force spectroscopy, which allow the analysis of pN-forces (Figure 3a–c). In all three techniques, one end of the protein of interest is anchored to a surface, e.g. a glass coverslip, another protein or a cell surface. The other end is attached to an optically trapped bead, a magnetic bead or the AFM tip, respectively, through which force is applied. The displacement of the bead or tip is used as a measure of force (Neuman and Nagy 2008). These three techniques have been used to study the generation of force by motor proteins, stiffness as well as unwinding behavior of DNA, and adhesion forces between cells, amongst others (Lipfert et al. 2010; Kuo and Sheetz 1993; Benoit et al. 2000).

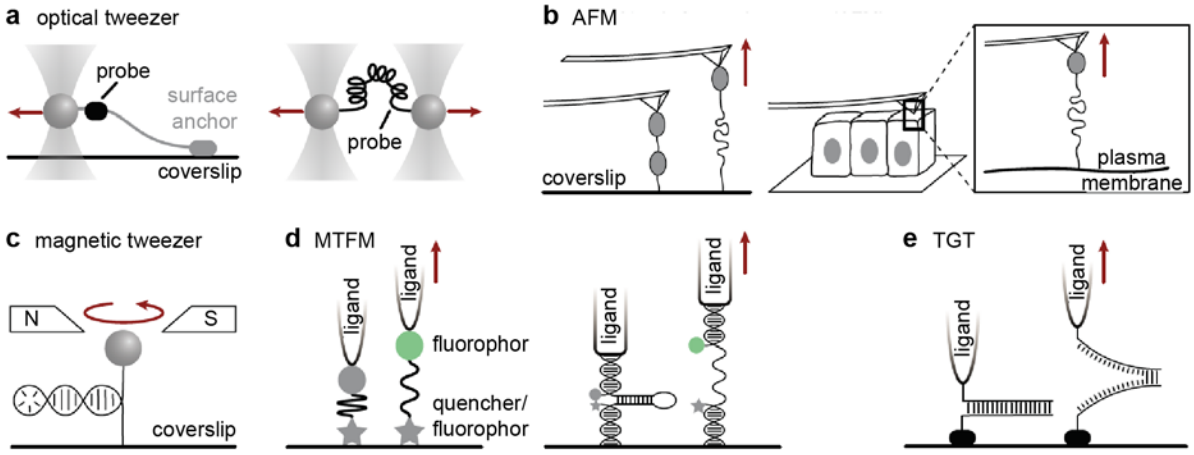

FIGURE 3: TECHNIQUES TO MEASURE FORCE ACROSS SINGLE MOLECULES *IN VITRO* OR AT THE CELL SURFACE. (a) Optical tweezers use optically trapped beads to exert and measure forces on single molecules to study protein unfolding or the interactions of proteins. **(b)** Atomic force microscopy (AFM) enables the study of protein unfolding and can be used to exert forces on individual immobilized proteins or cell surface receptors on cells. **(c)** Magnetic tweezers are used to quantify torque on DNA and proteins by using a magnetic field. **(d)** In molecular tension fluorescence microscopy (MTFM) exerted tension is visualized by external FRET-based tension sensors, which are comprised of a fluorophore FRET pair connected by a force-sensitive peptide or DNA-based linker element. **(e)** Tension gauge tether (TGT) probes are based on a similar principle, but contain a double-stranded DNA linker, which ruptures upon exceeding a tunable force threshold. Modified figure is reproduced from Freikamp et al. 2017.

Whereas the single molecule atomic force spectroscopy techniques are limited to *in vitro* applications, the introduction of Förster resonance energy transfer (FRET)-based tension sensors brought single-molecule force measurements closer to a physiological level (Jurchenko and Salaita 2015). External tension sensors are typically immobilized on a solid support and consist of a spectrally matched fluorophore or a fluorophore–quencher pair connected by a force sensitive linker (Figure 3d). Force-induced elongation of the linker element, consisting of a peptide or a DNA strand, results in either a fluorescence gain or a decrease in FRET, which can be detected microscopically (see also 1.3.1). Another class of external tension sensors, the tension gauge tether (TGT) (Figure 3e), comprises two complementary DNA strands as a linker element, which rupture when a tunable force threshold is exceeded (Sarkar et al. 2018). External tension sensors have been used to study cell–ECM and cell–cell interactions as well as the process of cell adhesion and migration. However, the direct measurement of tension across distinct proteins inside a living cell or even an organism, is only possible by the application of genetically encoded FRET-based tension sensors (Freikamp et al. 2017).

1.4.1 Genetically encoded FRET-based tension sensors

In contrast to the force measurement techniques described above, genetically encoded FRET-based tension sensors allow the analysis of forces experienced by distinct proteins in their physiological environment and are based on the genetic insertion of a tension sensor module (TS module) into a protein of interest. The TS module is comprised of a fluorophore FRET pair, which is connected by a force sensitive linker peptide. In the absence of tension, the two fluorophores are in close proximity and undergo efficient FRET. Application of a force exceeding the force threshold of the linker peptide, leads to an increase in fluorophore separation and thus to a FRET efficiency decrease, which is recorded by a microscopy method (Figure 4a).

The design of a TS module requires the choice of an efficient fluorophore FRET pair, which consists of a donor and an acceptor fluorophore with overlapping excitation and emission spectra. Previous tension sensor studies have used FRET pairs with yellow/red (Grashoff et al. 2010; Austen et al. 2015; Ringer et al. 2017b; Price et al. 2018; Lemke et al. 2019), blue/yellow (Borghi et al. 2012; Price et al. 2018) or green/red (Kumar et al. 2016; LaCroix et al. 2018) emission spectra. When more than one tension sensor is measured simultaneously in a multiplexing experiment, the orthogonal fluorophore pairs mTFP1/ShadowG and LSSmOrange/mKate2 have been used, which can be excited with same excitation wave length (Ringer et al. 2017b; Demeautis et al. 2017).

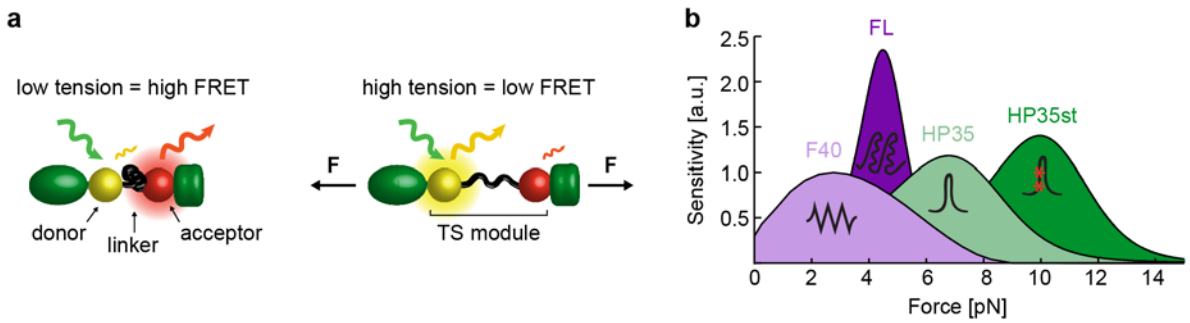

FIGURE 4: GENETICALLY ENCODED FRET-BASED TENSION SENSORS. (a) Schematic depiction of the principle of the FRET-based tension sensor. The TS module is comprised of a fluorophore FRET pair separated by a force sensitive linker peptide and is genetically integrated within a flexible region of the protein of interest (green). Mechanical force experienced by the tension sensor leads to extension of the mechanosensitive linker peptide and a consequent separation of the fluorophores resulting in a FRET efficiency decrease. **(b)** Single molecule force calibration was used to determine the force sensitivity of the mechanosensitive flagelliform (F40), ferredoxin-like (FL), villin headpiece (HP), and stabilized villin headpiece (HPst) linker peptides. Graph includes schematic depictions of the linker peptides. Modified figure reproduced from Ringer et al. 2017b

The mechanosensitive linker peptide is a key element in the TS module and needs to fulfill certain criteria to allow efficient force measurement (Freikamp et al. 2016). First, the linker peptide has to respond to specific forces typically located in the pN range, which are suitable to the analyzed protein of interest. Second, the contour length increase upon force-induced unfolding needs to be large enough to induce a measurable FRET efficiency drop. Third, linker peptide unfolding is required to be reversible upon force release, while the force response should be insensitive to the velocity of the applied mechanical force and thus be loading-rate insensitive. Finally, the linker peptide has to display similar unfolding and refolding transitions and therefore be free of hysteresis. To ensure that those requirements are met, the calibration of TS modules by single molecule force spectroscopy is recommended (Figure 4b). The first single-molecule calibrated tension sensor peptide is the 40 aa-long fagelliform (F40) peptide, which was derived from spider silk and gradually unfolds at forces of 1–6 pN (Grashoff et al. 2010). Contrarily, the 82 aa-long ferrodoxin-like fold (FL) peptide opens in a switch-like manner at forces of 3–5 pN accompanied by a larger contour length increase, thus leading to the highest sensitivity displayed by all single-molecule-calibrated genetically encoded TS modules so far (Ringer et al. 2017b). The 35 aa-long villin headpiece (HP35) peptide is sensitive to higher molecular forces and opens at 6–8 pN (Austen et al. 2015). The currently stiffest linker peptide of this kind, is the HP35 linker containing two additional point mutations (HP35st) causing the linker to open at forces of 9–11 pN (Austen et al. 2015). The combination of these four linker peptides is particularly valuable, as it enables the analysis of forces, and especially the force distribution, within the entire range of 1–11 pN.

The TS module, comprising one of the fluorophore FRET pairs and one of the linker peptides, is genetically inserted into a protein of interest and the resulting tension sensor is either overexpressed in cells by transfection or viral infection, or integrated at the corresponding genomic position by genome engineering methods such as CRISPR/Cas9. The integration site of the TS module needs to be chosen at an intramolecular position suitable to report the mechanical state of the protein, and such as not to interfere with protein or TS module functionality (Cost et al. 2015). Therefore, typical integration sites are located in unstructured, flexible and non-conserved protein domains. Specific functionality assays depend on the protein of interest, but commonly involve a combination of verification of subcellular localization by immunostainings or protein turnover rates by fluorescence recovery after photo bleaching (FRAP), and, ideally, the phenotype rescue in knockout cells or organisms upon expression of the tension sensor (Cost et al. 2019).

1.4.2 Evaluating FRET in tension sensor experiments

Förster resonance energy transfer (FRET) is a photophysical process, during which energy is transferred from an excited donor fluorophore to an acceptor fluorophore with overlapping emission and excitation spectra in a radiation-free and distance-dependent manner. The efficiency of the energy transfer E depends on the quantum yield of the donor fluorophore, the extent of spectral overlap and the orientation as well as the distance of the fluorophores towards each other. In biological systems rotational freedom of the fluorophores is assumed and the efficiency of the energy transfer E is defined as

$$E = \frac{R_0^6}{R_0^6 + r^6} \tag{1}$$

with R_0 being the Förster distance at which E=50% for a specific fluorophore pair and r being the distance between the donor and acceptor fluorophore (Lakowicz 2006). The FRET efficiency is inversely proportional to the fluorophore distance to 6th power and is thus a powerful tool to detect the small force-induced distance changes experienced by the genetically encoded tension sensors inside a biological system.

The FRET efficiency of tension sensors can be quantified by time-correlated single-photon counting fluorescence lifetime imaging microscopy (TCSPC-FLIM) (Austen et al. 2013). Therefore, the donor fluorophore is repeatedly excited with an ultra-short laser pulse and the arrival times of the emitted photons are recorded in a pixel-resolved manner. The resulting histogram of the arrival times reflects the fluorescence decay curve, which is fitted with an exponential decay function to determine the lifetime of the donor fluorophore. Since FRET offers a radiation-free alternative relaxation pathway, the average lifetime of the donor fluorophore is reduced in the presence of an acceptor fluorophore

(Wallrabe and Periasamy 2005). Consequently, the comparison of the donor fluorophore lifetime in the presence and absence of the acceptor fluorophore can be used to calculated the FRET efficiency (see 2.4.3). As the unique fluorescence lifetime decay is an inherent property of each fluorophore, it is independent of the excitation intensity or concentration of the fluorophore, even though, both parameters will influence the fitting quality. Furthermore, only the donor fluorescence is analyzed and therefore spectral bleed-through, cross excitation or photobleaching of the acceptor is avoided (Wallrabe and Periasamy 2005). However, molecular environmental factors such as pH, ion concentration and temperature do influence the lifetime of the fluorophore. Consequently, the donor fluorophore lifetime is assessed with a so-called donor-only lifetime control construct, which either comprises the donor fluorophore alone at the TS module integration site in the protein of interest, or consists of the tension sensor with a fluorescently inactivated acceptor fluorophore (Cost et al. 2019).

To quantify the extent of a FRET efficiency drop upon force, the starting FRET efficiency of the relaxed tension sensor needs to be determined. Therefore, a no-force control construct, unable to respond to molecular tension, is designed by placing the TS module at the C- or N-terminal end of the protein of interest. However, at this position the fluorophores are exposed to a different molecular environment, which might influence the fluorescence lifetime. Truncating the tension sensor after the acceptor fluorophore improves this issue, if truncation does not impair correct subcellular localization (Figure 4a). The least invasive method to generate a no-force control is to introduce point mutations or small deletions within the protein of interest leading to abolished or reduced force transmission.

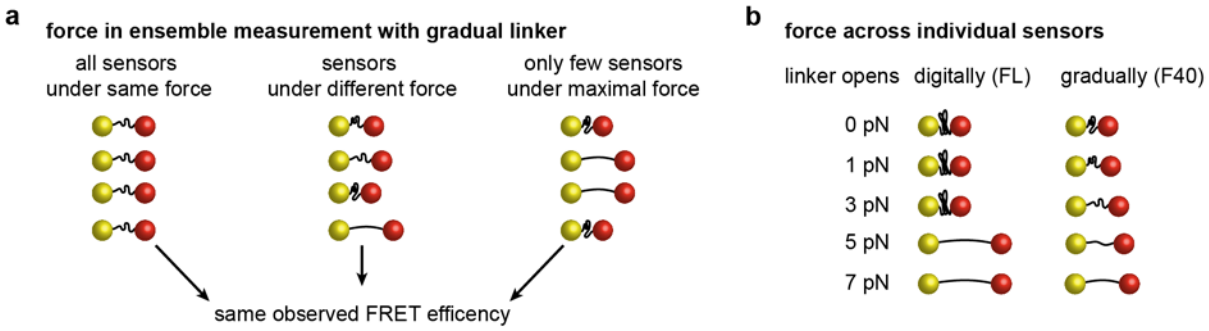

FIGURE 5: INTERPRETATION OF FRET MEASUREMENTS OF TENSION SENSORS. (a) In ensemble FRET measurements using a gradually unfolding linker, the observed average FRET efficiency can be can be generated either by all molecules stretched to the same extent, a mixture of different stretch degrees, or by molecules in either the stretched or the unstretched conformation. Using several linker peptides with different force sensitivities can help to differentiate between those scenarios. **(b)** Mechanosensitive linkers, such as the FL peptide, respond to forces in an almost digital manner, therefore existing either in a closed folded (high FRET efficiency) or an open stretched conformation (low FRET efficiency), whereas linkers such as the F40 peptide unfold gradually within a specific force range, therefore potentially displaying a range of different FRET efficiencies within its force sensitivity range. Modified figure reproduced from Cost et al. 2019.

FRET efficiency differences, observed upon comparison of the tension sensor and no-force control data, reflect the minimal force experienced by the protein of interest in relation to the force threshold of the employed linker peptide. Note, that the upper limit of experienced forces cannot be reported by only one individual linker and narrowing down the force range exerted on the protein of interest requires a combination of linker peptides with different force sensitivities. Due to signal intensity limitations of live-cell experiments, the tension sensor measurements are typically ensemble recordings of e.g. all tension sensors within the FAs of one cell. Therefore, the resulting FRET efficiency reports an average force value, which does not give insight into the force distribution within the tension sensor population (Cost 2019; Cost et al. 2019). The same average FRET efficiency value could thus be generated by all molecules under the same average force, the molecules under either high or no force, or a mixture with molecules under a range of different forces (Figure 5a). Depending on the nature of the force response of the employed linker peptide, one of the scenarios is more likely (Figure 5b). When the second case is assumed, the molecular engagement ratio, which is the relative amount of stretched molecules, can be calculated using a recently developed analysis method based on bi-exponential fitting (see 2.4.3; Ringer et al. 2017b; Lemke et al. 2019). In summary, carefully controlled and interpreted genetically encoded FRET-based tension sensor experiments are a powerful tool to investigate molecular tension on distinct proteins in their physiological environment.

1.4.3 Forces in cell adhesions

The genetically encoded tension sensors have been applied before to measure tension in essential mechanosensitive proteins of FAs and AJs. For instance, experiments with F40-based epithelial (E)- and vascular/endothelial (VE)-cadherin tension sensors revealed, that both protein family members are under tension in cell–cell junctions requiring actomyosin contractility as well as α-catenin (Borghi et al. 2012; Conway et al. 2013). Furthermore, E-cadherin tension sensor expression in flies unraveled a tension gradient across E-cadherin in directionally migrating ovarian cell clusters, emphasizing the importance of the cell surface receptor for direction sensing, although, this observation could not be reproduced (Cai et al. 2014; Eder et al. 2017). Moreover, measurement of tension on VE-cadherin in cells and zebrafish helped to shed light on the molecular mechanism of force-regulated angiogenesis (Lagendijk et al. 2017; Conway et al. 2013). While most cadherin tension sensor studies are focused on epithelial systems, a recent study using a F40-based neural (N)-cadherin tension sensor revealed cell-type specific tension on N-cadherin in vascular smooth muscle cells (Puranam et al. 2019). Downstream of cadherins, tension on the catenin protein family was studied with a F40-based αE-catenin tension sensor, which was used to demonstrated the importance of junctional contractility regulation in epithelial barrier formation and concomitantly showed that αE-catenin experiences forces of at least 1–6 pN in AJs of epithelial cells (Acharya et al. 2017).

In FAs, talin and vinculin are the best studied proteins regarding force analysis with tension sensors, whereas so far only one study using integrin subunit-specific tension sensors showed, that in migrating T-cells the integrin subunit β2 transduces actin-derived tension, requiring intact kindlin- and talin-binding (Nordenfelt et al. 2016). Talin tension was measured by Austen et al. (2015) using the HP35 and HP35st linker peptides. Their study revealed, that talin molecules bear forces of 6–8 pN with a proportion experiencing even forces of up to 11 pN. Importantly, talin seems to be involved in extracellular rigidity sensing, since talin tension was gradually reduced together with cell spreading area upon seeding of talin tension sensor (Tln-TS) expressing cells on substrates with decreasing stiffness (Kumar et al. 2016; Austen et al. 2015). Notably, this ability seems to be independent of vinculin expression, whereas the promotion of higher tension on talin requires reinforcement by vinculin. Furthermore, an internal force gradient within the talin rod domain was discovered by a multiplexing approach and confirmed the previously determined importance of its actin binding site 2 for transduction of high forces (Ringer et al. 2017b; Kumar et al. 2016). Interestingly, tension sensor experiments on talin-1 and talin-2 uncovered talin isoform-specific force transduction, as the recruitment of vinculin to talin-2 was shown to be independent of preceding force generation by actin and led to increased force-levels on talin-2 (Austen et al. 2015). Importantly, a study using transgenic talin tension sensor flies demonstrated that, *in vivo*, only a small proportion of talin are under tension at the same time at muscle attachment sites. Since reduction of the talin pool led to muscle–tendon rupture, most likely induced by active muscle contraction in the adult fly, this reservoir of temporarily unstretched talin molecules seems to be essential for high tissue forces (Lemke et al. 2019).

Vinculin was the first protein to be analyzed in a single molecule calibrated genetically encoded tension sensors study, which revealed that vinculin is exposed in average to 2.5 pN force in stable FAs by using the F40 linker (Grashoff et al. 2010). Since then, the V-TS has been used exemplarily to investigate the nature of cellular tension by elucidating the plastic relationship of vinculin tension, cell shape stability, adhesive load and adhesion complex area (Chang and Kumar 2013; Hernández-Varas et al. 2015). Upon the development of linker peptides with higher force sensitivity, measurements with HP35-based vinculin (V-TS) and metavinculin tension sensors (M-TS) demonstrated forces of at least 6–8 pN on both splice isoforms (Kluger 2016). Likewise, vinculin was found bearing tension of at least 1–6 pN in AJs of the zonula adherens of epithelial cell sheets and in collectively migrating neural crest cells (Leerberg et al. 2014; Kuriyama et al. 2014). Moreover, studies analyzing vinculin conformation and protein turnover in dependence of vinculin tension at FAs and AJs using the F40-based V-TS, suggested that vinculin activation and mechanical engagement are regulated separately from each other (Grashoff et al. 2010; Leerberg et al. 2014; Rothenberg et al. 2018). The V-TS was also one of the first tension sensors used to study physiologically more relevant mechanical processes

Recently, the V-TS was used to study the pathologically very important process of tumor metastasis by analyzing the influence of mechanical stimulation of osteocytes on motility and vinculin tension in breast cancer cells (Li et al. 2019). Finally, the first transgenic mammalian tension sensor model was successfully generated in form of a F40-based V-TS expressing mouse line, therefore paving the way to the analysis of tension in living mammalian organisms (Tao et al. 2019).

Together, these studies demonstrate the versatile application possibilities for genetically encoded FRET-based tension sensors, which in the future not only will help to decipher the biophysical principles underlying cellular contractility and mechanosensing, but also to deepen our understanding of their role in biological processes.

1.5 AIM OF STUDY

Numerous studies have established a crucial and prevailing role of vinculin in mechanotransduction in cells and organisms. In contrast, comparably few studies exist on its muscle-specific splice variant metavinculin, which has been associated with cardiomyopathies. Even though several biochemical and structural studies revealed splice isoform specific differences in binding and bundling of F-actin, the role of metavinculin in mechanotransduction remains obscure. To determine whether and how forces are transduced in a splice isoform-specific manner, this study focuses on the analysis of the mechanics of metavinculin in comparison to vinculin in FAs using a set of piconewton-sensitive tension sensors. First, a splice isoform-specific difference in force experienced by (meta)vinculin is established and the specificity of the measurements is thoroughly controlled. Next, the range and magnitude of forces experienced by (meta)vinculin is investigated. Followingly, the influence of vinculin and metavinculin expression on force propagation across the integrin–talin linkage, more specifically talin 1 and talin 2, in FAs is explored. Moreover, the influence of activation on force transduction across (meta)vinculin is investigated in mutational experiments.

Furthermore, metavinculin is widely considered a cardiomyopathy gene, even though its role in heart function and disorder is still undefined. Therefore, a metavinculin knock-out mouse model is characterized under normal and pathological conditions of the transverse aortic constriction model leading to pressure overload-induced cardiac hypertrophy. Additionally, the influence of the cardiomyopathy-associated R975W mutation in metavinculin is analyzed in transgenic mice.

2 MATERIALS AND METHODS

2.1 MOLECULAR BIOLOGY METHODS

Sequences of constructs used in this study are based on plasmids containing the first generation of V-TS and M-TS previously generated by Dr. Carleen Kluger (Kluger 2016). These plasmids were generated by overlap extension polymerase chain reaction (PCR) using human vinculin cDNA sequence NM_003373 (https://www.ncbi.nlm.nih.gov/nuccore/NM_003373) as a template, while the metavinculin tail was added using a synthesized oligonucleotide (MWG Biotech) encoding aa 874–1134, based on sequence NM_014000 (https://www.ncbi.nlm.nih.gov/nuccore/NM_014000). In contrast to the first generation, the current V- and M-TS constructs contain the fluorescent donor YPet instead of Venus. Consequently, they comprise the TS modules YPet-F40-mCherry (Addgene, 101252), YPet-FL-mCherry (Addgene, 101170), YPet-HP35-mCherry (Addgene, 101250) and YPet-HP35st-mCherry (Addgene, 101251) each flanked by short linkers at the N-terminus (aa LE) and the C-terminus (aa AAA) inserted into the proline-rich linker region between aa 883 and aa 884 of vinculin and metavinculin. The no-force controls correspond to the respective tension sensor, but were cut off after the mCherry fluorophore and ended with a stop codon, therefore lacking aa 884–1066(1134). The donor-only control consists of the V-TS containing only the fluorophore YPet at the position of the TS module, while TagBFP (Evrogen) was added at the end of the tail encoding sequence of (meta)vinculin. Mutations in the sequence of the V-TS or M-TS were generated using mutated overlapping Gibson primers. All constructs used in this study (Table 1) were assembled by Gibson Assembly (see 2.1.6) into the modified retroviral expression plasmid pLPCX (Clontech, 631511) and cloning strategies were designed using the software SnapGene (version 4.2.1.1).

2.1.1 Polymerase chain reaction (PCR)

Touch down PCR with PfuUltra II Fusion High-fidelity DNA Polymerase (Agilent, 600674) was used to generate the DNA fragments which were later assembled by Gibson Assembly. In this type of PCR, the annealing temperature is gradually decreased over the first 10 cycles to reduce the risk of unspecific primer binding to the template DNA at high temperatures while maintaining reaction efficiency at low temperature (Table 2 and Table 3). During the course of this thesis, this protocol was replaced by PCR reactions with the improved Phusion™ High-Fidelity DNA-Polymerase (Thermo Fisher, F534S) showing reduced error rates and allowing a faster PCR protocol (Table 4 and Table 5). Primers contained 18–22 base pairs complementary to the template DNA with an according melting temperature (T_m) of ~60 °C and a Gibson overlap (see 2.1.6) ending with G or C at their 3’ end. Sequences are listed in Table 6.

TABLE 1: GENERATED AND USED EXPRESSION PLASMIDS

no.	name
32	pGEX IpaA (DeMali/Burridge)
413	pLPCXmod + hTalin-1 (wt)-YPet(short).STOP
417	pLPCXmod + hTalin-2 (wt)-YPet(short).STOP
445	pLPCXmod + Vinculin-TagBFP.STOP
446	pLPCXmod + MetaVinculin-TagBFP.STOP
472	pLPCXmod + hTalin-1 (wt)-[YPet(short)-Villin-mCherry].STOP
475	pLPCXmod + hTalin-1 (wt)-[YPet(short)-Villin-mCherry] (internal)
477	pLPCXmod + hTalin-2 (wt)-[YPet(short)-Villin-mCherry].STOP
480	pLPCXmod + hTalin-2 (wt)-[YPet(short)-Villin-mCherry] (internal)
767	pLPCXmod + Vinculin-[YPet(short)-F40-mCherry] (internal)
768	pLPCXmod + Vinculin (head)-[YPet(short)-F40-mCherry].STOP
769	pLPCXmod + Vinculin-[YPet(short)-Villin-mCherry] (internal)
770	pLPCXmod + Vinculin (head)-[YPet(short)-Villin-mCherry].STOP
771	pLPCXmod + Vinculin-[YPet(short)-st.Villin-mCherry] (internal)
772	pLPCXmod + Vinculin (head)-[YPet(short)-st.Villin-mCherry].STOP
773	pLPCXmod + Vinculin-[YPet(short)-FL-mCherry] (internal)
774	pLPCXmod + Vinculin (head)-[YPet(short)-FL-mCherry].STOP
777	pLPCXmod + MetaVinculin-[YPet(short)-F40-mCherry] (internal)
778	pLPCXmod + MetaVinculin-[YPet(short)-Villin-mCherry] (internal)
779	pLPCXmod + MetaVinculin-[YPet(short)-st.Villin-mCherry] (internal)
780	pLPCXmod + MetaVinculin-[YPet(short)-FL-mCherry] (internal)
783	pLPCXmod + Vinculin-YPet(short) (internal)
883	pLPCXmod + Vinculin (I997A)-[YPet(short)-FL-mCherry] (internal)
884	pLPCXmod + MetaVinculin (I1065A)-[YPet(short)-FL-mCherry] (internal)
914	pLPCXmod + Vinculin (I997A)-TagBFP.STOP
915	pLPCXmod + Metavinculin (I1065A)-TagBFP.STOP
926	pLPCXmod + Vinculin (I997A)-[YPet(short)-st.Villin-mCherry] (internal)
927	pLPCXmod + MetaVinculin (I1065A)-[YPet(short)-st.Villin-mCherry] (internal)
956	pLPCXmod + Vinculin-[YPet(short)-F7-mCherry] (internal)
958	pLPCXmod + MetaVinculin-[YPet(short)-F7-mCherry] (internal)
1134	pLPCXmod + Vinculin (N773A,E775A)-[YPet(short)-FL-mCherry] (internal-883)
1135	pLPCXmod + MetaVinculin (N773A,E775A)-[YPet(short)-FL-mCherry] (internal-883)
1136	pLPCXmod + MetaVinculin (N773A,E775A)(1-883)-[YPet(short)-FL-mCherry].STOP
1137	pLPCXmod + Vinculin (A50I)-[YPet(short)-FL-mCherry] (internal-883)
1138	pLPCXmod + MetaVinculin (A50I)-[YPet(short)-FL-mCherry] (internal-883)
1139	pLPCXmod + Vinculin (A50I)(1-883)-[YPet(short)-FL-mCherry].STOP
1174	pLPCXmod + Vinculin (N773A,E775A)-[YPet(short)-F40-mCherry] (internal-883)
1175	pLPCXmod + MetaVinculin (N773A,E775A)-[YPet(short)-F40-mCherry] (internal-883)
1176	pLPCXmod + MetaVinculin (N773A,E775A)(1-883)-[YPet(short)-F40-mCherry].STOP
1177	pLPCXmod + Vinculin (A50I)-[YPet(short)-F40-mCherry] (internal-883)
1178	pLPCXmod + MetaVinculin (A50I)-[YPet(short)-F40-mCherry] (internal-883)
1179	pLPCXmod + Vinculin (A50I)(1-883)-[YPet(short)-F40-mCherry].STOP

no. is the inventory number in the Grashoff laboratory

TABLE 2: PCR REACTION MIX – PFU

component	volume	final concentration
PfuUltra II reaction buffer (10x)	5 µl	1x
forward primer (10 µM)	1 µl	0.2 µM
reverse primer (10 µM)	1 µl	0.2 µM
dNTPs (deoxyribonucleoside triphosphate, each 10 mM)	1 µl	each 0.2 mM
plasmid DNA template	X µl	5–30 ng
PfuUltra fusion HS DNA Polymerase (2.5 U/µl)	1 µl	0.05 U/µl
ddH_2O	fill to 50 µl	

TABLE 3: TOUCHDOWN PCR PROGRAM – PFU

name	temperature	time	no. of cycles
initial denaturation	95 °C	3 min	1 x
denaturation	95 °C	20s	
primer annealing	lowest primer Tm -5°C + 10 °C -> decrease by 1 °C each cycle	20 s	10 x
elongation	72°C	15 s/1 kb*	
denaturation	95 °C	20 s	
primer annealing	Tm-5 °C	20 s	30 x
elongation	72 °C	15 s/1 kb*	
final elongation	72 °C	3 min	1 x
storage	10 °C	∞	

* 15 s for targets ≤1 kb, 15 s/1 kb for targets >1kb and ≤10 kb, 30s/1 kb for targets > 10 kb

TABLE 4: PCR REACTION MIX – PHUSION

component	volume	final concentration
Phusion Green HF Buffer (5x)	10 µl	1x
forward primer (10 µM)	1 µl	0.2 µM
reverse primer (10 µM)	1 µl	0.2 µM
dNTPs (each 10 mM)	1 µl	each 0.2 mM
plasmid DNA template	X µl	1 pg–10 ng
Phusion DNA polymerase	0.5 µl	0.05 U/µl
ddH_2O	fill to 50 µl	

TABLE 5: PCR PROGRAM – PHUSION

name	temperature	time	no. of cycles
initial denaturation	98 °C	3 min	1 x
denaturation	98 °C	10 s	
primer annealing	lowest Tm + 3 °C*	20 s	30 x
elongation	72 °C	15 s/1 kb	
final elongation	72 °C	8 min	1 x
storage	4 °C	∞	

*when lowest primer Tm ≥ 72 °C primer annealing step was omitted leading to a 2-step protocol

TABLE 6: GIBSON ASSEMBLY PRIMERS

no.	name	sequence
V1	G_Vin(pLPCX)_f	CGCTAGCGCTACCGGACTCAACCATGCCAGTGTTTCATACGC
V2	G_Vin(pLPCX)_r	TTTATTTTATCGATGTATAGGCTCACTGGTACCAGGGAGTCTTTCTAACC
V4	G_Vin(YPet)_r	CCATCTCGAGTTCATCCTTTTCCTCTGGTGGTG
V5	G_YPet(VH)_f	AAAGGATGAACTCGAGATGGTGAGCAAAGGCGAAG
V6	G_cherry(VT)_r	CCGCGGCCGCCTTGTACAGCTCGTCCATG
V7	G_Vin(mC)_f	GCTGTACAAGGCGGCCGCGGAGTTCC
V8	G_cherry(pLPCX)_r	TCTTTTATTTTATCGATGTATAGGCTCACTTGTACAGCTCGTCCATGCC
V10	G_Vin(YPet)_f	GCCGCCGCAGCCGCGGAGTTCCCTG
V11	G_YPet_r	CGCGGCTGCGGCGGCGGTCAGG
V15	G_Vint(I997A)_r	CTGTGGACAGGGCTTTGAGCTGGGTGCTTATGG
V16	G_Vint(I997A)_f	CCATAAGCACCCAGCTCAAAGCCCTGTCCACAG
V18	G_tagBFP(pLPCX)_r	TTTATTTTATCGATGTATAGGCGGCCGCTTAATTAAGTTTGTG

no. is the inventory number in the Grashoff laboratory

TABLE 7: GENOTYPING PCR MASTER MIX

component	volume	final concentration
Phire master mix (2x)	10 µl	1x
forward primer (10 µM)	1 µl	0.5 µM
reverse primer 1 (10 µM)	1 µl	0.5 µM
(reverse primer 2 (10 µM))	1 µl	0.5 µM
genomic tail DNA	1 µl	
ddH_2O	fill to 20 µl	

TABLE 8: GENOTYPING PCR PROGRAM

name	temperature	time	no. of cycles
initial denaturation	98 °C	3 min	1 x
denaturation	98 °C	10 s	
primer annealing + elongation	72 °C	20 s	30 x
final elongation	72 °C	8 min	1 x
storage	4 °C	∞	

TABLE 9: GENOTYPING PRIMERS

no.	name	sequence
317	MV_gen_lox1_f	CCGAGGTGTAGGGTTTTCACTGC
319	MV_gen_lox2_f	ACTCATTATCTGTGCGGGTCCTGTG
320	MV_gen_lox2_r	GGAGCCAAGCAAAGCTCAGTGG
580	MV_gen_lox1_new_r	AATGGCATGCTCTCCAGGAGC

2.1.2 Genotyping PCR

To determine the genotype of mice, a tail biopsy was taken upon weaning. Genomic DNA was extracted using the Phire™ Tissue Direct PCR Master Mix (Thermo Fisher, F170S). Therefore, the tail biopsy was placed in 20 µl Dilution buffer mixed with 0.5 µl DNARelease additive and incubated for 2–5 min at room temperature (RT) followed by 2 min at 98 °C. Genotyping PCR was performed directly on 1 µl of the solution (Table 7). Genotyping PCR of transgenic mice $M^{(R975W)}$ comprised primer no. 319 and no. 320 and generated a bigger fragment 400 bp on the transgenic allele R975W and a smaller fragment on the wild type allele of 312 bp. Genotyping of $M^{(-/-)}$ mice involved three primers no. 317, no. 580 and no. 320. PCR reaction on the KO allele generated a smaller fragment of 245 bp and on the wild type allele a bigger fragment of 504 bp, while the potential large fragment of 1207 bp is not generated due to short extension step in the PCR program (Table 8, Table 9 and Figure 7).

2.1.3 Quantitative real time polymerase chain reaction (qRT-PCR)

Quantitative real time polymerase chain reaction (qRT-PCR) is employed to assess the expression level of a gene of interest by quantifying the amount of mRNA present in a sample. To this end RNA was extracted from snap frozen left ventricular tissues of sham- and TAC-operated wild type and $M^{(-/-)}$ mice with PureLink RNA Mini Kit (ambion, life technologies) following the subsection "purifying RNA from animal tissue" of the manufacturers protocol. An ULTRA-TURRAX T8 disperser (IKA) was used to homogenize the ventricular tissue in 500–600 µl lysis buffer. RNA concentration was evaluated on a NanoDrop 2000 UV-Vis (Thermo Fisher) and purity of the sample was verified as $OD_{260/280}$>1.8. Complementary DNA (cDNA) was generated by reverse transcribing 500 ng extracted RNA using the Rnase H based iScript cDNA Synthesis Kit (Bio-Rad Laboratories, 1708890). Resulting cDNA was stored at -20 °C until usage.

Quantitative PCR was performed in triplicates on 0.5 µl cDNA using iQ SYBR Green Supermix (BioRad, 170–8880) on a Light Cycler 480 (Roche) in which the reaction progress is monitored by detection of the fluorophore SYBR Green binding to double stranded DNA (Table 10 and Table 11). Primers for q-PCR reaction were synthetized by Eurofins MWG Operon and sequences are listed in Table 12.

TABLE 10: QPCR REACTION MIXTURE

component	volume	final concentration
iQ™ SYBER® Green supermix (2x)	10 µl	1x
forward primer (10 µM)	0.2 µl	0.1 µM
reverse primer (10 µM)	0.2 µl	0.1 µM
cDNA template (1:10 dilution)	5 µl	
RNAse free H_2O	4.6 µl	
total reaction mix volume	20 µl	

TABLE 11: QPCR THERMAL CYCLING PROTOCOL

reaction step	temperature	time	no. of cycles
Initial denaturation	95 °C	3 min	
denaturation	95 °C	15 s	40 x
annealing/extension	60 °C	30 s	

TABLE 12: QPCR PRIMER SEQUENCES

Nr.	Name	sequence
V33	qPCR_mNppa_f	GCTTCCAGGCCATATTGGAG
V34	qPCR_mNppa_r	GGGGGCATGACCTCATCTT
V35	qPCR_mMyh6_f	GCCCAGTACCTCCGAAAGTC
V36	qPCR_mMyh6_r	GCCTTAACATACTCCTCCTTGTC
V37	qPCR_mMyh7_f	ACTGTCAACACTAAGAGGGTCA
V38	qPCR_mMyh7_r	TTGGATGATTTGATCTTCCAGGG
V39	qPCR_mNPPB_f	CCCAAAAAGAGTCCTTCGGTC
V40	qPCR_mNPPB_r	CGGTCTATCTTGTGCCCAAAG
V41	qPCR_mACTA1_f	CCCAAAGCTAACCGGGAGAAG
V42	qPCR_mACTA1_r	CCAGAATCCAACACGATGCC
V43	qPCR_mCol1A1_f	CTGGCAAGAAGGGAGATGA
V44	qPCR_mCol1A1_r	CACCATCCAAACCACTGAAA
V45	qPCR_mCol1A2_f	AGGTCTTCCTGGAGCTGATG
V46	qPCR_mCol1A2_r	ACCCACAGGGCCTTCTTTAC
V47	qPCR_mCol3A1_f	ACAGCAAATTCACTTACACAGTTC
V48	qPCR_mCol3A1_r	CTCATTGCCTTGCGTGTTT
V49	qPCR_mRPL32_f	ACATCGGTTATGGGAGCAAC
V50	qPCR_mRPL32_r	GGGATTGGTGACTCTGATGG

Nr. Is the inventory number in the Grashoff laboratory

Gene expression was quantified using the 2–δδ–CT method (Livak and Schmittgen 2001), which assumes that amplification efficiency of primers differ by less than 5% and a gene amplification efficiency is near to 100% in the exponential phase. Therefore, the average cycle threshold (Ct), which is defined as the number of cycles required for the fluorescent signal to exceed the background level, was determined for each technical sample triplicate excluding values leading to a spread >0.5. The relative gene expression was calculated by normalizing the fold change of the gene of interest to the one of the constitutively expressed housekeeping gene ribosomal protein L32 (*RPL32)* according to equation 2.

$$\text{Relative gene expression} = 2^{(Ct_{gene} - Ct_{housekeeper})} \quad (2)$$

Followingly, the relative expression of the gene of interest in ventricle tissue of TAC operated mice was normalized to the average relative gene expression of wild type sham-operated littermates.

2.1.4 DNA separation and purification

DNA fragments were separated by agarose gel electrophoresis to analyze their size or to separate them from enzyme mixtures. 1% agarose (Thermo Fisher, 16500500) was cooked in 1x tris-acetate-EDTA (TAE) buffer (Table 13) and mixed with ethidium bromide (1:20,000, Sigma, E1510) to allow visualization of DNA bands under ultraviolet light. DNA samples mixed with gel loading dye (NEB, B7024S) were run together with a 1 kb DNA ladder (NEB, N3232) at 130 V. Genotyping PCRs were analyzed on 2% agarose gels and compared to a Quick-Load® Purple 2-Log DNA Ladder (NEB, N0550S). For cloning, bands of desired size were cut out and DNA was extracted using a gel purification kit (Macherey-Nagel, 740412).

TABLE 13: TAE BUFFER 50X

Component	stock concentration	final concentration	amount
Tris-base	121 g/mol	2 M	242 g
glacial acetic acid	1.05 g/l	60 mM	57.1 ml
EDTA (ethlyenediaminetetraacetic acid, pH 8)	0.5 M	50 mM	100 ml
ddH_2O*			fill to 1 l

* ddH_2O for agarose gels, dH_2O for running buffer

2.1.5 DNA digestion

DNA digestion was performed either to linearize the backbone for Gibson assembly or to test correct assembly of the plasmid by restriction enzyme analysis. The vector was linearized by the restriction enzymes NotI (NEB, R0189L) and BglII (NEB, R0144S) for at least 1 h at 37 °C (Table 14). To prevent self-religation of the digested plasmids, dephosphorylation was performed by adding two times 1 µl calf intestine alkaline phosphatase (CiP) (NEB, M0290) for 30 min at 37 °C. The linearized DNA was purified by agarose gel electrophoresis before Gibson Assembly (see 2.1.4 and 2.1.6).

TABLE 14: RESTRICTION ENZYME REACTION MIXTURE – PLASMID LINEARIZATION

component	volume	final concentration
NEB buffer 3.1 (10x)	4 µl	1x
plasmid DNA template	X µl	2 µg
NotI (10,000 units/ml)	1 µl	250 units/ml
BglII (10,000 units/ml)	1 µl	250 units/ml
dd H_2O	add to 40 µl	

TABLE 15: RESTRICTION ENZYME REACTION MIXTURE – CONTROL DIGEST

component	volume	final concentration
NEB buffer (10x)	3 µl	1x
plasmid DNA	X µl	0.8 – 1 µg
enzyme 1 (10,000 units/ml)	0.5 µl	333 units/ml
enzyme 2 (10,000 units/ml)	0.5 µl	333 units/ml
dd H_2O	add to 30 µl	

To verify correct Gibson Assembly, control digests of DNA extracted from bacterial cultures (see 2.1.7) was performed for 30 min – 1h at 37 °C with one or a combination of two restriction enzymes (Table 15): ClaI (NEB, R0197L), KpnI (NEB, R0142S or R3142S (HF)), SacI (NEB, R3156S), SalI (HF, NEB, R3138S), XbaI (NEB, R0145S). The characteristic band patterns observed upon separation of the DNA fragments of the digest by agarose gel electrophoresis (see 2.1.4) were compared using the software SnapGene and allowed the delimitation of potentially correctly assembled samples, which were then sent for sequencing (see 2.1.7).

2.1.6 Gibson assembly

Gibson assembly cloning allows seamless assembly of multiple overlapping DNA fragments in an isothermal reaction (Gibson et al. 2009). The reaction mixture contains three enzymes: (i) an exonuclease chewing back the 5' ends of the DNA fragments, thereby creating sticky overhangs, which can then anneal; (ii) a DNA polymerase extending the 3' ends of the DNA fragments; and (iii) a DNA ligase sealing the nicks and leading to a seamlessly joined plasmid DNA. All constructs generated during the course of this thesis were assembled by Gibson Assembly using the NEBuilder® HiFi DNA Assembly Master Mix (New EnglandBiolabs, E2621L). Prior to assembly, specific DNA fragments with overlapping sequences of 20–25 bp with a Tm of ~50 °C were designed and amplified by PCR (see 2.1.1). 2–4 DNA fragments were assembled into the linearized retroviral expression plasmid pLPCX (Clontech, 631511) after the Cytomegalovirus (CMV) promotor in a 1:2 molar ratio (typically 6.25 fmol vector + 12.5 fmol insert each) in 10 µl NEBuilder HiFi DNA Assembly Master Mix (total volume 20 µl) at 50 °C for 1h. 2 – 10 µl of the Gibson Assembly mixture were transformed into competent bacteria (see 2.1.7).

2.1.7 Transformation, amplification and sequence verification

Freshly assembled or preexisting plasmids were amplified in competent *Escherichia coli (E. coli)* (One Shot™ OmniMAX™ 2 T1R, Thermo Fisher, C854003). Competent bacteria were generated by growing a bacterial colony, picked from a Luria broth (LB) agar (Roth, 6675) plate containing 10 µg/ml tetracycline (Tet, Sigma, 87128), in 10 ml LB (Roth, 6673) medium with the same concentration of Tet. After 16 h, 100 ml warm LB medium without antibiotics were inoculated with 2 ml of this starter culture and grown to an OD_{550} of 0.5. After cooling for 10 min on ice and centrifugation for 15 min at 1100 g at 4 °C, the culture pellets were resuspended in 10 ml ice-cold transformation and storage solution (TSS, Table 16) containing 2.5 ml sterile glycerol. Aliquots of 100 µl were snap-frozen in liquid nitrogen and stored at -80 °C for up to 6 months.

TABLE 16: TRANSFORMATION AND STORAGE SOLUTION (TSS)

Component	stock concentration	final concentration	amount
Tryptone-peptone		1.0%	5.0 g
yeast extract		0.5%	2.5 g
NaCl	58.44 g/mol	100 mM	2.5 g
PEG (polyethylene glycol)	3000 – 3500 g/mol	10%	50 g
DMSO (dimethyl sulfoxide)	100%	5%	25 ml
$MgCl_2$	1 mM	50 mM	25 ml
ddH_2O			add to 500 ml

pH 6.5, sterile filtered, stored at 4 °C

For transformation by heat shock, an aliquot of competent bacteria was taken from -80 °C and thawed on ice. 2–10 µl assembled DNA mix resulting from Gibson assembly were added to the bacteria and incubated for 30 min on ice. Plasmid uptake was facilitated by a heat shock in a 42 °C warm water bath for 75 s. Subsequently, samples were cooled down for 3 min on ice followed by shaking in 900 µl prewarmed antibiotic-free LB medium at 37 °C for 60 min. Next, bacteria were pelleted for 3 min at 4500 g, resuspended in 100 µl LB, plated on a prewarmed LB plate supplemented with 75 µg/µl ampicillin (Sigma, A9518) and incubated at 37 °C overnight. For retransformation of plasmids, 0.5–1 µg DNA were transformed into one bacterial aliquot (100 µl) and 50 µl were plated directly after heat shock and recovery omitting the centrifugation step.

In order to analyze the assembled DNA, the following day, 4–8 colonies were inoculated in 4 ml LB medium supplemented with 75 µg/µl ampicillin overnight at 37 °C while shaking. While the small leftovers of the bacterial culture were stored at 4 °C, a little less than 4 ml of the bacterial culture were centrifuged at 4500 g for 3 min and DNA was extracted from the resulting pellets using the NucleoSpin® Plasmid EasyPure kit (Machinery-Nagel) following manufacturers protocol. DNA concentration was determined using a NanoDrop 2000 UV-Vis (Thermo Fischer) and DNA was stored at 4 °C (short term) or -20 °C (long term). Bacterial cultures containing correctly assembled DNA plasmids were first delimited by restriction enzyme digest (see 2.1.5) and then verified by sequencing using Mix2Seq kits (Eurofins Genomics). Therefore, 0.75–1.5 µg DNA were mixed with 20 pmol primer (Table 17) in 17 µl total volume. Resulting sequences were compared to the predicted sequence with the software SnapGene. Previously stored leftover of the identified bacterial culture stored at 4 °C was inoculated into 250 ml LB medium supplemented with 75 µg/µl ampicillin, grown overnight at 37 °C while shaking. Subsequently bacteria were pelleted at 4500 g for 15 min and plasmid DNA was extracted using the NucleoBond® Xtra Midi Plus kit (Machinery-Nagel) following manufacturers protocol. After DNA concentration was determined (see above), the DNA was aliquoted and stored at -20 °C until further use for transfection (see 2.2.2 and 2.2.3).

TABLE 17: SEQUENCING PRIMERS

no.	Name	sequence
47	pLPCX_seq_f	AGCTCGTTTAGTGAACCGTCAGATC
48	pLPCX_seq_r	ACCTACAGGTGGGGTCTTTCATTCCC
62	EGFP_Venus_seq_f	GATCCGCCACAACATCGAGGACGG
63	Cherry_BamH_f	ATAGGATCCATGGTGAGCAAGGGCGAGGAGG
75	2.YPet_Xho_f	GCCTCGAGATGGTGAGCAAAGGCGAAGAGC
77	2.delYPet_Bam_r	GCGGATCCGGCGGCGGTCAGGAACTCCAG
248	MV_seq_L_5	AAGGAGACTTAGGTTGGAGGC
V9	Vinc_seq_p2_r	CTGAGATGCAAGTGCTCGTG
V16	G_Vint(I997A)_f	CCATAAGCACCCAGCTCAAAGCCCTGTCCACAG
V26	Vinc_seq_p1b	CTAAGATGGCCAAGATGATTGACG
C3	vinc_Xba_wostp_r	CGCTCTAGACTGGTACCAGGGAGTCTTTCTAACC
C4	vin_p1	CTT GGG CCA GAT TGA CGA G
C6	vin_p3	ACAGTGGATGACCGTGGAGT
C7	vin_p4	AGCTGCTTATGAACATTTTGAGA
A42	Seq_Cherry590_f	CCTACAACGTCAACATCAAGTTGG
A41	Seq_YPet_595_f	CCACTACCTGAGCTACCAGAGCGC

Nr. is the inventory number in the Grashoff laboratory

2.2 CELL PREPARATION

2.2.1 Cell culture

Vinculin-deficient mouse embryonic fibroblasts (vinc$^{(-/-)}$) were previously generated by Dr. Carleen Kluger. SV40 large T immortalized fibroblasts carrying a *loxP* flanked *vinculin* gene (vinc$^{(fl/fl)}$, Thievessen et al. 2013) were transduced with Cre recombinase and a clonal cell line with the most similar morphological features to the parental cell line was isolated (Kluger 2016). The vinc$^{(-/-)}$, talin-deficient mouse kidney fibroblasts (tln1$^{-/-}$tln2$^{-/-}$; Theodosiou et al. 2016; Austen et al. 2013) and HEK293 cells (Phoenix cells; AmphoPack 293 cell line, Clontech - Takara Bio Europe, 631505) were cultured at 37 °C and 5% CO_2 in feeding medium containing high glucose (DMEM-GlutaMAX™ medium, Thermo Fisher Scientific, 31966047) supplemented with 10% fetal bovine serum (FBS, Thermo Fisher Scientific, 10270-106). Cells cultured in T75 flasks were split upon reaching confluency every 3–4 days in a ratio of 1:4 by adding 1 ml trypsin–EDTA (Sigma, T3924) after washing in 8 ml Dulbecco's phosphate buffered saline (PBS, Sigma, D8537). After the cells detached they were resuspended in prewarmed feeding medium, centrifuged at 170 g for 4 min and the pellet was resuspended in the desired amount of feeding medium. For freezing, the cells were resuspended in 6 ml freezing medium (Table 18) and divided into 4 tubes, which were stored at -80 °C or transferred to liquid nitrogen at least 1 day later for long term storage.

TABLE 18: FREEZING MEDIUM

Component	supplier, catalog num.	final concentration	volume
feeding medium	see text	40%	20 ml
FBS	Thermo Fisher, 10270-106	50%	25 ml
DMSO	Roth, 4720	10%	5 ml

2.2.2 Transient transfection

Transient expression of V-/M-TS or tagged proteins was accomplished by transient transfection with the cationic lipid transfection reagents Lipofectamine 2000 (Thermo Fisher Scientific, 11668019) or Lipofectamine 3000 (Thermo Fisher Scientific, L3000015) using aliquoted DNA, which underwent less than three thaw/freezing cycles. For transfection with Lipofectamine 2000, 10 µl lipofectamine 2000 reagent and 3 µg DNA were each vortexed in 250 µl Opti-MEM® and incubated for 5 min. The combined mixture was inverted few times and incubated for 20 min at RT. For transfection with Lipofectamine 3000, 7.5 µl lipofectamine 3000 reagent were vortexed in 125 µl Opti-MEM® and added to 2–3 µg DNA mixed with 125 µl Opti-MEM® and 4–6 µl P3000 reagent. The mixture was inverted few times and incubated for 10–15 min at RT. In both cases the medium on cells at 70–90% confluency in 6-wells was changed to 1 ml feeding medium. The DNA-lipid-mixtures were added dropwise to the cells and the dish was softly shaken to ensure equal distribution. The next day, the transiently transfected cells were seeded for imaging (see 2.4.1 and 2.4.2).

2.2.3 Stable infection

Due to poor expression efficiency by transient transfection, experiments with Tln-TS relied on cell lines stably expressing Tln-TS constructs. Stable infection was accomplished using the retroviral infection system and retroviral packaging Phoenix cell line (see 2.2.1; Swift et al. 2001). For each infection one 80% confluent 10 cm dish of Phoenix cells was transfected with the construct of interest by calcium chloride phosphate co-precipitation. Therefore, 20 µg DNA were mixed in 500 µl ddH_2O containing 244 mM $CaCl_2$, and DNA was precipitated by adding 500 µl 2x HBS buffer (Table 20) dropwise to the mixture while vortexing. Next, DNA precipitates were dripped onto the phoenix cells pre-incubated in feeding medium containing 25 µM chloroquine to reduce degradation of transfected DNA. The medium was changed back to feeding medium 6–8 h later.

The next day, medium of a 10 cm dish of vinc$^{(-/-)}$ target cells grown to ~60% confluency was exchanged for the filtered supernatant of the phoenix cells containing the ecotropic retroviral particles and 5 µg/ml of the infection enhancing compound polybrene, while the phoenix cells received fresh feeding medium. After five infection cycles every 12 h, cells were selected with 2 µg/ml puromycin.

TABLE 19: HBS BUFFER (PH 7.0) 2X

Component	stock concentration	final concentration	amount
NaCl	58.44 g/mol	280 mM	8 g
HEPES	238.30 g/mol	50 mM	6 g
Na_2HPO_4	141.96 g/mol	1.5 mM	0.1 g
ddH_2O			fill to 500 ml

2.3 BIOCHEMICAL METHODS

2.3.1 Cell lysis

Mouse tissues were homogenized with an ULTRA-TURRAX T8 disperser (IKA) for 3 times 30 s with 30 s breaks on ice in 500 µl lysis buffer (Table 21). The disperser was washed in between samples in 0.5 M NaOH, followed by 70% EtOH and ddH_2O to avoid contamination between samples. Following centrifugation for 10 min at 16,000 g at 4°C, protein concentration in the supernatant was determined using the bicinchoninic acid-based BCA Protein Assay Kit (Merck, 71288). The colorimetric reaction was detected at 562 nm with a plate reader (Tecan, Sunrise with Magellan software version 7.2) and protein concentration of the cell lysates were calculated from the intensity values and normalized to the concurrently measured BSA standard curve (0.5–2 mg/ml in lysis buffer). The concentration was adjusted to 2 mg/ml with lysis buffer and samples supplemented with 4x Laemmli loading buffer (Table 22) were denatured for 5 min at 98 °C. As metavinculin is especially prone to degradation in ventricular tissue lysates, the samples were frozen directly at -80 °C after lysis and analyzed within the following week.

TABLE 20: LYSIS BUFFER

Component	stock concentration	final concentration	volume
Tris/HCl pH 7.5	1 M	50 mM	0.5 ml
NaCl	1 M	150 mM	1.5 ml
Triton X-100	100%	1%	100 µl
SDS (sodium dodecyl sulfate)	20%	0.2%	100 µl
protease inhibitor cocktail*			1 tablet dissolved in 2 ml ddH_2O
ddH_2O			5.8 ml

* cOmplete ULTRA, mini, EDTA-free EASYpack, Roche, 5892791001

TABLE 21: LAEMMLI LOADING BUFFER (4X)

Component	stock concentration	final concentration	volume
Tris pH 6.8	1 M	200 mM	10 ml
EDTA	0.5 M	4 mM	400 µl
Glycerol	100%	40%	20 ml
SDS	20%	4%	10 ml
Bromphenol blue	669.96 g/mol		1 pinch (until color turns to deep blue)
ddH_2O			fill to 50 ml
β-mercaptoethanol	100%	4%	40 µl added to working aliquot of 1 ml buffer

2.3.2 Actin co-sedimentation assay

The ability of (meta)vinculin to co-sediment actin in the presence and absence of the bacterial vinculin activator IpaA was used to assess the activation of the two splice variants. First, the GST-tagged protein IpaA was recombinantly expressed in bacteria and purified from inclusion bodies by dialysis according to a previously published protocol (Chen et al. 2005) by Ina Kowsky. Next, a confluent 10 cm dish of HEK293 cells was transfected with the (meta)vinculin construct of interest by calcium chloride phosphate co-precipitation (see 2.2.3). The next day a hypotonic cell lysate was generated by mechanically detaching the cells in PBS, centrifuging them at 1000 g for 3 min at 4 °C and resuspending the pellet in 1.5 ml ice-cold hypotonic lysis buffer. Following incubation for 20 min on ice and homogenization with a Dounce homogenizer, the lysates were cleared by centrifugation at 16,000 g for 10 min at 4 °C. The total supernatant (T) was supplemented with 100 mM KCl and 5 µM actin from rabbit muscle (Sigma, A2522) and incubated in the presence or absence of 1 µM GST-IpaA for 20 min on ice. While 60 µl of T supplemented with 4x Laemmli loading buffer (Table 22) were denatured for 5 min at 98 °C, the rest of the sample was subjected to ultra-centrifugation at 135,000 g for 30 min (TLA-110 rotor, Beckman-Coulter). The soluble fraction (S) was collected and denatured equally, whereas the pellet fraction (P) was first washed once in hypotonic lysis buffer and then directly resuspended in 1x Laemmli loading buffer followed by denaturation. Actin co-sedimentation assay was evaluated by loading 2% of the denatured fraction T and S as well as 10% of the fraction P in SDS-PAGE and Western blot analysis (see 2.3.3 and 2.3.4). Actin co-sedimentation assays were performed together with Prof. Dr. Carsten Grashoff.

TABLE 22: HYPOTONIC LYSIS BUFFER

Component	stock concentration	final concentration	volume
Tris pH 7.5		20 mM	
$MgCl_2$		2 mM	
EGTA		0.2 mM	
DTT		0.5 mM	
ATP		0.5 mM	
protease inhibitor cocktail*			2 tablet dissolved in 2 ml ddH_2O
ddH_2O			

* cOmplete ULTRA, mini, EDTA free EASYpack, Roche, 5892791001

2.3.3 SDS polyacrylamide gel electrophoresis (SDS-PAGE)

SDS-PAGE is used to separate proteins according to their molecular mass eliminating the effect of structure and charge by binding to the strongly negatively charged anionic detergent sodium dodecyl sulfate (SDS). A separation gel with 8% (or 12% for connexin-43 western blots) polyacrylamide (PAA, Serva, 10688) (Table 23) was polymerized in 1.5 mm wide and 10 cm long homemade chambers covered by isopropanol. After polymerization isopropanol was discarded and a stacking gel with 6% PAA (Table 24) to increase band resolution was polymerized on top containing the comb. The gels were placed in SDS-PAGE running buffer (Table 25) and equal amounts of protein from each sample were separated next to 10 µl Spectra Multicolor High Range Protein Ladder (Thermo Fisher, 26625) or PageRuler Plus Prestained Protein Ladder (Thermo Fisher, 26619) at 120 V–180 V. In order to better detect the very small amount of metavinculin in ventricular tissue samples, the distance between vinculin and metavinculin bands was increased by using a PerfectBlue Vertical Dual Gel Systems Twin M (VWR, 700-0961/700-0955).

TABLE 23: SEPARATING GEL

Component	stock concentration	final concentration	volume
Tris/HCl pH 8.8	1.5 M	0.375 M	2.5 ml
PAA	30%	8%/12%	2.7 ml/4 ml
SDS	20%	0.1%	50 µl
APS (ammonium persulfate)	10%	0.1%	100 µl
TEMED (N,N,N',N'-tetramethylethylenediamine)	100%	0.1%	10 µl
ddH_2O			4.6 ml/3.4 ml

TABLE 24: STACKING GEL

Component	stock concentration	final concentration	volume
Tris/HCl pH 6.8	1.5 M	0.225 M	0.75 ml
PAA	30%	6%	1 ml
SDS	20%	0.1%	25 µl
APS	10%	0.1%	50 µl
TEMED	100%	0.1%	5 µl
ddH_2O			3.2 ml

TABLE 25: SDS-PAGE RUNNING BUFFER

Component	stock concentration	final concentration	volume
Western Blot Running Buffer 10x (Table 26)			100 ml
SDS	20%	0.1%	5 ml
ddH_2O			fill to 1 l

TABLE 26: WESTERN BLOT RUNNING BUFFER 10X

Component	stock concentration	final concentration	amount
Trizma®-Base	121.14 g/mol	0.25 M	30.2 g
glycine	75.07 g/mol	1.92 M	144 g
ddH_2O			fill to 1 l

2.3.4 Western blot

To ensure efficient transfer of high molecular weight proteins, the proteins were transferred from a PAA-gel to a polyvinylidenfluorid (PVDF) membrane (Merck, IPVH00010) by tank blotting. Therefore, the gel was assembled into a sandwich onto a PVDF membrane, which was pre-activated and equilibrated in methanol, and in between Whatman paper and sponges. All components were equilibrated in blotting buffer containing methanol (Table 27) during assembly to avoid air bubbles. The blot was immersed completely in blotting buffer and run at 30 V and 50 mA overnight at 4 °C including a cooling unit while stirring.

TABLE 27: WESTERN BLOT BLOTTING BUFFER

Component	stock concentration	final concentration	volume
Western Blot Running Buffer 10x (Table 26)	10x	1x	100 ml
methanol	100%	20%	200 ml
ddH_2O			fill to 1 l

Afterwards, the membrane was washed in TBS-T (Table 28) and blocked in blocking buffer containing 5% skim milk (AppliChem, A0830) or 5% BSA (Pan Biotech, P06-1391100) in TBS-T as indicated for 4 h at 4 °C or 1 h at RT to block unspecific binding sites. Subsequently, the membrane was incubated with primary antibodies (Table 30) overnight at 4°C, washed in TBS-T (5 x 5 min) and incubated with secondary antibodies conjugated to horseradish peroxidase (Table 31) in blocking buffer for 1.5 h. Following washing in TBS-T (5 x 5 min), bands were detected by the enhanced chemiluminescence detection system Immobilon Western HRP Substrat Kit (Merck, WBKLS0500) on a luminescent image analyzer (GE Healthcare, ImageQuant LAS-4000). Images were adjusted linearly to reduce background using Fiji (Schindelin et al. 2012). In blots showing metavinculin bands in ventricle tissue samples the background was subtracted by a rolling ball algorithm with a radius of 3.7 cm (= 500 px) to allow better distinction of the weak metavinculin band as in respect to the strong vinculin band. Densitometric quantification was performed only on Western Blots with clearly different band intensities.

TABLE 28: TBS BUFFER WITH TWEEN-20 (TBS-T)

Component	stock concentration	final concentration	volume
TBS Buffer 10x (Table 29)	10x	1x	100 ml
Tween-20	100%	0.1%	1 ml
ddH_2O			fill to 1l

TABLE 29: TBS BUFFER (PH 7.6) 10X

Component	stock concentration	final concentration	amount
Trizma®-Base	121.14 g/mol	0.2 M	24.2 g
NaCl	58.44 g/mol	1.5 M	88.0 g
ddH_2O			fill to 1 l

2.4 MICROSCOPY AND IMAGING

2.4.1 Immunofluorescence

For immunofluorescence analysis of transfected vinc$^{(-/-)}$ cells, cells were seeded on fibronectin-coated (10 µg/ml, Merck, 341631) glass slides (Menzel, #1.5) and allowed to spread for 4h in the incubator. After fixation in 4% paraformaldehyde (PFA) in PBS for 10 min at RT and washing 3 x 5 min in PBS, unspecific binding sites were blocked using blocking buffer (2% BSA and 0.1% Triton X-100 in PBS) overnight at 4 °C. Following incubation for 3 h at RT or overnight at 4 °C with 1st antibodies in blocking buffer (Table 30) and washing 3 x 5 min in PBS, cells were incubated in 2nd antibodies (Table 31) at RT in blocking buffer. Subsequently, cells were incubation with 4',6-diamidino-2-phenylindole (DAPI) in PBS for 7 min to stain nuclei, washed 3 x 5 min in PBS and mounted with Prolong Gold (Thermo Fisher Scientific, P36934) to prevent fading of the fluorophores. Samples were stored at 4 °C in the dark to avoid bleaching of the fluorophores. Images were acquired on a confocal laser scanning microscope (Leica TCS SP5 X with Leica Application Suite Advanced Fluorescence, version 2.7.3.9723, or Zeiss LSM 880 with ZEN Software, black edition) equipped with an 63x oil objective (HCX PL APO lambda blue, oil, NA=1.4).

For immunofluorescence of ventricular tissue, ventricles of mice were fixed for at least 2 h in 4% PFA right after isolation and cryoprotected in 30% sucrose overnight. The next day, ventricles were embedded in Shandon Cryomatrix (Thermo Fisher Scientific, 6769006) in cryomolds (tissue-tek, 4557 and 4566) and stored on -80 °C. 5 µm sections were cut on a cryostat (Thermo Fisher, CryoStar™ NX70), air dried for ~ 30 min and placed in -80 °C for short term storage. To reduce the cross-linking of epitopes by PFA treatment, sections were unmasked by heat-induced antigen retrieval. Therefore, sections were rehydrated in PBS for 3 x 5 min, while antigen retrieval buffer (Table 32) was heated until boiling in a plastic chamber in the microwave at maximum power. After cool down for 3 min at RT, sections were transferred into the hot antigen retrieval buffer and cooked for 6–12 min at 145 Watt. Subsequently, sections inside the hot antigen retrieval buffer were allowed to cool down at RT for 20 min. After permeabilization in 0.2% Triton X-100 in PBS for 20 min, tissue sections were blocked for 1 h in 5% BSA (Pan Biotech, P06-1391100) in PBS and incubated with 1st antibodies (Table 30) in 1.5% BSA in PBS at 4 °C overnight. After incubation with 2nd antibodies (Table 31) in 1.5% BSA in PBS for 2 h at RT, sections were stained with DAPI in PBS for 7 min and mounted with fluorescence mounting medium (Elvanol). Each described step was separated by washing 3 x 5 min in PBS. Images of tissue stainings were acquired using a LSM780 confocal scanning microscope (Zeiss) equipped with a 20× objective (air, NA 0.8) for ICD and gap junction markers and a 40× objective (oil,

NA 1.4) for costamere markers using zoom 2, 1024 x 1024 px^2, a laser scanning velocity of 7 Hz and a line average of 4.

TABLE 30: PRIMARY ANTIBODIES

antigen (clone)	species	supplier, catalog num.	dilution for IF	dilution for WB
actin (sarcomeric)	mouse	Sigma, A2172		1:1000
α-catenin	rabbit	Sigma, C2081	1:400–200	1:4000
β-catenin	rabbit	Sigma, C2206	1:400	1:4000
connexin-43	rabbit	Cell Signaling Technologies, 3512	1:400	1:4000 in BSA
dystrophin	rabbit	abcam, ab15277	1:200	1:500
integrin β1 M-B1.2	rat	Millipore, MAB1997	1:400	-
integrin β1D 2B1	rat	abcam, ab8991	-	1:1000
N-cadherin (3B9)	mouse	Thermo Fisher Scientific, 33-3900	1:500	1:2000
paxillin	mouse	BD Transduction Laboratories, 610051/2	1:400–200	-
talin-1 (97H6)	mouse	Bio-Rad, MCA4770	-	1:1000
talin-2 (68E7)	mouse	abcam, ab105458	-	1:2000
tubulin (DM1A)	mouse	Sigma, T6199	-	1:3000
(meta)vinculin (hVIN-1)	mouse	Sigma, C2081	1:400	1:4000

TABLE 31: SECONDARY ANTIBODIES AND REAGENTS

antigen	label	supplier, catalog num.	dilution for IF	dilution for WB
mouse IgG	Alexa-405	Invitrogen, A31553	1:500	
rabbit IgG	Alexa-405	Invitrogen, A31556	1:500	
rabbit IgG	Alexa-488	Invitrogen, A21441	1:500	
rat IgG	Alexa-488	Invitrogen, A11006	1:500	
mouse IgG	Alexa-568	Invitrogen, A11004	1:500	
rabbit IgG	Alexa-568	Invitrogen, A11036	1:500	
mouse IgG	Alexa-647	Invitrogen, A21235	1:500	
mouse IgG	HRP	BioRad, 170-6516		1:10,000
rabbit IgG	HRP	BioRad, 170-6515		1:10,000
phalloidin	Alexa-647	Invitrogen, A22287	1:200	
DAPI		Sigma, D8417	1:10,000	

TABLE 32: ANTIGEN RETRIEVAL BUFFER

Component	stock concentration	final concentration	volume
citric acid	0.1 M	1.8 mM	12.6 ml
sodium citrate	0.1 M	8.2 mM	57.4 ml
Tween-20	100%	0.05%	350 µl
ddH_2O			630 ml

2.4.2 Fluorescence lifetime imaging microscopy

FRET efficiencies of tension sensor experiments were evaluated using TCSPC-FLIM on live cells. Cells transiently expressing V-TS/M-TS constructs were seeded on fibronectin coated (10 µg/ml, Merck, 341631-5MG) glass bottom imaging dishes (Ibidi, 81158) one day after transient transfection and allowed to spread for 4–7 h. The medium was changed to DMEM without phenol red containing 25 mM HEPES, 4.5 mg/ml glucose and 2 mM glutamine (Thermo Fisher, 21063045) supplemented with 10% FBS at least 30 min before imaging. For analysis of (meta)vinculin tension upon Rho-associated protein kinase (ROCK) inhibition (Y-27632), cells were incubated with 25 µM Y-27632 inhibitor for 20 min followed by fixation in 4% PFA for 10 min before imaging to stop the reaction. $Tln1^{-/-}tln2^{-/-}$ cells transfected with the (meta)vinculin tension sensor set were seeded on glass bottom dishes coated with poly-L-Lysine (pLL, 0.1% (w/v), Sigma, P4707) for 15–240 min. Before imaging, the cells were treated with 10 µM Y-27632 inhibitor for 30 min. For FLIM of stably expressed Tln-TS combined with transient expression of BFP-tagged vinculin or metavinculin, cells were seeded as described above, but were allowed to spread for 20–30 h before imaging.

TCSPC-FLIM experiments were performed on two different confocal laser scanning microscopes. The first set-up was located at the Max-Planck Institute of Biochemistry in Martinsried, and consisted of a Leica TCS SP5 X laser scanning microscope (Leica Application Suite Advanced Fluorescence, Version 2.7.3.9723) equipped with a 63× objective (HCX PL APO CS, water, NA=1.2) and a heating chamber (37°C, 5% CO2; Ibidi). A pulsed white light laser with an 80 MHz repetition rate (NKT Photonics) was used at 508 nm to excite YPet at 70% laser intensity and the emitted fluorescence signal was filtered by a band-pass filter for YPet (545/30 nm, Chroma). Arrival time and spatial information for each photon were detected by a FLIM X16 TCSPC detector using the detector software Imspector Pro (LaVision Biotech). 20 FLIM image repeats with a total duration of 2.586 s each were acquired with a scanning velocity of 400 Hz on 512 × 512 pixels using zoom 2 thereby covering 123.02 × 123.02 μm^2. The second set-up was located at the Westfälische Wilhelms Universität Münster and comprised a Zeiss LSM 880 confocal scanning microscope (ZEN Software, black edition), which was equipped with a pulsed laser with a 40 MHz repetition rate for excitation at 510 nm (LDH-D-C-510), a 63× objective (glycerin, NA 1.2), and a 37°C heating chamber. FA images were acquired over 122.68 µm × 122.68 µm area (512x512 pixels) and photon arrival times were recorded with a FLIM module from PicoQuant (MultiHarp 150 4N; SymPhoTime 64 software, PicoQuant). For each experimental condition, 15–80 images were recorded on 2–6 consecutive days.

2.4.3 Analysis of TCSPC-FLIM data

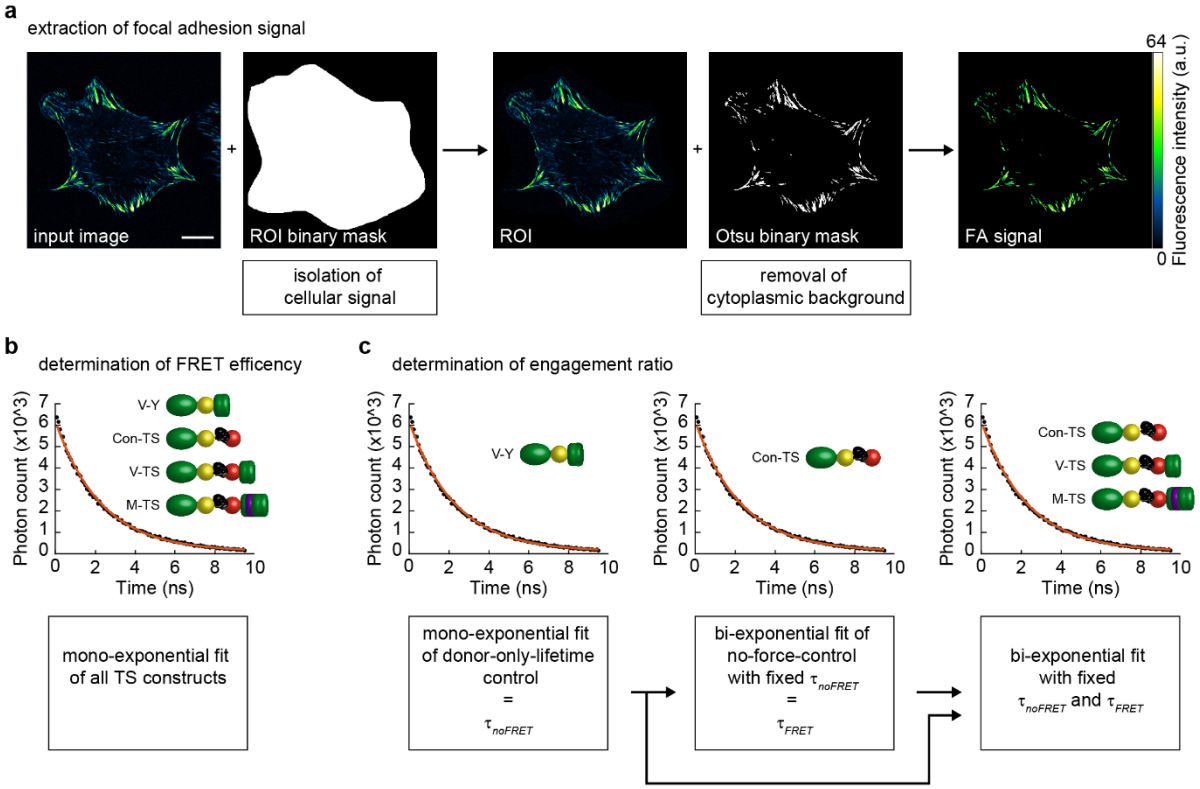

FIGURE 6: SCHEMATIC DEPICTION OF THE WORKFLOW FOR FA ANALYSIS OF FLIM-FRET DATA. **(a)** Exemplary FA extraction on an intensity image of a cell generated by summing the temporal information of the photon arrival times contained in the 20 image repeats of the raw FLIM-FRET data. After limiting the signal to a single cell by drawing a region of interest (ROI), the FA-specific signal is extracted by an automated two- or three-level multi-Otsu intensity thresholding algorithm followed by exclusion of resulting regions smaller than ~0.5 µm^2. The subsequently fitted lifetime consequently represents an average of the lifetimes of all isolated FAs within one individual cell and is represented by one dot in the boxplots. Scale bar: 20 µm. **(b)** To analyze FRET efficiencies, the photon count time trace (black dots) of each masked cell is fitted by a mono-exponential decay function (red line) to determine the fluorescence lifetime of the donor-only-lifetime control (V-Y), no-force control (Con-TS), vinculin tension sensor (V-TS) and metavinculin tension sensor (M-TS). **(c)** A three-step process is necessary to determine the molecular engagement ratio: First, τ_{noFRET} is approximated by determining the lifetime of V-Y using the mono-exponential fit as described in (b). Next, τ_{FRET} is determined as the short lifetime using a bi-exponential fit of the FLIM data of Con-TS with τ_{noFRET} as fixed parameter. Lastly, the molecular engagement ratios of Con-TS, V-TS and M-TS are estimated by fitting the respective FLIM data with a bi-exponential fit with fixed τ_{noFRET} and τ_{FRET}. To correct for fluorescently inactive acceptor fluorophores, the resulting ratios are rescaled to the engagement ratio of Con-TS. Note that (b) and (c) depict an example data set. Vinculin (green), metavinculin insert (purple), YPet donor fluorophore (yellow), mCherry acceptor fluorophore (red), mechanosensitive linker (black). Figure reproduced from Kanoldt et al. 2020.

Analysis of time-correlated single photon counting (TCSPC)-FLIM-data was performed using the custom-written automated MATLAB program Fluorescence Lifetime Analysis and Merge Software (FLAMES) written by Dr. Anna-Lena Schweizer run on MATLAB version R2017b (Cost 2019). To efficiently extract the FA signal (Figure 6a), first a region of interest (ROI) was drawn around single cells in the intensity image generated by summing the temporal information of the photon arrival times contained in the 20 image repeats of the raw FLIM-FRET data. Next, the highest intensity class of an automated binary two- (V-TS, M-TS and VY in vinc$^{(-/-)}$) or three-level (Con-TS, mutated V- and M-TS, all Tln-TS) multi-Otsu thresholding was isolated from the ROI and resulting regions smaller than ~0.5 µm^2 were excluded. Few particularly inefficiently masked images were excluded manually from further analysis. The thresholding efficiency depended on the contrast of the specific signal to the general or cytoplasmic background signal and the thresholding type was chosen once for each tension sensor construct under each experimental condition.

The photon time trace merged over all repeats and pixels within the masked cell was fitted by an exponential decay using MATLAB's 'fmincon' with a maximum-likelihood cost function based on Poisson statistics to determine the fluorescence lifetime (Figure 6b). The contribution of the instrument response function and autofluorescence to the signal was minimized by starting the fitting at 0.56 ns after the maximum photon count and fixing the fit length to 9.6 ns. Additionally, the lifetimes were required to have a relative fit error <10% to be included in further data analysis. The FRET efficiency E is defined as the percentage of photons contributing to FRET and was calculated from the mean donor-only lifetime $\overline{\tau_D}$ and the lifetime of the donor in presence of an acceptor τ_{DA}:

$$\mathrm{E} = 1 - \frac{\tau_{\mathrm{DA}}}{\overline{\tau_{\mathrm{D}}}} \tag{3}$$

$\overline{\tau_D}$ consisted of the median of the simultaneously measured donor-only lifetimes merged over the indicated experimental time span and was determined independently for each experimental data set.

To determine the molecular engagement ratio r_M, which is defined as the amount of mechanically engaged tension sensors M_{tensed} relative to the total number of tension sensor molecules M_{total}, the fluorescence lifetime decay acquired in FLIM experiments was fitted with a bi-exponential fitting algorithm (Figure 6c; Cost 2019; Ringer et al. 2017b; Lemke et al. 2019). The signal is assumed to be comprised of predominantly two lifetimes: the lifetime of the open and therefore mechanically engaged tension sensor τ_{noFRET}, and the lifetime of the closed not-engaged tension sensor τ_{FRET}, both of which can be approximated by control FLIM experiments. Due to the large contour length increase of the stretched linker peptide, τ_{noFRET} can be approximated by the mono-exponentially fitted lifetime of the donor alone. The signal of the no-force control FLIM data consists of the lifetime of the fully

fluorescently active closed tension sensor τ_{noFRET} and the lifetime of tension sensors with fluorescently inactive mCherry acceptor corresponding to τ_{noFRET}. Thus, a biexponential fit with fixed τ_{noFRET} was applied to determine τ_{FRET} thereby including a ratio bounded between 0 and 1 to increase fitting robustness and requiring a minimum of 10,000 photons to increase fitting quality. By then fitting the FLIM data bi-exponentially with the two fixed lifetimes τ_{noFRET} and τ_{FRET}, the relative contribution of photons from molecules with these two lifetimes was obtained. The corresponding relative molecular engagement ratio r_M was derived by taking into account the loss of photons due to FRET. Finally, r_M was rescaled to the respective median of the no force control to account for the tension sensors with fluorescently inactive mCherry acceptor (non FRETing tension sensors).

To determine the relative number of tensed molecules (M_{tensed}), the total number of tension sensor molecules emitting the recorded fluorescent signal in the FLIM experiments (M_{total}) needs to be assessed. Since each tension sensor molecule contains deterministically one YPet fluorophore, the recorded photon count N_{total} can be used as an approximation when photon loss due to FRET is considered. The recorded photon count N_{total} stems from either tensed (N_{tensed}) or relaxed tension sensors ($N_{relaxed}$):

$$N_{total} = N_{tensed} + N_{relaxed} \tag{4}$$

The photon count N_{tensed} is directly proportional to the number of tensed molecules M_{tensed}, whereas the photon count $N_{relaxed}$ is comprised of the photons emitted by the relaxed tension sensor molecules ($N_{relaxedFRETcorr}$) diminished by the photons transferred to the acceptor fluorophore with the FRET efficiency E:

$$N_{relaxed} = N_{relaxedFRETcorr}(1 - E) \tag{5}$$

By combining and rewriting equations 3–5, the theoretical total photon count corrected for photon loss by FRET is

$$N_{FRETcorr} = N_{tensed} + N_{relaxedFRETcorr} = N_{tensed} + N_{relaxed}\frac{\tau_{\mathrm{D}}}{\tau_{\mathrm{DA}}} \tag{6}$$

Furthermore, the ratio r_N can be used to describe the relative contribution of N_{tensed} to the total photon count N_{total}:

$$N_{tensed} = r_N N_{total} \tag{7}$$

Therefore, the FRET-corrected total photon count can be rewritten as

$$N_{FRETcorr} = r_N N_{total} + (1 - r_N)N_{total}\frac{\tau_{\mathrm{D}}}{\tau_{\mathrm{DA}}} \tag{8}$$

By using the FRET-corrected total photon count $N_{FRETcorr}$ as an approximation for the absolute number of molecules M_{total}, the number of tensed tension-sensor molecules can then be calculated using the molecular engagement ratio r_M:

$$M_{tensed} = r_M N_{FRETcorr} \tag{9}$$

The FLIM data is visualized in boxplots generated by MATLAB's 'boxplot' in which one data point represents the merged signal of one cell. Furthermore, the boxplots show the median, 25th and 75th percentile and whiskers reaching to the last data point within 1.5× interquartile range corresponding to 2.7 standard deviation for normally distributed data. To evaluate the statistical significance of the FLIM data a two-sided Kolmogorov–Smirnov (KS) test with a default significance level of $\alpha = 0.05$ was used. Statistical significances are indicated by the p-value: *** $p < 0.001$; ** $p < 0.01$; * $p < 0.05$; n.s. (not significant): $p \geq 0.05$.

2.5 ANIMAL WORK

2.5.1 Generation of transgenic and knockout mouse strains

Generation of the transgenic mouse line $M^{(R975W)}$ introducing the putative cardiomyopathy point mutation R975W into the *Vcl* gene and the $M^{(-/-)}$ deleting the exon encoding the metavinculin insert (E-M) from the *Vcl* gene entirely, was accomplished in a combined targeting strategy by homologous recombination by Dr. Anna Chrostek-Grashoff (Figure 4). The targeting construct based on clone WTSIB741I19227Q of the BAC library generated from AB2.2 ES cell DNA (129S7/SvEvBrd-Hprtb-m2; Adams et al. 2005) encoded the E-M flanked by loxP-sites and included the point mutation R975W. A neomycin-resistance cassette (Neo) flanked by FRT-sites facilitated selection of successfully modified R1 ES cell clones, which were screened by Southern blot and injected into C57BL/6N host blastocysts. To generate the transgenic $M^{(R975W)}$ mice, the resulting chimera males were bred with female FLP-deleter mice (Tg(ACTFLPe)9205Dym; Rodríguez et al. 2000) removing the neomycin selection cassette in F1 generation. To generate knockout $M^{(-/-)}$ mice, the chimera males were bred with female Cre transgenic mice (Tg(Nes-cre)1Wme; Betz et al. 1996) removing the E-M together with the neomycin selection cassette in F1 generation. Heterozygous males of both F1 generations were crossed with C57BL/6N wild type females to breed out the Flp and Cre transgene. Mutation of E-M in $M^{(R975W)}$ mice was confirmed by sequencing (see 2.1.7) and genotyping was performed according to 2.1.2. The mice were generated, bred and housed at the animal facility of the Max Planck Institute of Biochemistry in Martinsried, Germany under SPF barrier conditions (RT: 22 ± 1.5°C, relative humidity: 55 ± 5%, lighting: artificial with a light:dark cycle of 14:10 hours). All animal experiments were conducted in accordance with animal welfare laws and were approved by the Government of Upper Bavaria (55.2-1-54-2532-77-2015). Mouse data was compared by two-way analysis of variance (ANOVA) followed by Sidak's multiple comparison test using GraphPad Prism software package (version 6). Statistical significances are indicated by the p-value: *** $p < 0.001$; ** $p < 0.01$; * $p < 0.05$; n.s. (not significant): $p \geq 0.05$. To analyze whether heterozygous mice breed at Mendelian ratio, the chi-square test was used.

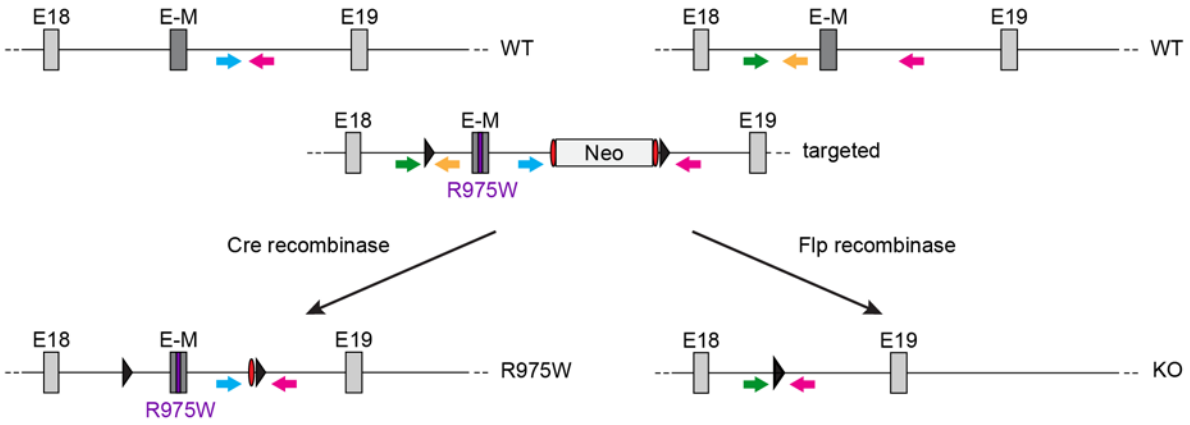

FIGURE 7: GENERATION OF TRANSGENIC $M^{(R975W)}$ AND KNOCKOUT MOUSE LINE $M^{(-/-)}$. Schematic depiction of the targeting strategy combining the generation of $M^{(R975W)}$ and $M^{(-/-)}$ mouse line: The metavinculin-specific exon (E-M) encoding the putative cardiomyopathy mutation R975W was flanked by loxP-sites (black triangles). A neomycin-resistance cassette (Neo) flanked by FRT-sites (red ovals) was added to enable selection of transgenic ES cell clones. Breeding of chimeric animals with FLP transgenic mice led to excision of Neo and resulted in the transgenic allele R975W. Excision of the loxP-flanked fragment including the mutated E-M and Neo, was accomplished by breeding with Cre transgenic mice resulting in the knock out (KO) allele. Genotyping PCR of $M^{(R975W)}$ mice was performed with two primers (blue and pink) generating a 400 bp-long fragment on the transgenic allele R975W and a 312 bp-long fragment on the wild type (WT) allele. Genotyping PCR of $M^{(-/-)}$ mice involved three primers (green, yellow, pink) generating a 504 bp-long fragment on the WT allele and a 245 bp-long fragment on the KO allele. Due to short extension step in the PCR program, the potential large fragment (green, pink) is not generated on the WT allele. Colored arrows represent genotyping primers no. 317 (green), no. 580 (yellow), no. 320 (pink) and no. 319 (blue). Modified figure reproduced from Kanoldt et al. 2020.

2.5.2 Transverse aortic constriction (TAC) model

Thoracic aortic constriction was performed in collaboration with the group of Prof. Dr. Dr. Stefan Engelhardt from the Institute of Pharmacology and Toxicology at the Technical University of Munich on 10 8-week-old male mice per group as described previously (Rockman et al. 1991) with small adaptations. 60 min before intubation mice received buprenorphine (0.8–0.1 mg/kg s.c.) and anesthesia with isoflurane. Thoracotomy was performed between the second and third rib, and the diameter of the aortic arch was reduced by 65–70% by a ligature over a 27 G cannula. Mice remained in a warmed cage for 2–4 h under direct supervision until complete recovery from anesthesia. To exclude effects caused by the surgery itself, a control group was sham operated meaning, that they were treated equally except ligation of the aorta. Pulse-wave Doppler echocardiography on a Vevo Imaging System (VisualSonics) was carried out before TAC/sham surgery and 4 weeks after surgery directly before animal euthanization and organ harvest to assess cardiac dimensions and function.

FIGURE 8: TRANSVERSE AORTIC CONSTRICTION (TAC) PROTOCOL. Time line of TAC protocol involving twenty wild type $M^{(+/+)}$ and twenty knockout $M^{(-/-)}$ 8-week-old male mice: Ten mice of each genotype were subjected to TAC or sham surgery and sacrificed 4 weeks later for organ harvest. All mice were examined by echocardiography before surgery and right before sacrifice. Modified figure reproduced from Kanoldt et al. 2020.

2.5.3 Tissue isolation and histopathology

For histology, dissected organs were incubated in 4% PFA at RT overnight. Following washing in PBS for 10 min, tissues were dehydrated in a series of different ethanol concentrations for 1 hour each (50%, 70%, 80%, 90%, 100%, 100%) followed by an additional 1.5 h in 100% ethanol. Next, tissues were incubated 2 x 15 min in xylene and then transferred into paraffin for 60 min. To remove all xylene, tissues were transferred for another 60 min and 90 min to fresh paraffin, before being embedded into the final paraffine block on a HistoStar™ Embedding Workstation (Thermo Fisher). Samples were stored at 4 °C. Paraffin blocks were sectioned into 6 µm slices on a microtome (Microm HM 355S, Thermo Fisher) using MX35 Premier microtome blades (34°/80 mm, Thermo Fisher).

For histological staining, tissue sections were deparaffinized for 2 x 5 min in xylene and rehydrated in a series of different ethanol concentrations (100%, 100%, 90%, 80%, 70%) and ddH_2O for 2–3 min each. Next tissues were incubated for 2 min in haematoxylin solution and rinsed 3 x in tap water. For counterstaining, sections were transferred into 0.2% eosin solution for 1 min. Finally, sections were dehydrated in the same series of ethanol concentrations as described above in reverse order and mounted in entellan. Sections were imaged on an Axioskop (Zeiss) with a 40x objective using Spot Software 5.1.

To visualize collagen depositions sections were treated as described above, but stained in 0.1% fast green staining solution for 20–30 min at RT. Staining was stopped in 1% acetic acid for 1 min, followed by washing in tap water for 5 min. Finally, sections were stained in 0.1% picrosirius red solution for at least 30 min. Dehydration was performed as above and sections were mounted in DEPEX (Merck). Ventricle sections were imaged on an Observer Z1 (Zeiss) with a 10× objective. Interstitial fibrosis was determined as the percentage of Sirius Red positive area excluding vessels, endo- and epicardium using the software MetaMorph 7.7.1.0.

3 RESULTS

3.1 THE ROLE OF METAVINCULIN IN FORCE TRANSDUCTION

3.1.1 Functionality of (meta)vinculin tension sensors

In a previous study by Dr. Carleen Kluger, force transduction across the vinculin isoforms was investigated using V-TS and M-TS as well as control constructs to determine the donor fluorophore lifetime and no-force control FRET efficiencies (Kluger 2016). In the present study, the tension sensor measurements were improved by integrating the optimized fluorophore FRET pair YPet and mCherry as well as all four available single molecule calibrated tension sensor linkers F40 (1–6 pN), FL (3–5 pN), HP35 (6–8 pN), and HP35st (9–11 pN). The resulting V-TS and M-TS contain the TS modules in between the head and tail domain within the flexible linker region after aa 883, whereas the donor-only lifetime control (V-Y) is comprised of vinculin containing only the donor fluorophore YPet at the analogous position (Figure 9). The no-force control (Con-TS) consists of the (meta)vinculin tension sensor lacking the actin-binding tail domain and therefore cannot transmit forces.

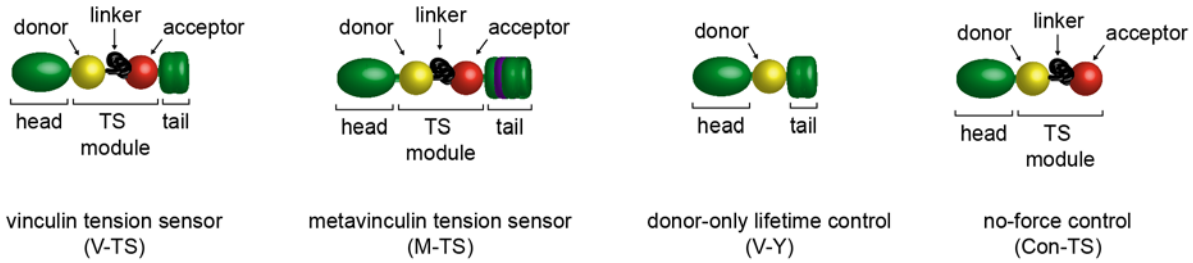

FIGURE 9: THE VINCULIN AND METAVINCULIN TENSION SENSORS. Schematic depiction of tension sensor constructs used for (meta)vinculin FRET-FLIM studies: the vinculin (V-TS) and the metavinculin (M-TS) tension sensor; the donor-only lifetime control construct containing only YPet at the tension sensor insertion site (V-Y); the no-force control tension sensor (Con-TS) lacking the actin binding tail domain. YPet donor fluorophore (yellow), mCherry acceptor fluorophore (red), vinculin (green), metavinculin insert (purple), mechanosensitive linker (black). Modified figure reproduced from Kanoldt et al. 2020.

Previous studies by Grashoff et al. (2010) and Kluger (2016) evaluated the functionality of V-TS and M-TS and identified a delayed spreading phenotype of early passage vinculin-deficient mouse embryonic fibroblasts (vinc$^{(-/-)}$), which was most prominent 2h after cell seeding on fibronectin. In the present study, immunostaining experiments confirmed that vinc$^{(-/-)}$ cells display a more rounded cell morphology as compared to their parental cells (vinc$^{(f/f)}$; Figure 10). Moreover, expression of V-TS or M-TS both rescued the spreading defect of the vinc$^{(-/-)}$ cells and both tension sensors showed the expected localization to FAs independently of each other.

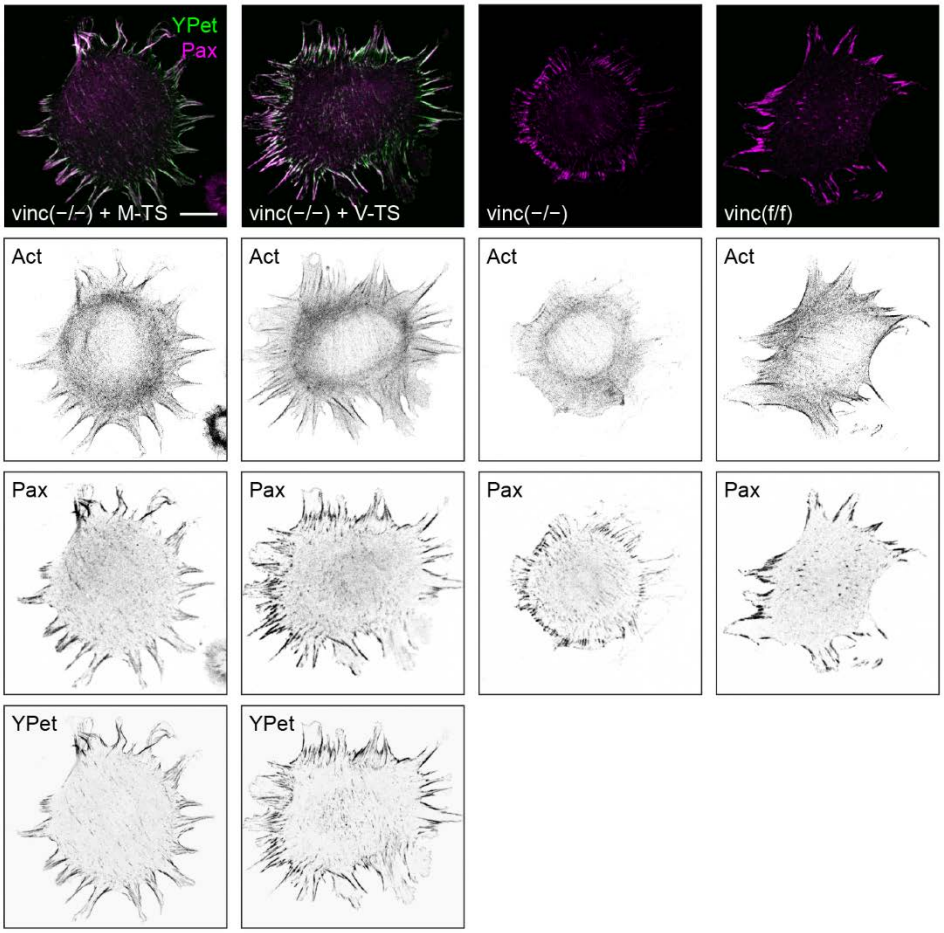

FIGURE 10: THE (META)VINCULIN TENSION SENSOR RESCUES THE SPREADING DEFECT OF VINCULIN-DEFICIENT CELLS. Representative images of vinc$^{(f/f)}$, vinc$^{(-/-)}$, and vinc$^{(-/-)}$ cells expressing vinculin (V-TS) or metavinculin (M-TS) tension sensors containing the FL module show that the tension sensors rescue the spreading defect of the vinc$^{(-/-)}$ cells seeded for 2 h on FN-coated glass slides. Note the comparably more rounded cell morphology of vinc$^{(-/-)}$ cells. Grey scale images depict the individual channels, the merge images show the YPet signal of the tension sensor in green and paxillin (Pax) in magenta. Scale bar: 20 µm. Modified figure reproduced from Kanoldt et al. 2020.

The ability of (meta)vinculin to bind most of its interaction partners depends on the release of its autoinhibition and metavinculin was shown to be more active than vinculin, which was attributed to the elongated linker region of metavinculin (see 1.2.2). Given that the insertion of the relatively bulky TS modules might also influence the activation of the two isoforms, an actin co-sedimentation assay using hypotonic cell lysates from HEK293 cells expressing V-TS, M-TS, and as a control vinculin (V-V) or metavinculin (M-V) C-terminally tagged with the fluorophore Venus was performed (Figure 11). In this *in vitro* assay, the activation of (meta)vinculin is triggered by the addition of the bacterial vinculin activator IpaA and the ability of the fusion proteins to co-sediment with actin upon ultracentrifugation is used as a measure of activation (Chen et al. 2005; DeMali et al. 2006). In accordance with previous experiments (Grashoff et al. 2010), the addition of IpaA triggered the expected activation response in all samples, characterized by an increase of (meta)vinculin fusion protein in the pellet fraction and a corresponding decrease in the soluble fraction (S). However, the amount of (meta)vinculin present in

the pellet fraction without addition of IpaA was slightly increased in the tension sensor samples. The additional secondary bands in the tension sensor samples were caused by a partial fragmentation of the DsRed-derived fluorophore mCherry upon processing for SDS-PAGE, as was observed before (Gross et al. 2000). Therefore, the insertion of the TS module seems to influence the activation of vinculin and metavinculin slightly, but does so equally in both isoforms, while the general activation response of the two splice isoforms remains unchanged. Together, these data confirm that tension sensor insertion does not constitutively activate (meta)vinculin, and that both tension sensors can compensate for the loss of endogenous vinculin regarding FA formation and cell spreading.

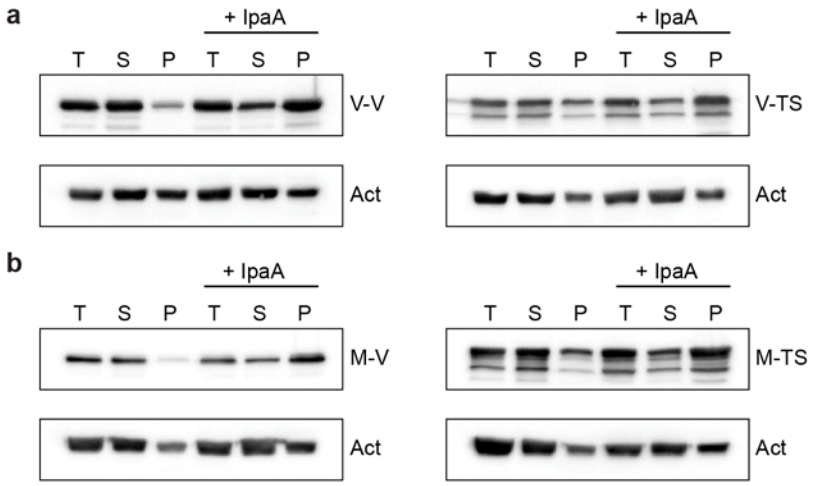

FIGURE 11: INSERTION OF THE TS MODULE DOES NOT CONSTITUTIVELY ACTIVATE (META)VINCULIN. Actin co-sedimentation assays comparing the ability of **(a)** vinculin C-terminally tagged with Venus (V-V) and vinculin tension sensor (V-TS) or **(b)** metavinculin C-terminally tagged with Venus (M-V) and metavinculin tension sensor (V-TS) to bind actin in the presence or absence of the vinculin activator IpaA. These results illustrate that insertion of the HP35st TS module does not lead to constitutive activation of (meta)vinculin. Total (T), soluble (S), pellet (P) fraction. Modified figure reproduced from Kanoldt et al. 2020. Western Blot was performed by Prof. Dr. Carsten Grashoff.

3.1.2 Force transduction in FAs is vinculin–isoform dependent

Tension sensor experiments were started using the most sensitive module FL, which responds to 3–5 pN force and requires less molecules under sufficient tension than the other modules to detect significant changes in FRET efficiency. All tension sensor constructs localized to FAs when expressed in vinc$^{(-/-)}$ cells including the Con-TS, which induced slightly hypertrophic FAs, as observed before (Figure 12; Humphries et al. 2007; Grashoff et al. 2010). In agreement with Dr. Kluger's previous data, a distinct FRET efficiency decrease for V-TS- and M-TS-expressing cells was observed, which was less pronounced for cells expressing M-TS (Figure 13a). Unexpectedly, the same effect could be observed repeating the experiment with the stiffest module HP35st, indicating that both, V-TS and M-TS, experience high forces of up to at least 9–11 pN (Figure 13b).

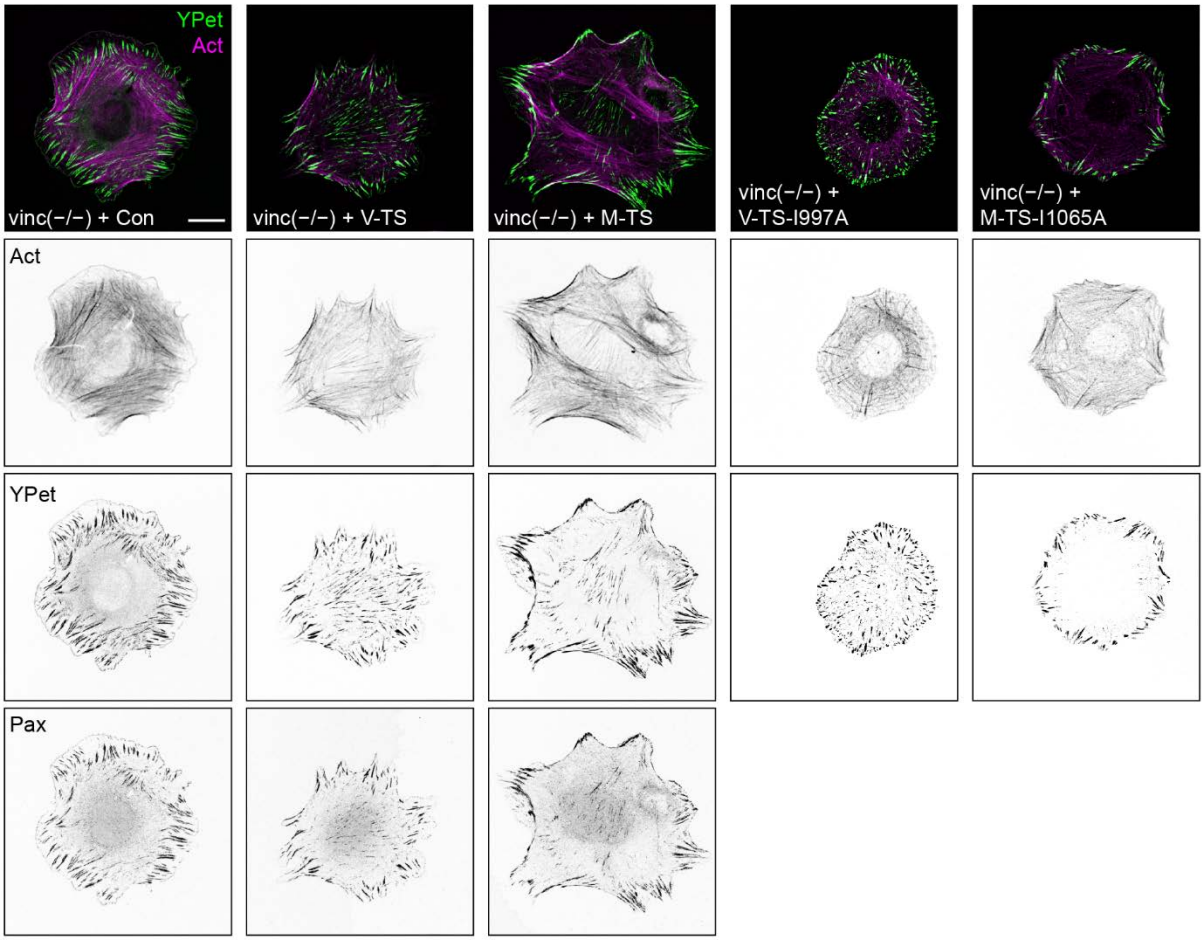

FIGURE 12: VINCULIN AND METAVINCULIN TENSION SENSORS LOCALIZE TO FAS. Representative images of vinc$^{(-/-)}$ cells expressing no-force control (Con-TS), vinculin (V-TS), metavinculin (M-TS) or actin binding deficient vinculin (V-TS-I997A) and metavinculin (M-TS-I1065A) tension sensors containing the FL module spreading for 4h on FN-coated glass slides. Grey scale images depict the individual channels, the merge images show the YPet signal of the tension sensor in green and actin (Act) in magenta. Scale bar: 20 µm. Modified figure reproduced from Kanoldt et al. 2020.

Since the FRET efficiency differences were consistent but rather small, an additional no-force control was employed to test the specificity of the observations. Dr. Kluger had introduced a point mutation (I997A) known to reduce actin binding of vinculin to 50% into V-TS (V-TS-I997A; see1.2.3). In the present study, this point mutation was also introduced into M-TS (I1065A, M-TS-I1065A) at the corresponding residue to reduce actin engagement (Figure 12d). V-TS-I997A and M-TS-I1065A localized to FAs, but, in contrast to Con-TS, did not seem to form hypertrophic FAs (Figure 12). The cell morphology of Con-TS, V-TS-I997A and M-TS-I1065A seemed more spherical and the actin fiber organization appeared distinct from V-TS and M-TS consisting of concentric actin stress fibers combined with a round slender actin mesh. Overall, the differences in cell morphology and actin cytoskeleton between the load bearing and unloaded tension sensors were rather small, supporting the previous observation that vinculin is dispensable for cell spreading (Thievessen et al. 2013).

Remarkably, FRET efficiencies of FL-based V-TS-I997A and M-TS-I1065A were both comparable to the no-force control level of Con-TS, indicating reduced force transmission across the tension sensors (Figure 13a). Also, the introduction of the actin binding mutations into HP35st-based V-TS and M-TS raised FRET efficiencies to almost no-force control levels of the respective Con-TS and ablated the splice isoform-specific differences (Figure 13b). Therefore, these mutation experiments show that the FRET difference between the two splice isoforms is dependent on actin engagement.

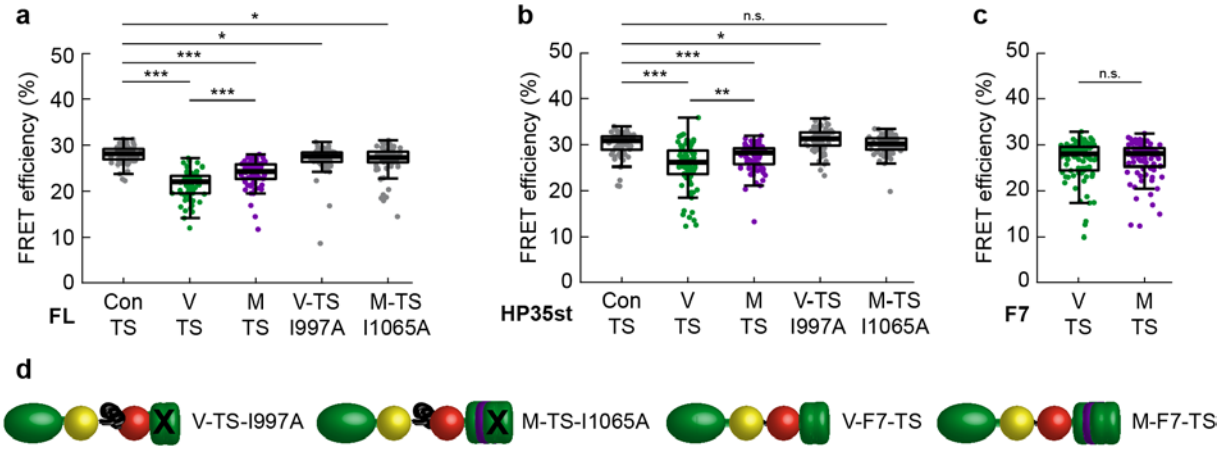

FIGURE 13: FORCE TRANSDUCTION IN FAS IS VINCULIN ISOFORM-DEPENDENT. (a) Live-cell FLIM measurements of vinc$^{(-/-)}$ cells expressing FL-based V-TS and M-TS sensitive to low forces of 3–5 pN show tension on both isoforms. Note the smaller reduction in FRET efficiency in M-TS expressing cells. A point mutation (I997A and I1065A) in the actin binding domain of vinculin and metavinculin strongly reduces tension and ablates isoform-specific differences (n=73, 73, 74, 72, 73 cells). **(b)** Analogous live-cell FLIM experiments using (meta)vinculin tension sensors based on HP35st module confirm the vinculin isoform-specific difference and reveal forces of up to 11 pN on both isoforms. Elevated FRET efficiency levels upon disruption of the actin-binding site support force specificity of observed effect (n=72, 77, 77, 75, 74 cells). **(c)** Live-cell FLIM measurements of vinc$^{(-/-)}$ cells expressing force-insensitive vinculin and metavinculin tension sensor controls demonstrate highly similar FRET efficiencies and confirm that vinculin isoform–specific effects are conformation-independent (n = 86, 85 cells). **(d)** Schematic depiction of mutant tension sensor constructs used to control the force specificity of the (meta)vinculin FRET-FLIM experiments: the actin-binding-impaired mutants of the vinculin (I997A, V-TS-I997A) and metavinculin (I1065A, M-TS-I1065A) tension sensors serving as additional no force controls; the F7-based force-insensitive vinculin (V-F7-TS) and metavinculin (M-F7-TS) tension sensor controls. YPet donor fluorophore (yellow), mCherry acceptor fluorophore (red), vinculin (green), metavinculin insert (purple), mechanosensitive linker (black). Boxplots show median, 25th and 75th percentile with whiskers reaching to the last data point within 1.5× interquartile range. Kolmogorov–Smirnov test: ***p < 0.001, **p < 0.01, 571 *p < 0.05, n.s. (not significant) p ≥ 0.05. Modified figure reproduced from (Kanoldt et al. 2020).

Even though metavinculin and vinculin have a very similar structure, their conformation might differ (see 1.2.2 and 1.2.3). This might influence the rotational freedom of the fluorophores of the TS module and, consequently, FRET (see 1.3.2). Therefore, the force sensitive linker peptide in the TS module of V-TS and M-TS was replaced by a 7-aa-long peptide (F7), which cannot be significantly elongated under force (Figure 13d). FRET efficiencies of the resulting force-insensitive V-F7-TS and M-F7-TS were highly similar, showing that the observed isoform-specific differences in FRET efficiencies are independent of (meta)vinculin conformation (Figure 13c).

To further test the force-specificity of the observed FRET efficiency differences, force-release experiments with the FL-based tension sensor set expressed in vinc$^{(-/-)}$ cells were performed using the ROCK inhibitor Y-27632 (Figure 13). Releasing tension within the cell leads to loss of vinculin from FAs (Carisey et al. 2013). Therefore, the concentration and time span of inhibition need to be chosen carefully in order to maintain the balance between a measurable tension decrease and a signal intensity that still can be evaluated by FLIM. Based on the parameters described by Rothenberg et al. (2018) V- and M-TS expressing cells were incubated with 25 µM Y-27632 for 20 min followed by fixation. Subsequent FLIM measurement evidenced an expected decrease in spreading and FA area (Figure 14a). Additionally, a reduction in fluorescent signal intensity indicated partial loss of (meta)vinculin from FAs.

In accordance with previous studies (Carisey et al. 2013), these effects were less pronounced in Con-TS expressing cells, which can be attributed to impaired autoinhibition of the no-force control due to absence of the (meta)vinculin tail domain. While the FRET efficiency level of Con-TS remained comparably constant, FRET efficiencies of V-TS and M-TS expressing cells were distinctly, but not significantly, elevated upon addition of Y-27632, which indicated the expected decrease in tension on the two splice isoforms (Figure 14b). The observed FRET changes are very small and therefore need to be confirmed in further experiments with either increased inhibitor concentration or inhibition time span to increase the measurable tension release effect. Nonetheless, these data suggest that ROCK-driven actomyosin contractility is at least in part responsible for the observed FRET efficiency difference of the (meta)vinculin tension sensors.

To further confirm the importance of intact force transmission, the FL-based tension sensor constructs were expressed in talin-deficient mouse kidney fibroblasts (tln1$^{-/-}$tln2$^{-/-}$), which do not form FAs due to the absence of talin. The cells were seeded on poly-L-Lysine (pLL)-coated dishes to allow cell attachment without spreading and treated additionally with Y-27632 to ensure the absence of forces. As expected, all constructs localized in the cytoplasm of the tln1$^{-/-}$tln2$^{-/-}$ cells and FLIM-FRET experiments did not reveal any significant differences between FRET efficiencies of Con-TS, V-TS and M-TS expressing cells (Figure 14c and d). The comparably high spread in FLIM data points can presumably be attributed to crowding effects and intermolecular FRET issues.

Together, these experiments demonstrate that the measured FRET decrease in V-TS and M-TS expressing cells is vinculin isoform-specific, dependent on force and probably mediated by a diverse engagement of the two isoforms with the actin cytoskeleton.

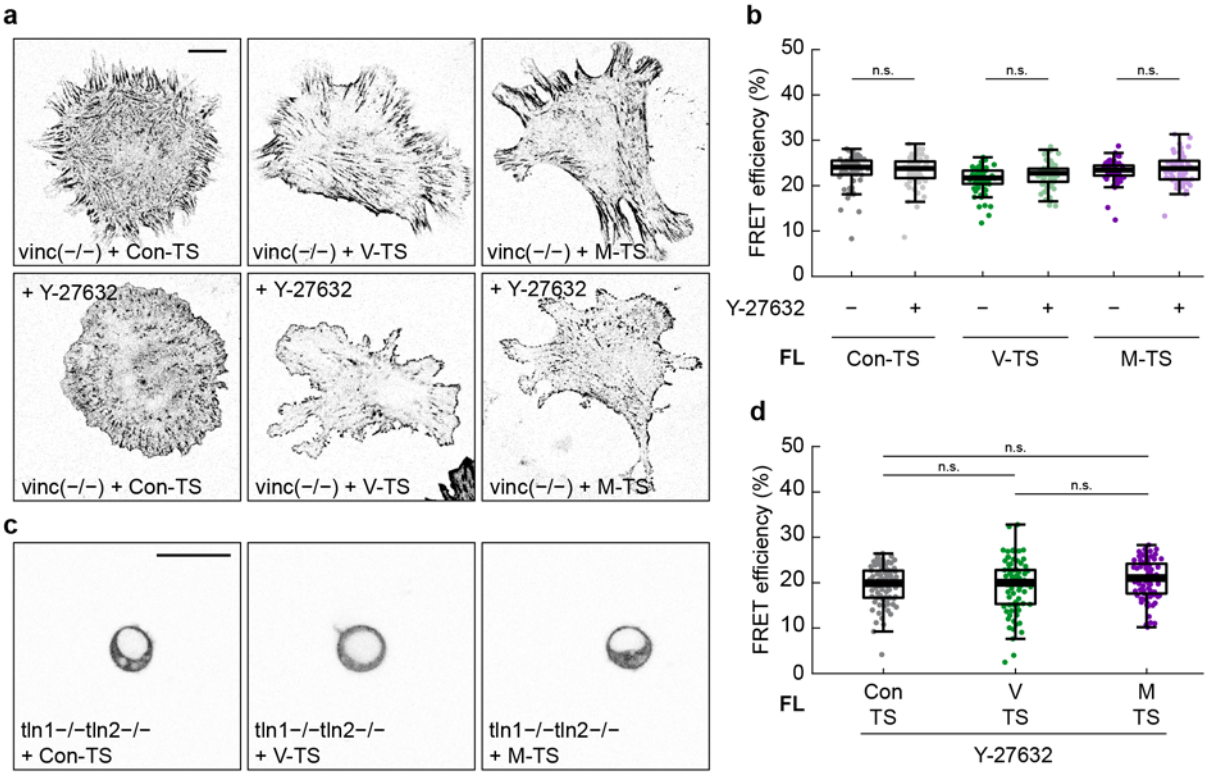

FIGURE 14: ISOFORM-SPECIFIC FORCE TRANSDUCTION IN FAS IS DEPENDENT ON ACTIN ENGAGEMENT. **(a)** Representative fluorescent images of vinc$^{(-/-)}$ cells expressing FL-based Con-TS, V-TS and M-TS show partial loss of FAs as well as signal intensity upon treatment with Y-27632. Grey-scale images depict summed photons acquired during a FLIM measurement depicted in (b). Scale bar: 20 µm. **(b)** FLIM measurements of fixed cells described in (a) show a slight increase in FRET efficiency specific to V-TS and M-TS upon treatment with Y-27632 indicating force release (n=62, 58, 63, 60, 62, 60 cells). **(c)** Representative fluorescent images of talin-deficient cells (tln1$^{-/-}$tln2$^{-/-}$) expressing FL-based Con-TS, V-TS and M-TS seeded on pLL-coated dishes and treated with Y-27632 show round cell morphology characteristic for absent FA attachment. Grey-scale images depict summed photons acquired during a FLIM measurement depicted in (d). Scale bar: 40 µm. **(d)** Live-cell FLIM measurements of cells described in (b) confirm that FRET efficiency differences are force specific (n=80, 80, 82 cells). Boxplots show median, 25th and 75th percentile with whiskers reaching to the last data point within 1.5× interquartile range. Kolmogorov–Smirnov test: ***p < 0.001, **p < 0.01, 571 *p < 0.05, n.s. (not significant) p ≥ 0.05. Modified figure reproduced from Kanoldt et al. 2020.

3.1.3 Metavinculin displays lower engagement ratio and higher force per molecule

To investigate the observed vinculin isoform specific FRET efficiency differences in more detail, sets of (meta)vinculin tension sensors containing one of the four available linker peptides F40 (1–6 pN), FL (3–5 pN), HP35 (6–8 pN), and HP35st (9–11 pN) were expressed in vinc$^{(-/-)}$ cells. Interestingly, the decrease in FRET efficiency of M-TS was consistently less pronounced across the whole force range of 1–11 pN. At the same time though, the FRET efficiency difference between V-TS and M-TS decreased with increasing stiffness of the linker peptide (Figure 15a). FRET efficiencies of individual days were highly reproducible and supported the reliability of the experimental results (Figure 15b). Together, these findings propose that the vinculin isoforms transduce forces differently.

There are two possible interpretations of the results above: either metavinculin is on average under lower force per molecule than vinculin; or a lower fraction of metavinculin molecules is mechanically engaged (see 1.3.2).

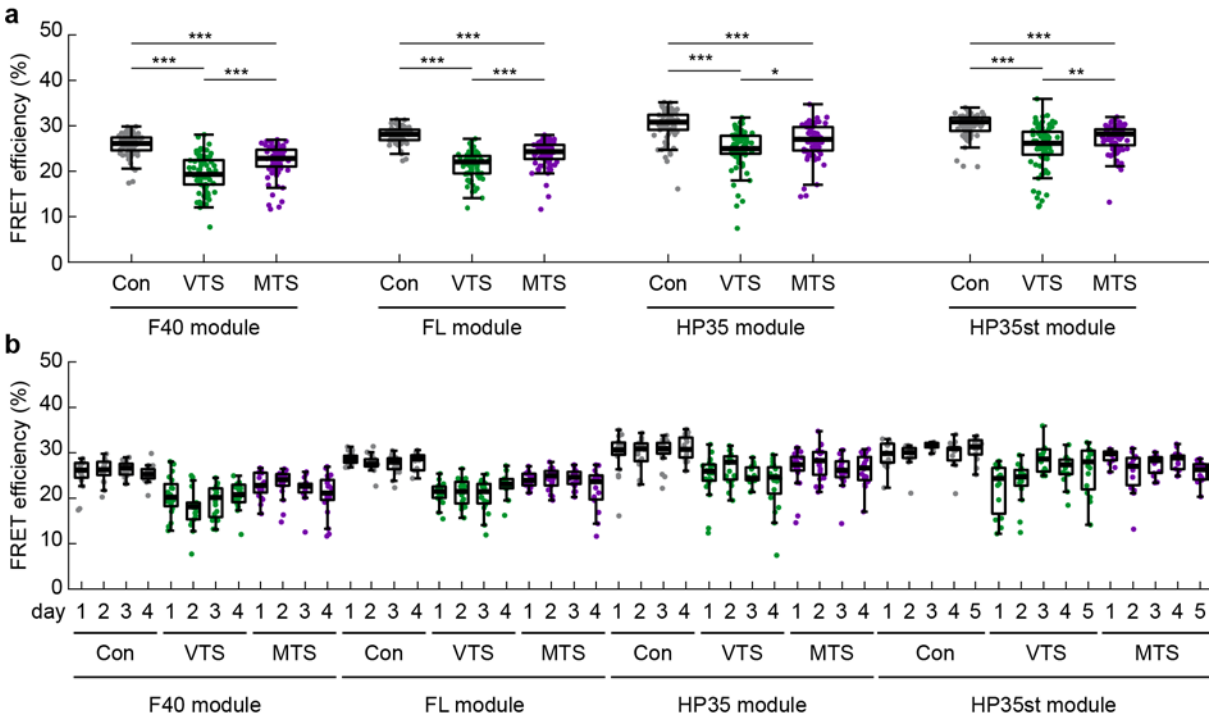

FIGURE 15: VINCULIN ISOFORM-SPECIFIC FRET DIFFERENCE IS CONSISTENT ACROSS 1–11 PN. (a) Live-cell FLIM measurements of vinc$^{(-/-)}$ cells expressing no-force control (Con-TS), vinculin (V-TS) and metavinculin (M-TS) tension sensors containing mechanosensitive linkers specific for distinct force ranges: F40 (1–6 pN), FL (3–5 pN), HP35 (6–8 pN), and HP35st (9–11 pN). Distinctly smaller FRET decrease of M-TS is consistent across 1–11 pN, but the isoform specific difference becomes smaller at higher force ranges; data of FL and HP35st modules are the same as in Figure 9b and c, respectively. (F40 n=74, 77, 80; FL n= 73, 73, 74; HP35 n=78, 80, 80; HP35st n=72, 77, 77). **(b)** Highly reproducible FRET efficiencies of individual experimental days sustain the reliability of the experimental results. Boxplots show median, 25th and 75th percentile with whiskers reaching to the last data point within 1.5× interquartile range. Kolmogorov–Smirnov test: ***p < 0.001, **p < 0.01, 571 *p < 0.05, n.s. (not significant) p ≥ 0.05. Modified figure reproduced from Kanoldt et al. 2020.

To distinguish between these two scenarios, the fraction of stretched molecules was determined by evaluating live cell FLIM measurements of all four (meta)vinculin tension sensor sets with a bi-exponential fitting algorithm (see 2.4.3). The approximated lifetimes τ_{noFRET} of 3.21 ns (F40), 3.06 ns (FL), 3.09 ns (HP35) and 3.03 ns (HP35st), measured with the same VY construct for each tension sensor set, differed slightly, therefore highlighting the importance of measuring the donor-only lifetime control with each data set, especially when sets measured several weeks or month apart are compared (Figure 16a). As expected, the estimated lifetimes τ_{FRET} of 1.68 ns (F40), 1.40 ns (FL), 1.30 ns (HP35) and 1.26 ns (HP35st) reflected the discrete starting FRET efficiencies of the TS modules caused by different size and fold of the linker peptides, which result in distinct orientations and distances of the fluorophore FRET pairs (Figure 16b). Interestingly, the resulting proportion of non FRETing tension sensor, which corresponds to the ratio of open tension sensors in Con-TS, is very similar for all TS modules (F40: 51.0%; FL: 52.9%; HP35: 52.0%; HP35st: 51.6%) and coincides with in vitro fluorescence

correlation spectroscopy (FCS) measurements of fluorescently inactive mCherry (56.9%; Figure 16c; Hendrix et al. 2008).

The mechanical engagement ratios of V-TS expressing cells ranged between 17% and 27% (F40: 27.6%; FL: 24.0%; HP35: 20.2; HP35st: 17.1%) and decreased with increasing linker stiffness, indicating that vinculin experiences a wide range of forces of at least 1–11 pN (Figure 16d). In contrast, the fraction of mechanically engaged molecules in M-TS-expressing cells was overall consistently lower (F40: 13.6%; FL: 14.9%; HP35: 14.6%; HP35st: 9.4%) and, intriguingly, remained constant at forces between 1–8 pN, only decreasing at higher forces (Figure 16e). In conclusion these data indicate that metavinculin molecules bear only mechanical tension >6–8 pN, while concomitantly a smaller fraction of the metavinculin linkages carries the mechanical load (Figure 16f).

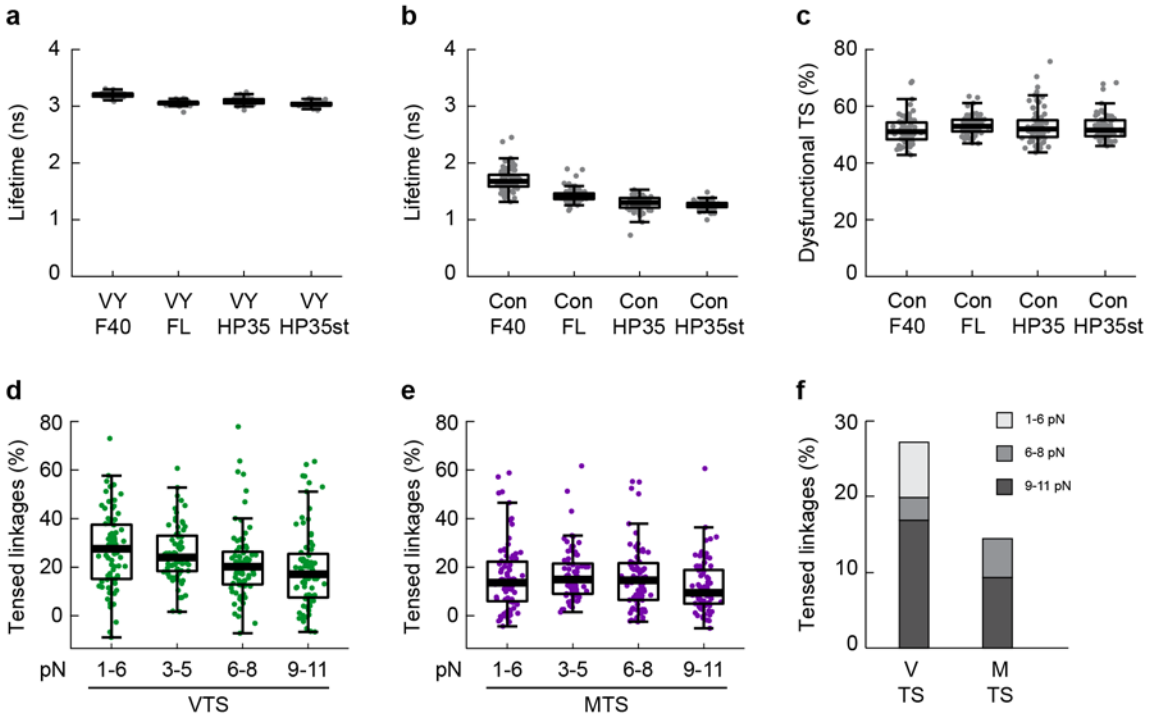

FIGURE 16: METAVINCULIN IS CHARACTERIZED BY HIGHER FORCE PER MOLECULE BUT LOWER ENGAGEMENT RATIOS. (a) Lifetimes of donor only (VY)-expressing cells merged by TS module used to approximate the lifetime of the open tension sensor τ_{noFRET} (n=72, 40, 58, 59). **(b)** Lifetimes of no-force control (Con-TS)-expressing cells used to approximate the lifetime of the closed tension sensor τ_{FRET} (n=74, 73, 72, 72). **(c)** Ratios of non FRETing no-force control tension sensors (Con-TS) due to fluorescently inactive mCherry used to rescale V-TS and M-TS engagement ratio data (n=72, 73, 79, 72). **(d)** Ratio of stretched tension sensors in V-TS expressing cells shows that 20–30% of the molecules are under tension and vinculin is exposed to a wide range of different forces (n=77, 73, 80, 76 cells). **(e)** Analogous investigation of M-TS expressing cells shows a smaller amount of mechanically engaged tension sensor molecules; note the equal amounts of tensed M-TS molecules using modules sensitive to 1–6 pN, 3–5 pN and 6–8 pN suggesting comparably high forces per molecule across metavinculin (n=80, 74, 79, 77 cells). **(f)** Comparing the relative amount of V-TS and M-TS molecules under specific forces reveals that metavinculin linkages are less frequently mechanically engaged and bear higher force per molecule. Boxplots show median, 25th and 75th percentile with whiskers reaching to the last data point within 1.5× interquartile range. Kolmogorov–Smirnov test: ***p < 0.001, **p < 0.01, 571 *p < 0.05, n.s. (not significant) p ≥ 0.05. Modified figure reproduced from Kanoldt et al. 2020.

3.1.4 Influence of differential force transduction of (meta)vinculin on talin tension

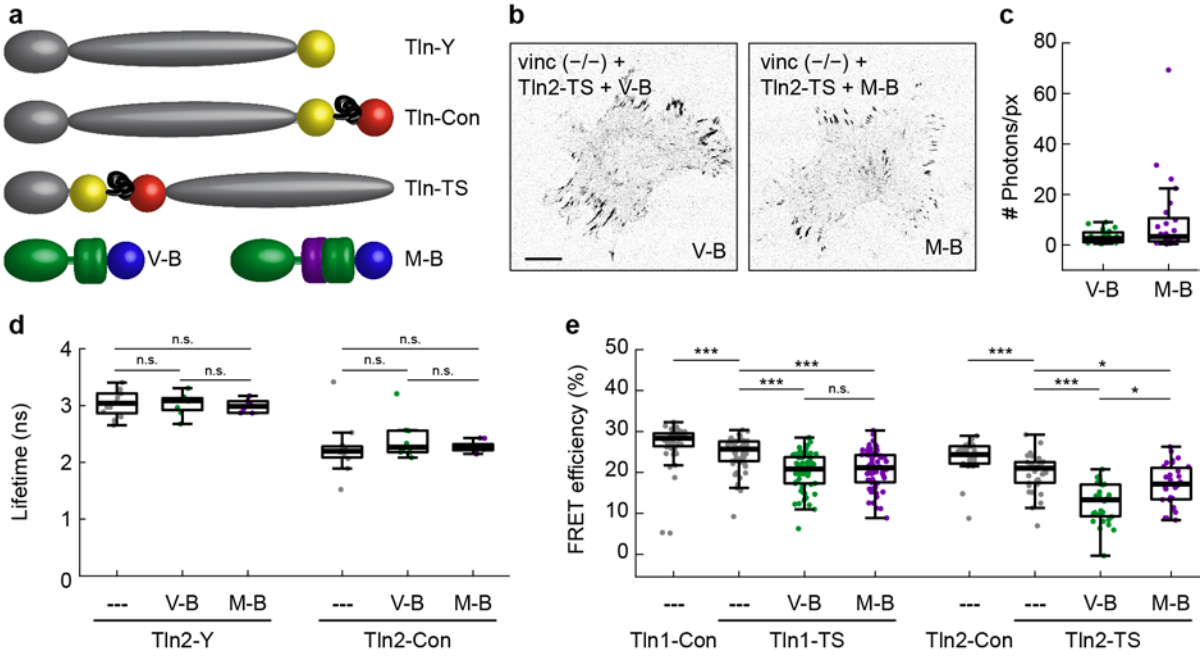

FIGURE 17: DIFFERENTIAL FORCE TRANSDUCTION OF VINCULIN SPLICE ISOFORMS ALTERS TENSION ON TALIN. **(a)** Schematic depiction of tension sensor constructs used for talin FRET-FLIM studies in dependence of the presence of (meta)vinculin: the donor only construct (Tln-Y) containing only the donor fluorophore at the C-terminus of talin; the no-force control tension sensor (Tln-Con) with the TS module placed at the C-terminus of talin; the talin tension sensor (Tln-TS) with the TS module placed in between the head and tail domain; vinculin (V-B) and metavinculin (M-B) C-terminally tagged with BFP. YPet donor fluorophore (yellow), mCherry acceptor fluorophore (red), talin (grey), vinculin (green), metavinculin insert (purple), mechanosensitive linker (black). **(b)** Representative images of vinc$^{(-/-)}$ cells expressing Tln2-TS together with V-B or M-B taken directly after FLIM measurements. The images depict the blue channel showing that V-B and M-B localize to FAs. Scale bar: 20 µm. **(c)** Normalized photon count per pixel of FA signal of images measured after each FLIM measurement are very similar for V-B and M-B (n= 21, 25). **(d)** The lifetimes of Tln2-Y and Tln2-Con are not influenced by co-expression of V-B or M-B (Tln1 n=13, 8, 6; Tln2 n= 11, 9, 9). **(e)** Live-cell FLIM measurements of vinc$^{(-/-)}$ cells expressing HP35-based Tln1-TS and Tln2-TS show that the presence of V-B and M-B greatly decrease FRET efficiencies on both isoforms. Note the smaller decrease caused by M-B on Tln2-TS. (Tln1 n= 52, 59, 67, 69; Tln2 n= 30, 36, 31, 31). Boxplots show median, 25th and 75th percentile with whiskers reaching to the last data point within 1.5× interquartile range. Kolmogorov–Smirnov test: ***p < 0.001, **p < 0.01, 571 *p < 0.05, n.s. (not significant) p ≥ 0.05. Modified figure reproduced from Kanoldt et al. 2020.

To investigate the influence of vinculin isoform-specific force transduction on force propagation across the integrin–talin linkage, talin-1 (Tln1-TS) and talin-2 (Tln2-TS) tension sensors containing the HP35 TS module (Austen et al. 2015) were co-expressed with BFP-tagged vinculin (V-B) or metavinculin (M-B) in vinc$^{(-/-)}$ cells (Figure 17a). Tln1-TS measurements were performed by Dr. Christiane Barz. V-B and M-B localized with similar intensity together with the talin tension sensors in FAs (Figure 17b and c). Co-expression of V-B and M-B did not influence the lifetime of the donor only construct (Tln2-Y) or the no-force control (Tln2-Con) of talin-2, thereby confirming that BFP fluorescence does not affect FRET between YPet and mCherry (Figure 17d). Consistent with previous experiments (Austen et al. 2015), the FRET efficiency reduction of Tln1-TS and Tln2-TS expressing cells was small in the absence of vinculin, whereas the co-expression of V-B increased force levels on both talin isoforms significantly

(Figure 17e). Interestingly, co-expression of M-B elevated force levels on talin-1 equally to V-B, but decreased FRET efficiencies less on talin-2. Of note, changes in FRET efficiencies were overall smaller for the cells expressing the Tln1-TS set, leading to a potential disguise of small differences. Together these data demonstrate that force transduction across integrin–talin linkages containing talin-2 is vinculin isoform-dependent.

To examine the different effects of (meta)vinculin on the talin isoforms in more detail, the molecular mechanical engagement ratios of Tln1-TS and Tln2-TS were compared. Therefore, the biexponential fits of the live cell FILM measurements were based on the merged donor lifetime Tln-Y of 3.12 ns (τ_{noFRET}, Figure 18a) and the two no-force control lifetimes Tln1-Con of 1.26 ns and Tln2-Con of 1.35 ns (τ_{FRET}, Figure 18b). Similarly to the corresponding (meta)vinculin tension sensor data (see 3.1.3), the fraction of non FRETing tension sensor of Tln1-Con (58.2%) and Tln2-Con (58.5%) was indistinguishable demonstrating equal amounts of fluorescently inactive mCherry (Figure 18c). The fraction of mechanically engaged Tln1-TS linkages was elevated nearly equally in the presence of the two vinculin splice isoforms (---: 9.4%; V-B: 27.4%; M-B: 26.4%), whereas the proportion of tensed Tln2-TS linkages was increased more strongly by co-expression of V-B than of M-B (---: 14.4%; V-B: 46.5%; M-B: 30.4%) (Figure 18d). These data reflect the previously observed FRET efficiency differences and indicate, that both vinculin and metavinculin increase the amount of talin linkages experiencing forces of at least 6–8 pN.

The mechanical engagement ratios of Tln1-TS in the presence and absence of vinculin are consistently lower than those of the Tln2-TS, implying that generally less Tln1 molecules transmit forces. However, when taking a closer look at the relative increase of stretched talin linkages upon co-expression of V-B and M-B in Figure 18d, the 2–3-fold increase in both isoforms is very similar. Even more striking is the consistent correlation of 0.6-fold–0.9-fold of the fraction of tensed linkages of the corresponding Tln1-TS and Tln2-TS data sets. Surprisingly, the comparison of the normalized FRET corrected photon count detected during the FLIM experiments shows the inverse correlation of 0.6-fold less photons for Tln2-TS than for Tln1-TS, whereas it is constant within each set (Figure 18e). Since each tension sensor molecule deterministically contains one YPet fluorophore, this number of photons can be used as an approximation of the amount of tension sensor molecules emitting the signal, and, consequently, allows the calculation of the relative number of engaged tension sensor molecules (see 2.4.3). Indeed, the relative amount of talin molecules transmitting tension is the same in the absence of vinculin and very similar its presence, while the co-expression of M-B leads to different amounts of mechanically engaged Tln1-TS and Tln2-TS molecules (---: 1.2, 1.2; V-B: 3.4, 3.1; M-B: 3.5, 2.4; Figure 18f).

In summary, these data suggest that the same number of talin-1 and -2 tension sensor molecules is transmitting forces of at least 6–8 pN in the presence and absence of vinculin, even though more talin-1 molecules would be available. Nevertheless, the difference of mechanically engaged molecules upon metavinculin expression between Tln1-TS and Tln2-TS remains, indicating that metavinculin might have a talin isoform-specific effect on integrin–talin linkages.

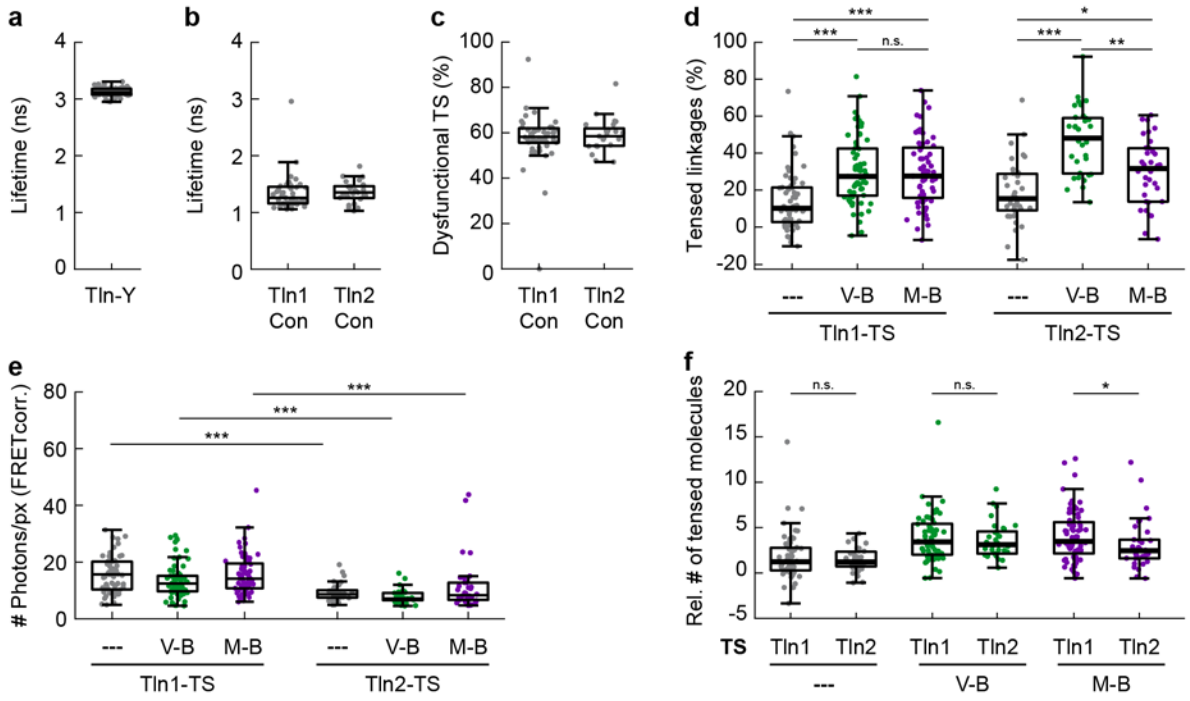

FIGURE 18: THE SAME NUMBER OF TALIN-1 AND -2 MOLECULES TRANSMITS TENSION IN FAS. (a) Lifetimes of donor only (Tln-Y)-expressing cells merged over both talin isoforms used to approximate the lifetime of the open talin tension sensor τ_{noFRET} (n= 70). **(b)** Lifetimes of no-force control of Tln1 (Tln1-Con) and Tln2 (Tln2-Con)-expressing cells used to approximate the lifetimes of the respective closed tension sensors τ_{FRET}. **(c)** Ratios of non FRETing Tln1-Con and Tln2-Con due to fluorescently inactive mCherry used to rescale the engagement ratio data of the respective tension sensor set (b and c: n= 47, 25). **(d)** Co-expression of V-B and M-B elevates the ratio of stretched talin tension sensors experiencing forces of at least 6–8 pN. Note the distinct vinculin splice-variant dependent difference in engaged talin-2 linkages. **(e)** Number of photons normalized to the analyzed number of pixels and corrected for photon loss due to FRET of FLIM-FRET data of Tln2-TS experiments is consistently smaller than of Tln1-TS. **(f)** The normalized relative number of tensed Tln1-TS and Tln2-TS molecules per pixel is very similar in the presence and absence of V-B. Note the talin isoform-specific difference caused by M-B expression. (d–f: Tln1 n=59, 69, 69; Tln2 n= 35, 33, 34). Boxplots show median, 25th and 75th percentile with whiskers reaching to the last data point within 1.5× interquartile range. Kolmogorov–Smirnov test: ***p < 0.001, **p < 0.01, 571 *p < 0.05, n.s. (not significant) p ≥ 0.05.

3.1.5 Influence of activation on force transduction of (meta)vinculin

Metavinculin was shown to display a higher affinity to talin as compared to vinculin, which was attributed to an increased activation of metavinculin (see 1.2.2). Yet, the experiments presented in the previous chapter (see 3.1.3) indicate that co-expression of metavinculin leads to a smaller increase in tensed talin molecules compared to vinculin. To investigate this apparent inconsistency, the influence of activation on (meta)vinculin force engagement was tested in FLIM-FRET experiments of $vinc^{(-/-)}$ cells expressing FL- and F40-based (meta)vinculin tension sensors comprising two types of previously published point mutations with opposite effect on the autoinhibition of the two splice isoforms (see 1.2.2).

The A50I mutation, located in the head domain of (meta)vinculin, was shown to reduce the head to tail dissociation of vinculin and, contemporarily, its binding to talin (Figure 19a). Introduction of this deactivating mutation into both F40- and FL-based V-TS (V-TS-A50I) and M-TS (M-TS-A50I) slightly reduced the fluorescent signal intensity of the tension sensors in FAs accompanied by a visible increase in cytosolic signal as well as a reduction of central FAs, as was observed previously (Figure 19b; Carisey et al. 2013). Unexpectedly, both V-TS-A50I and M-TS-A50I displayed decreased FRET efficiencies as compared to V-TS and M-TS (Figure 20a and b). Therefore, these data indicate that reducing (meta)vinculin activation leads to an increased amount of both vinculin and metavinculin molecules under tension of at least 1–6 pN.

Combined mutation of the charged aa N773 and E775 (HTI) to alanine in the head domain of (meta)vinculin was shown to reduce the autoinhibitory affinity of the head to tail interaction of vinculin (Figure 19a). Introduction of these two activating mutations into the V-TS (V-TS-HTI) induced bright prominent aggregates accompanied by a strongly reduced fluorescent signal of the tension sensor in FAs and a small increase in cytosolic signal, suggesting that overly activated vinculin is either prone to aggregation or compensated by its reduction in FAs (Figure 19b). These effects were observed only to a very small extent in cells expressing HTI-mutated M-TS (M-TS-HTI). In contrast to V-TS-HTI expressing cells, M-TS-HTI expressing cells displayed a clearly visible FA signal and small aggregates were detected only occasionally. Of note, the cell size of both V-TS-HTI and M-TS-HTI seemed smaller when compared to V-TS and M-TS. Interestingly, the FL-based M-TS-HTI expressing cells displayed reduced FRET efficiencies similar to no-force control levels, whereas the F40-based metavinculin FRET efficiency remained unchanged upon HTI mutation (Figure 20c and d). Thus, in accordance with the A50I mutation experiments, activation of metavinculin seems to reduce the relative number of molecules experiencing force >3–5 pN.

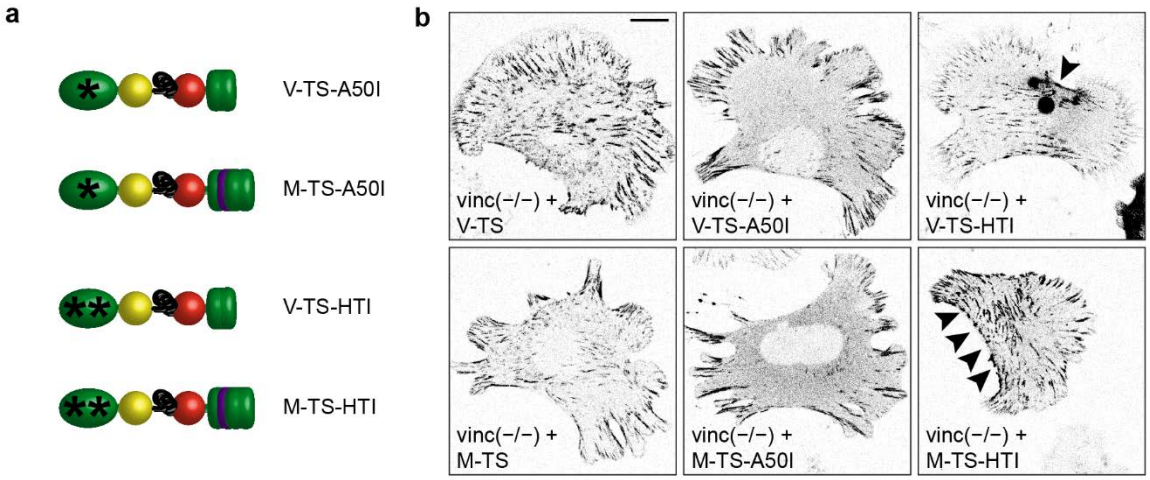

FIGURE 19: A50I AND HTI MUTATIONS ALTER THE ACTIVATION OF (META)VINCULIN. (a) Schematic depiction of tension sensor constructs used for FRET-FLIM studies of (meta)vinculin containing mutations altering the activation of the splice isoforms: the vinculin (V-TS-A50I) and metavinculin (M-TS-A50I) tension sensors containing an A50I point mutation (*) in the head domain of (meta)vinculin leading to decreased affinity for talin due to reduced activation; the vinculin (V-TS-HTI) and metavinculin (M-TS-HTI) tension sensors containing the two point mutations N773A and E775A (**) in the head domain of (meta)vinculin leading to reduced head to tail interaction (HTI). YPet donor fluorophore (yellow), mCherry acceptor fluorophore (red), vinculin (green), metavinculin insert (purple), mechanosensitive linker (black). **(b)** Representative fluorescent images of vinc$^{(-/-)}$ cells expressing FL-based mutated (meta)vinculin tension sensors: V-TS-A50I and M-TS-A50I expressing cells show an increased cytoplasmic fluorescent signal and reduced number of internal FAs; V-TS-HTI expressing cells display bright aggregates (arrow heads) accompanied by reduced YPet signal intensity in FAs, while the aggregation phenotype is less pronounced in M-TS-HTI expressing cells. Grey scale images depict summed photons acquired during a FLIM measurement depicted in Figure 16b and d. Scale bar: 20 µm. Modified figure reproduced from Kanoldt et al. 2020.

The aggregation phenotype displayed by V-TS-HTI expressing cells complicated FRET-FLIM analysis and interpretation. While the aggregates were excluded from fluorescence lifetime analysis, the reduced fluorescent signal intensity in the FAs caused increased spreading of the FRET data points due to less precise fitting of the photon lifetime decay amongst others (see 1.3.2). Nonetheless, median FRET efficiency of V-TS-HTI based on the F40 linker was reduced significantly when compared to V-TS, whereas HTI mutation of the FL-based V-TS did not apparently alter FRET efficiency. Together, these data suggest, that activation of vinculin leads to a reduced number of molecules in the FAs, while interpretation of tension is difficult due to the aggregation phenotype.

Taken together, these experiments suggest that activation of (meta)vinculin changes the force distribution and magnitude experienced by the molecules of the two splice isoforms. Counterintuitively, the correlation of activation and load-bearing engagement seems to be indirect, i.e. an increased (or decreased) activation leads to decreased (or increased) force levels on (meta)vinculin. However, more experiments are required to better understand the presented correlations.

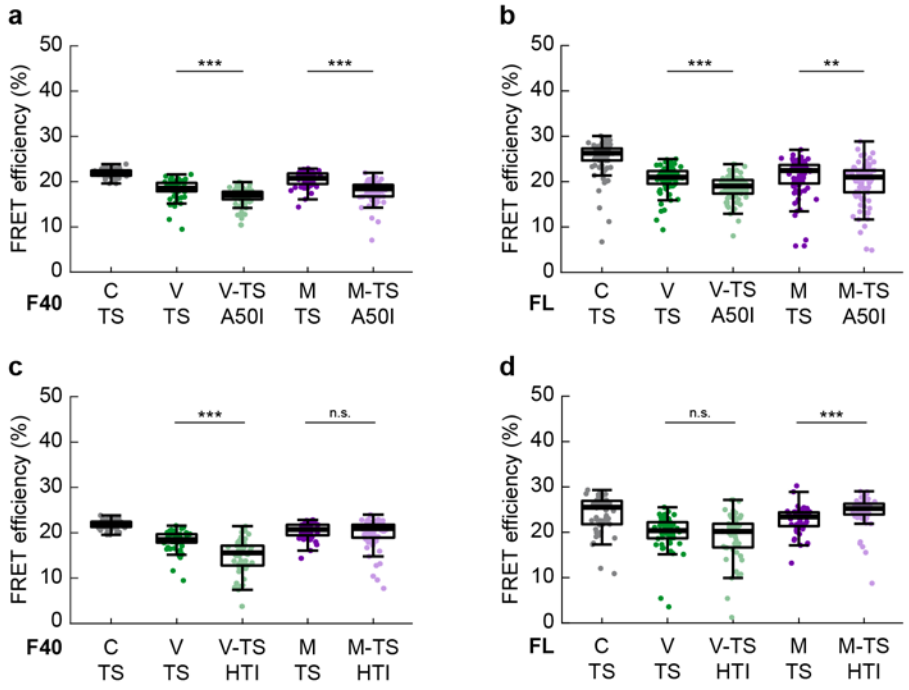

FIGURE 20: ACTIVATION MUTATIONS ALTER FORCE DISTRIBUTION ON (META)VINCULIN. Live-cell FLIM measurements of vinc$^{(-/-)}$ cells expressing **(a)** F40-based or **(b)** FL-based vinculin (V-TS-A50I) or metavinculin (M-TS-A50I) tension sensors containing the deactivating point mutation A50I show a decrease in FRET efficiencies upon mutation in vinculin and metavinculin samples (a: n = 60, 59, 77, 57, 78 cells; b: n = 84, 83, 78, 85, 86 cells). **(c)** Live-cell FLIM measurements of vinc$^{(-/-)}$ cells expressing the F40-based vinculin (V-TS-HTI) and metavinculin (M-TS-HTI) tension sensors including the activating point mutations N773A and E775A demonstrate that reduced HTI leads to a FRET efficiency decrease for vinculin but not metavinculin (n = 60, 59, 52, 57, 80 cells); data of Con-TS, V-TS and M-TS are the same as in (b). **(d)** Reduced HTI in analogous experiments with the FL-based tension sensor set causes a decrease in metavinculin FRET efficiency upon mutation, whereas no change in the vinculin sample is observed. Note the increased spread in both V-TS-HTI samples. (n = 53, 56, 50, 51, 51 cells). Boxplots show median, 25th and 75th percentile with whiskers reaching to the last data point within 1.5× interquartile range. Kolmogorov–Smirnov test: ***p < 0.001, **p < 0.01, 571 *p < 0.05, n.s. (not significant) p ≥ 0.05. Modified figure reproduced from Kanoldt et al. 2020.

3.2 THE ROLE OF METAVINCULIN IN MICE

3.2.1 Unaltered tissue architecture in metavinculin-deficient mice

Metavinculin is widely considered a cardiomyopathy gene, because absence and mutation of this vinculin splice isoform were detected in cardiomyopathy patients (see 1.2.1). To date, this association could not be proved due to only a considerably small number of identified patients and missing family linkage analyses. Therefore, the importance of metavinculin for heart muscle function was investigated in the metavinculin knockout mouse model $M^{(-/-)}$ generated by Dr. Anna Chrostek-Grashoff. Excision of the exon encoding for the metavinculin insert located between exon 18 and 19 in the $M^{(-/-)}$ mouse line was confirmed by genotyping PCR (Figure 21a). $M^{(-/-)}$ mice did not show an overt phenotype as they were viable, fertile and born at the expected Mendelian ratios (Figure 21b). In accordance with previous studies (see 1.2.1), metavinculin expression was low in cardiac muscle tissue, moderate in skeletal muscle of the gastrocnemius (GA) and high in the smooth muscle of the uterus when compared to vinculin (Figure 21c). Accordingly, heterozygous mice showed reduced levels of metavinculin and the splice isoform was absent in the muscle tissues of knockout mice as well as in the control non-muscle tissue of the liver.

Expression levels of costamere proteins β1 integrin, representative for the integrin–vinculin–talin complex, and dystrophin, representative for the dystrophin–glycoprotein complex, were not altered in 6- and 13-months-old knockout animals (Figure 21d). Also, adherens junction markers α-catenin, β-catenin and N-cadherin as well as gap junction marker connexin-43 did not display changes in expression levels upon metavinculin knockout. Histological sections of the heart muscle tissue revealed an intact tissue architecture (Figure 21e). Immunostainings of the myocardium revealed normal localization of costamere, ICD and gap junction proteins in 13-months-old $M^{(-/-)}$ mice (Figure 22). In summary, loss of metavinculin does not seem to impair development of mice or to deteriorate tissue homeostasis of the examined muscle tissue.

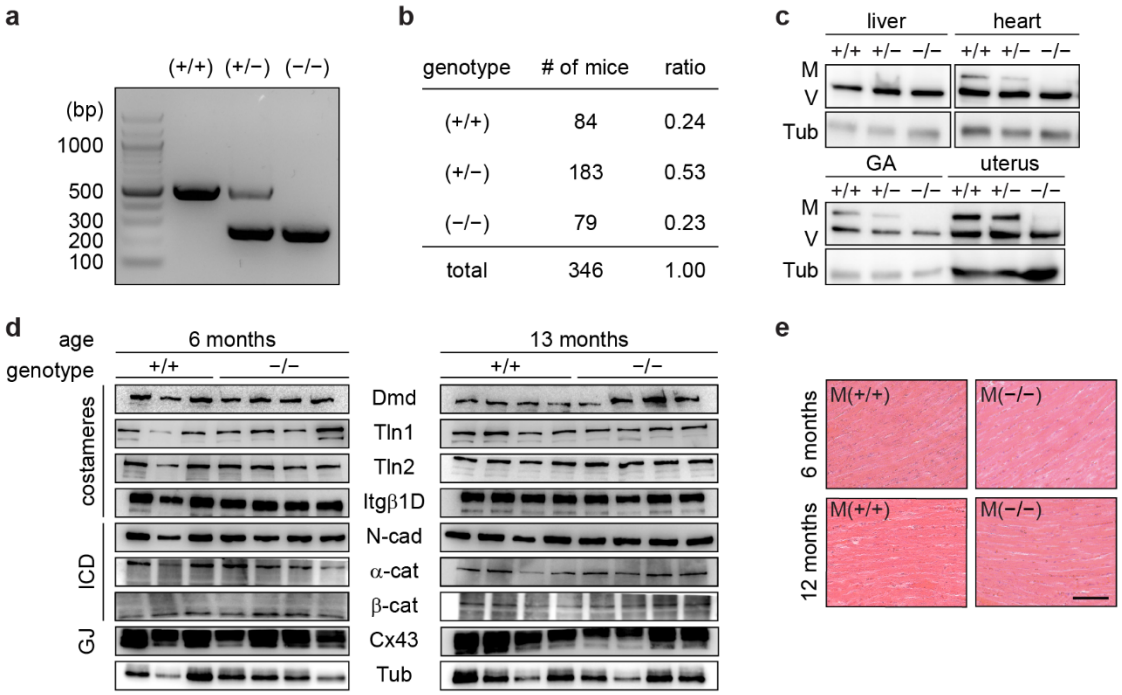

FIGURE 21: PROTEIN EXPRESSION AND TISSUE MORPHOLOGY IS UNALATERED IN METAVINCULIN-DEFICIENT MICE (a) Representative results of genotyping PCR performed on wild type (+/+), heterozygous (+/−), and knockout (−/−) samples generating a bigger fragment (504 bp) on the wild type allele than on the knock-out allele (245 bp). **(b)** Heterozygous mice breed at Mendelian ratio (X^2=1.019; p=0.60; $X^2_{0.05}$=5.991). **(c)** Metavinculin expression in muscle tissues is reduced in heterozygous $M^{(+/-)}$ mice and absent in knockout $M^{(-/-)}$ mice as compared to wild type $M^{(+/+)}$ littermates. (GA: gastrocnemius muscle; V: vinculin; M: metavinculin; loading control Tub: tubulin). **(d)** Western blot analysis of costamere proteins (Dmd: dystrophin; Tln1: talin-1; Tln2: talin-2; Itgβ1D: integrin β1 D), intercalated disc (ICD) proteins (N-cad: N-cadherin; α-cat: α-catenin; β-cat: β-catenin), and gap junction (GJ) protein connexin-43 (Cx43) in ventricular tissue of 6- and 13-months-old $M^{(-/-)}$ mice reveals largely unaltered expression levels (loading control tub: tubulin). **(e)** Histological analysis of heart tissue sections of 6- and 13-months-old $M^{(-/-)}$ mice confirms normal tissue morphology. Scale bar: 40 µm. Modified figure reproduced from Kanoldt et al. 2020.

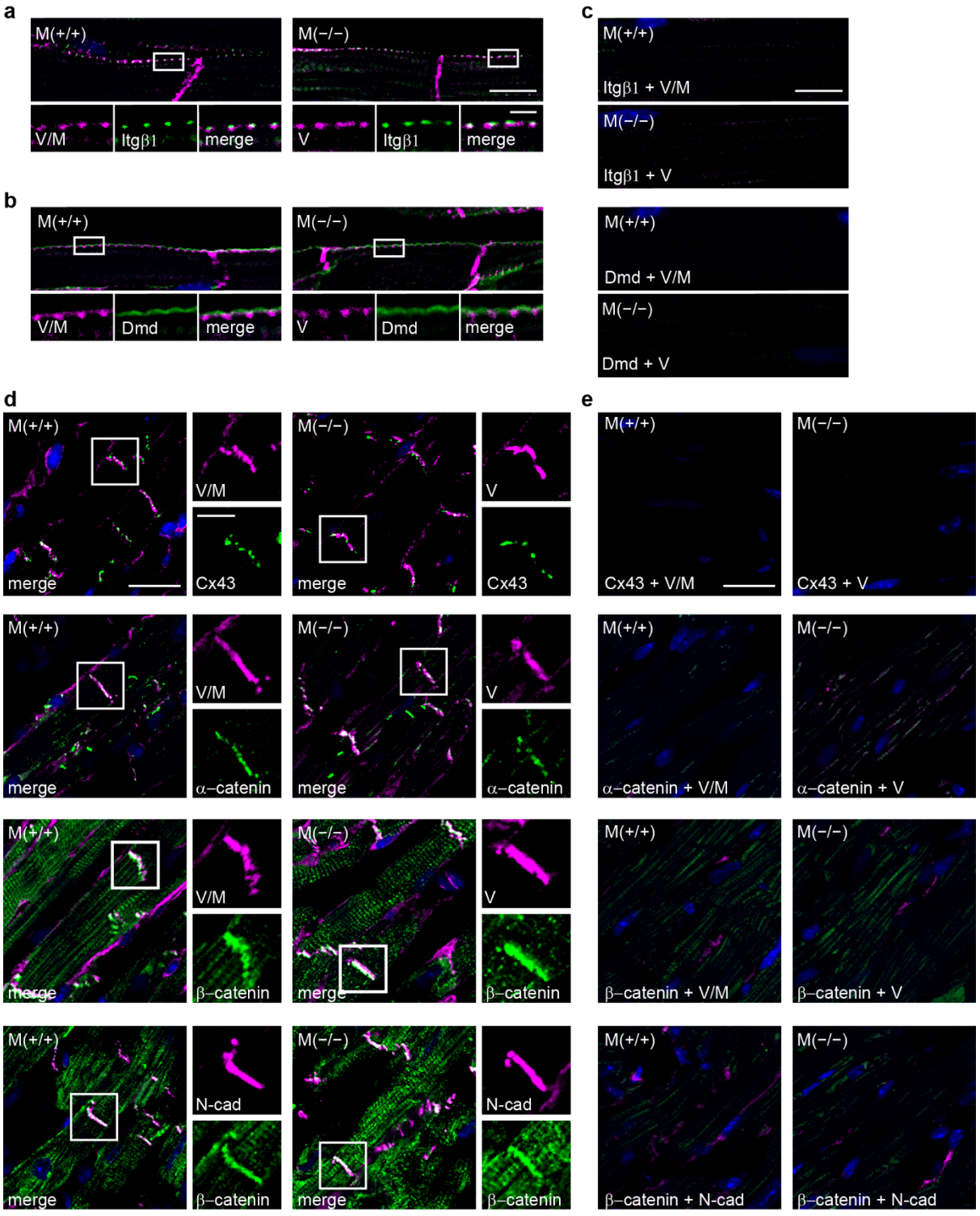

FIGURE 22: TISSUE ARCHITECTURE IS NORMAL IN THE ABSENCE OF METAVINCULIN. Costamere, ICD and gap junction marker localize normally independent of metavinculin deficiency in the myocardium of 13-months-old wild type $M^{(+/+)}$ and knockout $M^{(-/-)}$ mice. No difference in tissue architecture is evident. Representative immunofluorescence stainings showing costamere marker **(a)** β1 integrin (Itg β1) and **(b)** dystrophin (Dmd). **(c)** Secondary antibody only control staining confirms specificity of signal observed in a and b. **(d)** Representative immunofluorescence images of adherens junction markers α-catenin (α-cat), β-catenin (β-cat), N-cadherin (N-cad), and gap junction marker connexin-43 (Cx43). **(e)** Secondary antibody only control staining confirms specificity of signal observed in d. Color coding as indicated in the images and DAPI staining in blue. Scale bar: 20 µm, in zoom: 10 µm. Modified figure reproduced from Kanoldt et al. 2020.

3.2.2 Normal hypertrophic response in metavinculin-deficient mice

To test the relevance of metavinculin under pathological conditions, $M^{(-/-)}$ mice were subdued to a TAC protocol mimicking pressure overload-induced cardiac hypertrophy in collaboration with the group of Prof. Dr. Dr. Stefan Engelhardt from the Institute of Pharmacology and Toxicology at the Technical University of Munich (see 2.5.2). As expected, heart size and ventricle weight of TAC-operated wild-type mice increased four weeks after surgery as compared to their sham-operated littermates (Figure 23a and b). Similarly, cardiac function assessed by echocardiography decreased significantly upon TAC operation, whereas sham-operated mice showed unaltered cardiac function parameters (Figure 23c and Table 33). Further histological analysis assessing interstitial fibrosis in the myocardium demonstrated clearly increased tissue fibrosis (Figure 23d and e) accompanied by distinctly elevated transcription levels of hypertrophy and fibrosis marker genes evaluated by qRT-PCR (Figure 23f). Together, these data confirm the successful performance of the TAC experiment.

Interestingly, the hypertrophic response of $M^{(-/-)}$ mice upon TAC was indistinguishable from wild-type littermates. TAC-induced increase in heart size and weight, as well as aggravation of cardiac function and interstitial fibrosis was equally pronounced in $M^{(-/-)}$ and $M^{(+/+)}$ mice (Figure 23a–d and Table 33). Of note, qRT-PCR analysis indicated a slightly less pronounced hypertrophy and fibrosis response in $M^{(-/-)}$ mice upon TAC compared to wild-type littermates, however, this observation was only significant for 2 out of 8 tested gene markers (Figure 23f). Moreover, the structure of costameres, ICDs and gap junctions, visualized by the localization of corresponding marker proteins, was equivalent between knockout and wild-type animals (Figure 24). Furthermore, expression levels of vinculin were not altered by metavinculin-deficiency in the hearts of TAC-operated knockout animals (Figure 25a), even though putative small compensatory changes might not be detectable due to comparably low expression of metavinculin in heart tissue.

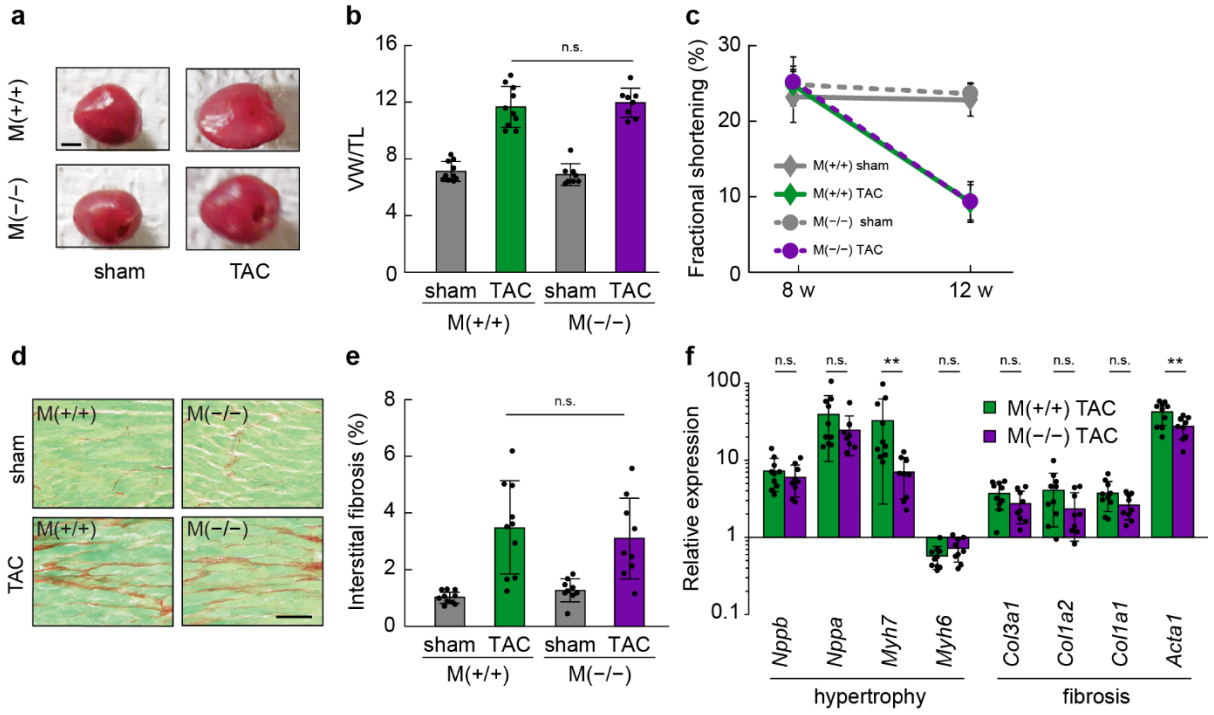

FIGURE 23: TRANSVERSE AORTIC CONSTRICTION (TAC) INDUCES NORMAL HYPERTROPHY RESPONSE IN $M^{(-/-)}$ MICE. (a) Representative images of ventricles of 3-months-old metavinculin knock-out $M^{(-/-)}$ and wild-type $M^{(+/+)}$ mice isolated 4 weeks after TAC demonstrate increased ventricle size in TAC operated mice. Scale bar: 0.2 cm. **(b)** Analysis of ventricle weight (VW) normalized to tibia length (TL) shows an increase upon TAC, but no difference between wild-type and knockout animals (n=10, 10, 9, 9). **(c)** Representative parameter of echocardiographic analysis shows reduced heart function in TAC-operated mice, which is very similar between wild-type and knock-out animals (n=19, 9, 9, 7). Representative images of Sirius Red/Fast Green histological stainings of the myocardium **(d)** and quantification of interstitial fibrosis **(e)** demonstrate increased tissue fibrosis in TAC-operated mice, but no metavinculin-deficiency specific difference. Scale bar: 40 µm. **(f)** qRT-PCR analysis of cardiac remodeling markers in ventricular tissue of $M^{(-/-)}$ and $M^{(+/+)}$ mice demonstrate cardiac remodeling upon TAC and suggests a small, but mostly not significant, genotype-specific difference. Natriuretic peptide B precursor (*Nppb*), Natriuretic peptide A precursor (*Nppa*), myosin heavy chain 7 (*Myh7*), myosin heavy chain 6 (*Myh6*), collagen type III alpha 1 chain (*Col3a1*), collagen type I alpha 2 chain (*Col1a2*), collagen type I alpha 1 chain (*Col1a1*), actin alpha 1 (*Acta1*). (n=10,9). ANOVA followed by Sidak's test: $^{**}p < 0.01$, n.s. (not significant) $p \geq 0.05$. Modified figure reproduced from Kanoldt et al. 2020.

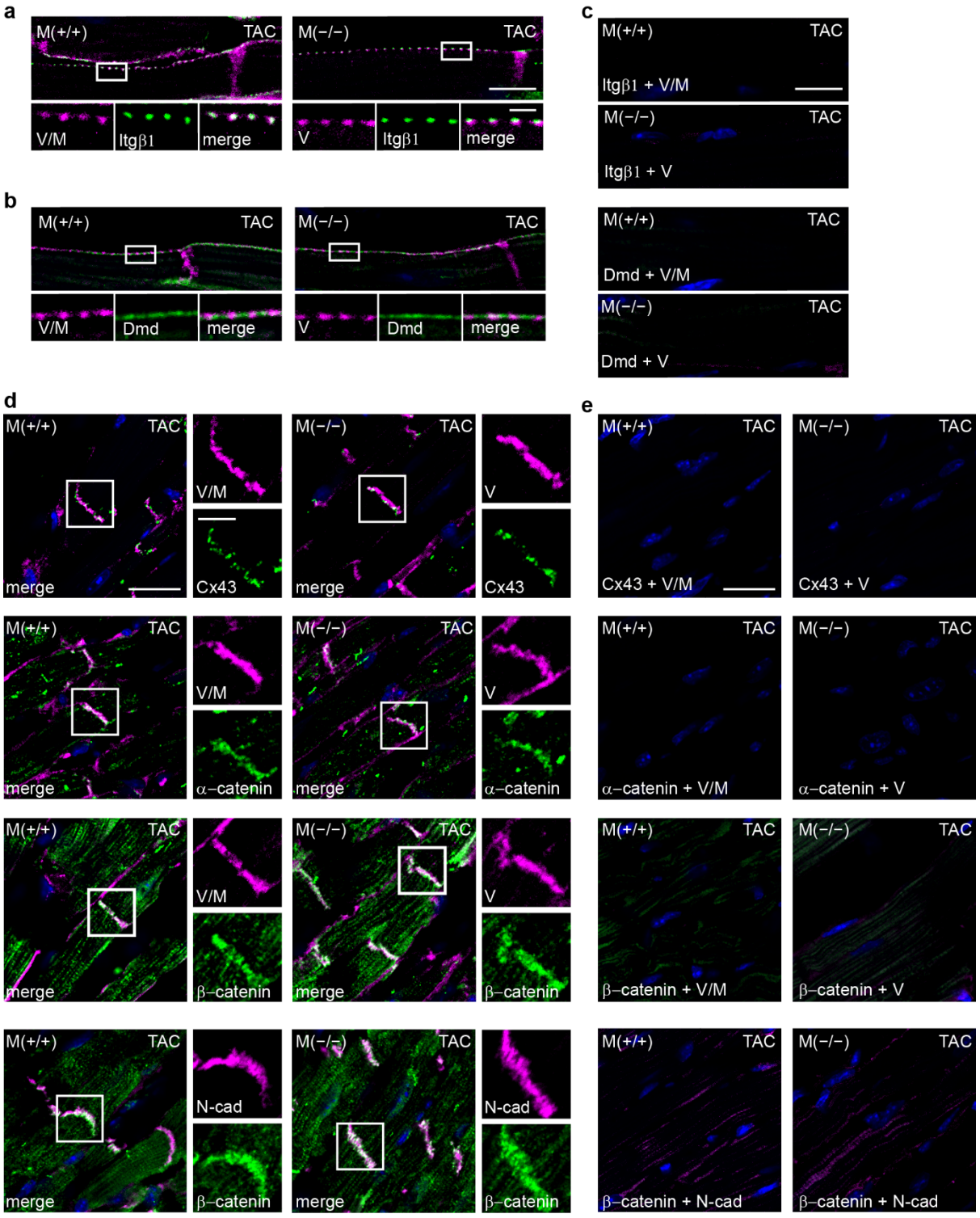

FIGURE 24: CARDIAC REMODELING UPON TAC IS NOT AGGRAVATED BY METAVINCULIN DEFICIENCY. No apparent difference in localization of costamere, ICD and gap junction marker as well as tissue architecture upon TAC in ventricular tissue of 3-months-old wild-type $M^{(+/+)}$ and knockout $M^{(-/-)}$ mice was detected. Representative immunofluorescence stainings show costamere markers **(a)** β1 integrin (Itg β1) and **(b)** dystrophin (Dmd). **(c)** Secondary antibody only control staining confirms specificity of signal observed in a and b. **(d)** Representative immunofluorescence images of adherens junction markers α-catenin (α-cat), β-catenin (β-cat), N-cadherin (N-cad), and gap junction marker connexin-43 (Cx43). **(e)** Secondary antibody only control staining confirms specificity of signal observed in d. Color coding as indicated in the images and DAPI staining in blue. Scale bar: 20 µm, in zoom: 10 µm. Modified figure reproduced from Kanoldt et al. 2020.

TABLE 33: ECHOCARDIOGRAPHIC ANALYSIS OF M$^{(-/-)}$ MICE BEFORE AND FOUR WEEKS AFTER TAC SURGERY.

	before surgery				after surgery			
Treatment	sham	sham	TAC	TAC	sham	sham	TAC	TAC
genotype	M(+/+)	M(−/−)	M(+/+)	M(−/−)	M(+/+)	M(−/−)	M(+/+)	M(−/−)
number	10	9	9	7	10	9	9	7
HR [BPM]	436.92 ± 57.90	471.38 ± 49.20	469.76 ± 52.35	432.35 ± 53.77	435.86 ± 90.87	420.66 ± 59.55	427.59 ± 86.55	465.26 ± 45.99
SV [µl]	27.38 ± 4.89	26.21 ± 7.69	26.29 ± 3.15	27.25 ± 3.74	27.97 ± 5.80	29.25 ± 7.72	15.79 ± 4.14 ***	14.88 ± 3.26 ***
EF [%]	47.14 ± 5.83	50.26 ± 3.39	50.02 ± 4.38	50.72 ± 5.39	46.54 ± 3.89	48.02 ± 2.45	20.54 ± 4.88 ***	20.66 ± 5.89 ***
FS [%]	23.19 ± 3.34	24.90 ± 2.00	24.80 ± 2.52	25.27 ± 3.20	22.81 ± 2.14	23.68 ± 1.33	9.24 ± 2.34 ***	9.29 ± 2.74 ***
CO [ml/min]	12.15 ± 3.57	12.31 ± 4.10	12.31 ± 1.78	11.72 ± 1.70	11.75 ± 1.95	11.76 ± 2.09	6.65 ± 2.02 ***	6.94 ± 1.71 **

Comparison of heart rate (HR), stroke volume (SV), ejection fraction (EF), fractional shortening (FS), cardiac output (CO) of wild type M$^{(+/+)}$ and metavinculin knockout M$^{(-/-)}$ mice before and four weeks after sham or transverse aortic constriction (TAC) surgery. TAC surgery did not reveal significant differences in cardiac function between M$^{(-/-)}$ and M$^{(+/+)}$ mice. All P-values were calculated by two-way ANOVA followed by Sidak's multiple comparison test and depicted p values compare data before and after surgery: *** P < 0.001, ** P < 0.01, * P < 0.05. Data represent means ± standard deviation. Modified figure reproduced from Kanoldt et al. 2020.

In conclusion, metavinculin-deficiency does not seem to cause an aberrant hypertrophy response in mice under the here tested conditions. Considering the challenging reproducibility of metavinculin signal detection in Western blots, notably, neither vinculin nor metavinculin expression levels seemed to be affected by TAC surgery (Figure 25b) calling into question the involvement of metavinculin in TAC-induced cardiac hypertrophy. Nevertheless, these data do not exclude a more pivotal role of metavinculin in other cardiac stress models.

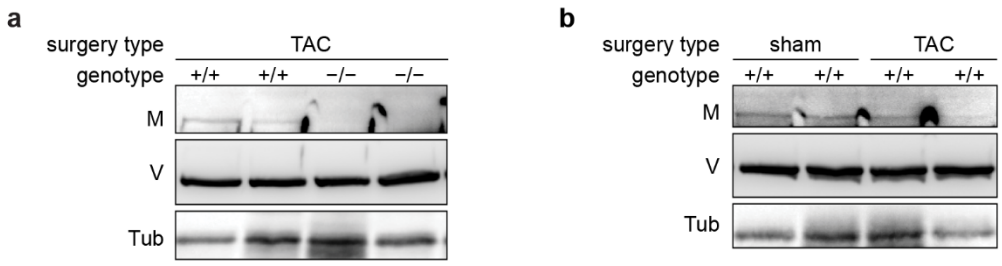

FIGURE 25: EXPRESSION LEVELS OF (META)VINCULIN ARE NOT ALTERED UPON TAC. (a) Vinculin expression in hearts of TAC-operated of 3-months-old wild-type M$^{(+/+)}$ and knockout M$^{(-/-)}$ mice seems to be independent of metavinculin-deficiency. **(b)** TAC induced cardiac stress does not seem to alter (meta)vinculin expression in heart tissue of wild type littermates. V: vinculin; M: metavinculin; loading control Tub: tubulin.

3.2.3 Reduced protein levels of mutated metavinculin in transgenic mice

To investigate the effect of the point mutation R975W, presumably causing cardiomyopathy, on heart integrity (see 1.2.1), the transgenic mouse model $M^{(R975W)}$ generated by Dr. Anna Chrostek-Grashoff was examined. Correct mutation of arginine to tryptophan in $M^{(R975W)}$ was ensured by sequencing and genotyping involving detection of FRT- and loxP-sites (Figure 26a and b). Like $M^{(-/-)}$ animals, $M^{(R975W)}$ mice were born at the expected Mendelian ratios and were viable and fertile (Figure 26c). Immunostainings of the myocardium of 13-months-old $M^{(R975W)}$ mice demonstrated normal tissue integrity and indistinguishable localization of costamere, ICD and gap junction proteins in wild-type and transgenic mice (Figure 27).

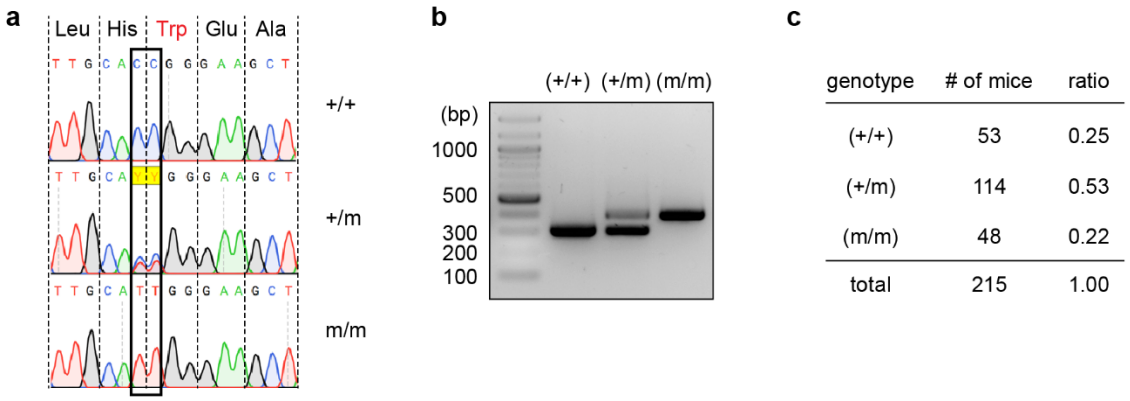

FIGURE 26: CONFIRMING MUTATION IN $M^{(R975W)}$ MICE. (a) Representative sequencing results of wild type (+/+), heterozygous (+/m) and mutated (m/m) $M^{(R975W)}$ mouse DNA confirming mutation of arginine to tryptophan at position 975. **(b)** Representative results of two-primer genotyping PCR generating a bigger fragment (400 bp) on the transgenic allele than on the wild type allele (312 bp). **(c)** Heterozygous $M^{(R975W)}$ mice breed at Mendelian ratio ($X^2 = 1.301$; $p = 0.52$; $X^2_{0.05} = 5.991$).

Interestingly, Western blot analysis revealed distinctly reduced protein levels of mutated metavinculin (M-R975W) to up to 30% of the wild-type levels in the uterus (Figure 28a and b). Talin-1 expression was not affected by mutation of metavinculin, however, vinculin levels were slightly, although not significantly, increased by 20% as compared to wild-type. Western blot analysis of metavinculin in heart tissue proved to be challenging, since the molecular weight of vinculin and metavinculin differs by only 7 kDa and the expression level of metavinculin compared to vinculin is particularly low. Therefore, reduced expression levels of M-R975W in the heart were observed but could not be reliably reproduced due to technical issues (Figure 28a and c). Meanwhile, talin-1 expression levels seemed independent of metavinculin mutation, whereas vinculin expression appeared slightly but not significantly increased by 9%. Together these results imply, that M-R975W protein levels are down-regulated in muscle tissue presumably to protect muscle integrity, and advocate for further analysis of the heterozygous and homozygous $M^{(R975W)}$ mouse line.

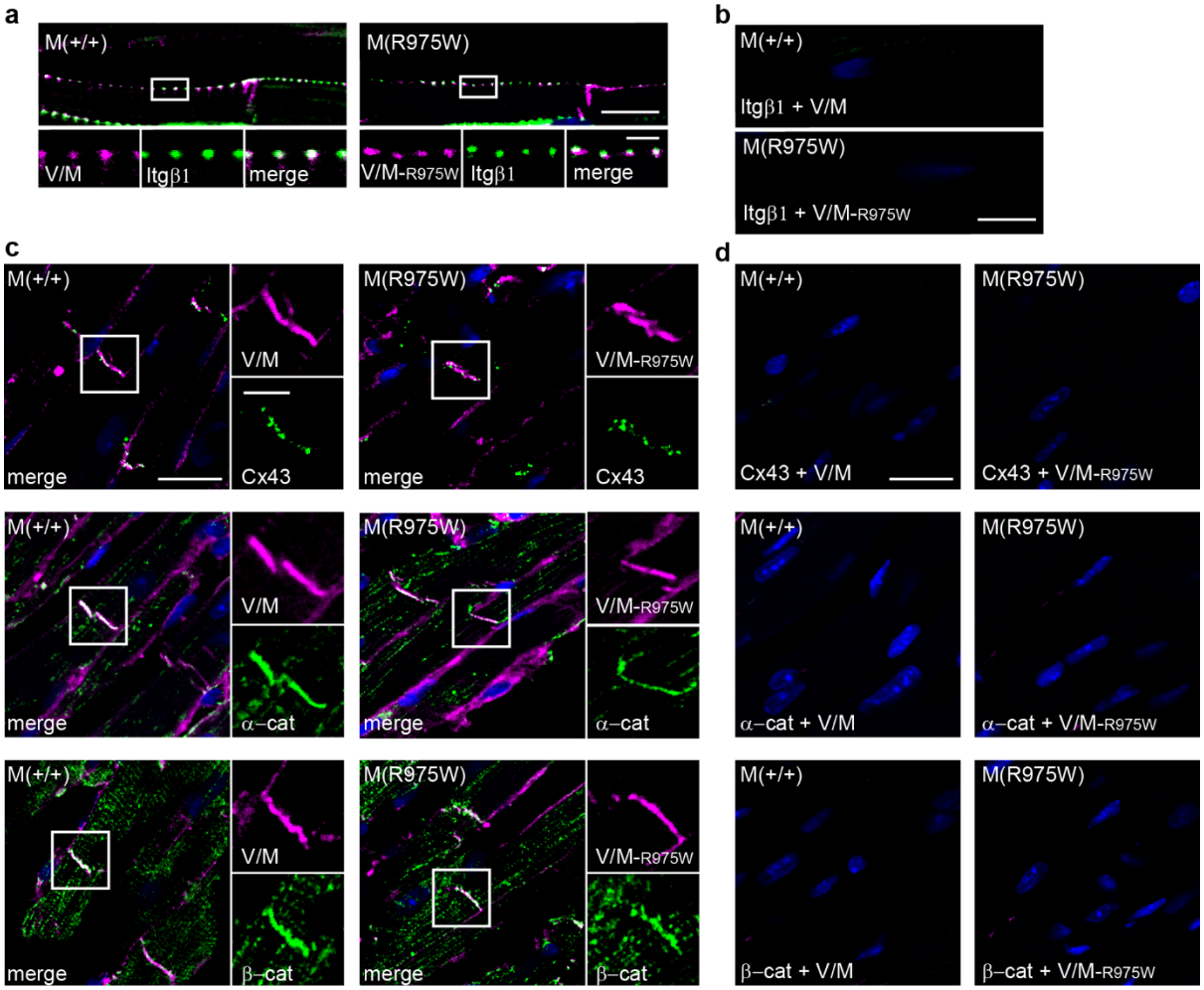

FIGURE 27: PUTATIVE CARDIOMYOPATHY MUTATION R975W IN METAVINCULIN DOES NOT ALTER TISSUE ARCHITECTURE IN MICE. No apparent difference in tissue architecture or localization of costamere, ICD and gap junction markers upon point mutation R975W in the myocardium of 6-months-old wild-type $M^{(+/+)}$ and transgenic $M^{(R975W)}$ mice. **(a)** Representative immunofluorescence stainings showing costamere marker β1 integrin (Itg β1). **(b)** Secondary antibody only control staining confirms specificity of signal observed in a. **(c)** Representative immunofluorescence images of gap junction marker connexin-43 (Cx43) and adherens junction markers α-catenin (α-cat) and β-catenin (β-cat). **(d)** Secondary antibody only control staining confirms specificity of signal observed in c. Color coding as indicated in the images and DAPI staining in blue. Scale bar: 20 µm, in zoom: 10 µm.

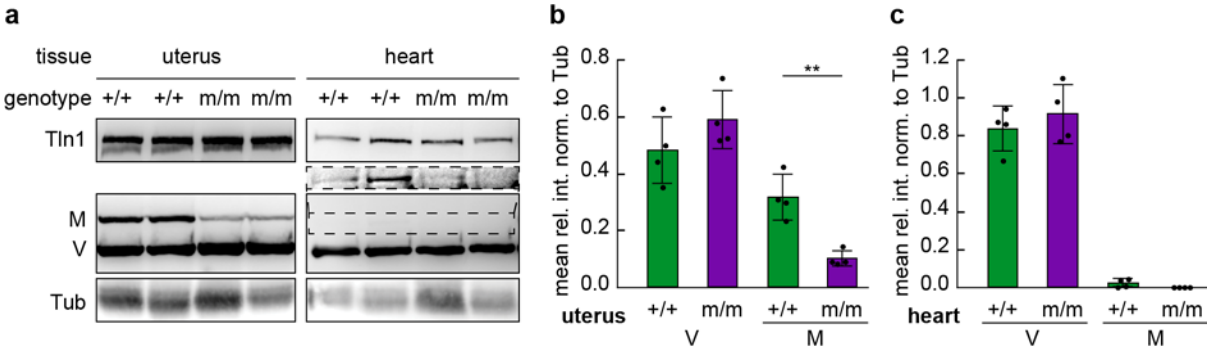

FIGURE 28: MUTATED METAVINCULIN PROTEIN LEVELS ARE REDUCED IN MUSCLE TISSUE OF TRANSGENIC MICE. (a) Representative image of Western blot analysis of muscle tissue of 6-months-old $M^{(R975W)}$ mice shows reduced M-R975W protein levels in the uterus as well as in the heart. Densitometric quantification of Western blot analysis of uterine **(b)** and cardiac **(c)** muscle tissue confirms significantly reduced M-R975W protein levels in the uterus and reveals slightly enhanced vinculin expression in both tissues (n= 4, 4, 4, 4). Two-sided students T-test, equal variance: $^{**}p < 0.01$, n.s. (not significant) $p \geq 0.05$.

4 DISCUSSION AND OUTLOOK

4.1 HIGH TENSION AND LOW ENGAGEMENT RATIOS OF VINCULIN AND METAVINCULIN

Since vinculin was first implicated in force transduction, several studies testing tension on vinculin were performed over the years using the F40-based V-TS sensitive to low piconewton forces (see 1.3.3). Measurements with this tension sensor allowed the investigation of several aspects of molecular tension as well as its observation during biological processes and revealed an average tension of 2.5 pN on vinculin in stable FAs (Grashoff et al. 2010). However, the magnitude of force experienced by single vinculin molecules remained obscure and its analysis was only made possible with the development of linker peptides sensitive to higher forces. In the present study, forces of at least 9–11 pN on both splice isoforms in FAs could be determined *in cellulo* for the first time. Notably, this result is consistent with a study by our laboratory detecting molecular forces as high as 11 pN on talin-1 and -2 (Austen et al. 2015). Furthermore, a recent single-molecule force spectroscopy study provided *in vitro* evidence for stable vinculin–talin and vinculin–α-catenin interactions at forces of 10 pN and higher (Le et al. 2019). The development of even stiffer linker peptides, will allow the determination of the maximum tension experienced by these FA proteins in the future.

While the exact engagement ratios differ between vinculin and metavinculin, only a comparably small proportion (< 30%) of the two proteins is engaged and bears tension, which is in accordance with the observation that vinculin conformation is variable at established FAs (Chen et al. 2005). Similarly, a recent study in the attachment sites of the developing flight muscle of *Drosophila* demonstrated that *in vivo* only a small proportion (< 15%) of talin is transmitting force at the same time; still high expression levels of talin molecules are required to maintain the integrity of the muscle attachment site (Lemke et al. 2019). The low engagement ratio could leave a pool of already bound or at least recruited mechanosensitive proteins, which can dynamically share the mechanical load. This hypothesis agrees with the observation, that FAs are dynamic structures (Sun et al. 2016). Furthermore, this pool might act as a buffer, which can be rapidly engaged upon a sudden increase in tension to maintain cell or tissue integrity.

4.2 REDUCED ENGAGEMENT RATIO IS COUNTERACTED BY HIGH FORCE PER MOLECULE

Up to now, tension sensor studies relied only on one or few different linker peptides thereby narrowing their findings to the inherently limited force sensitivity of the employed linker. Moreover, the analysis of FLIM-FRET data was based on FRET indices or efficiencies, which both do not allow the direct comparison of FRET changes based on different TS modules, since each module has a different starting FRET efficiency (see 1.3.2). Here, the innovative combination of two technical aspects allowed the analysis of force distribution on (meta)vinculin. First, the application of four TS modules comprising linker peptides with different force sensitivities in parallel enabled the comparison of vinculin and metavinculin force levels across the entire force range of 1–11 pN. Second, due to recent advancements in the evaluation of FLIM-FRET data (Ringer et al. 2017c; Cost 2019; Lemke et al. 2019), the fraction of mechanically engaged (meta)vinculin molecules could be determined and compared for each force range covered by the employed mechanosensitive linker peptide. Only both parameters together define how mechanical signals are transduced by molecular linkages and enabled the discovery, that overall a smaller fraction of metavinculin linkages carries mechanical load compared to vinculin; however, this fraction bears forces larger than 8 pN.

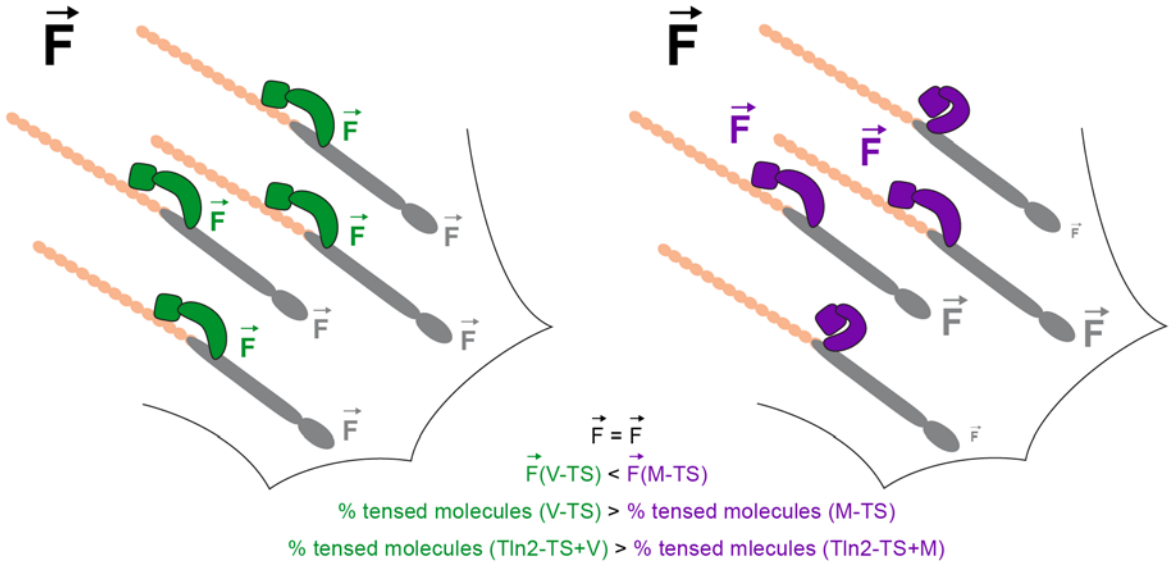

FIGURE 29: MODEL OF DIFFERENTIAL FORCE DISTRIBUTION ON FA MOLECULES. Schematic depiction of a FA in cells with the same overall cell tension. Vinculin (green) transduces on average smaller forces than metavinculin (purple) per molecule, therefore more vinculin molecules are engaged. Metavinculin reinforces less talin–actin–linkages than vinculin but leads to a stronger tension increase experienced by talin molecules (grey). Metavinculin binds to talin in its active state, but does not necessarily engage with actin (orange) to transmit force.

A simplified model, in which cells of similar size maintain the same overall cell tension $\vec{F}$, is consistent with these two findings (Figure 25): Metavinculin transduces higher forces than vinculin ($\vec{F}$(V) < $\vec{F}$(M)), while a lower percentage of metavinculin molecules is mechanically engaged (% tensed TS (V) >% tensed TS (M)). Thus, to maintain force homeostasis ($\vec{F}$=$\vec{F}$), a higher force per molecule is counteracted by a decreased engagement ratio and vice versa.

Notably, this model can also explain the intriguing observation that metavinculin leads to a less pronounced increase in the fraction of talin molecules under tension of at least 6–8 pN than vinculin (% tensed TS (Tln2-TS+V) > % tensed TS (Tln2-TS+M)). Reinforcement of the talin–actin linkage by both vinculin and metavinculin increases tension on talin and, therefore, also the fraction of talin molecules under higher tension. However, metavinculin transmits larger forces per molecule than vinculin and, therefore, the resulting force increase is larger on talin–metavinculin–actin linkages. Concomitantly, less metavinculin molecules are engaged than vinculin, leading to a smaller number of reinforced talin–actin linkages. As a result, the larger force per talin–metavinculin–actin linkage is counteracted by a smaller number of reinforced talin–actin linkages, which together leads to a smaller fraction of talin molecules under tension in the presence of metavinculin.

Based on this model, the engagement ratios of the Tln-TS in the idealized simplified FA can be approximated depending on the relative stiffness of the mechanosensitive linker. In an ideal FA the model predicts for a very soft linker 100% mechanically engaged talin molecules upon co-expression of either vinculin splice isoforms; for a moderately stiff module 100% tensed talin molecules upon vinculin expression and 50% upon metavinculin expression; and for a very stiff linker that only metavinculin co-expression leads to an increased fraction of 50% tensed talin molecules. Of note, 100 % or 0 % have never been observed in tension sensor measurements, neither *in cellulo* nor *in vitro*, due to biological restrictions such as fluorophore maturation issues, limited fluorophore distances due to the linker peptide separating the fluorophores and microenvironmental factors influencing the fluorescence signal. The results of the Tln2-TS experiments performed in this study with the HP35 linker sensitive to 6–8 pN are best reflected by the hypothetical results of the moderately stiff linker. To verify the hypothesized force distribution on talin, force measurements with Tln-TS in the presence and absence of V-B and M-B with linker peptides of different stiffness could be performed. Importantly, the predicted force thresholds might be higher or lower than the sensitivities of the currently available mechanosensitive linkers. Therefore, the development of new linkers with lower or higher force sensitivity might be required.

Of note, the here presented experiments were all performed in fibroblast cell lines, which do not naturally express metavinculin (Belkin et al. 1988b; Saga et al. 1985), whereas, *in vivo*, the two

isoforms are always co-expressed in muscle tissue (see 1.2.1). Recent experiments with HL-1 cells expressing FL-based V-TS and M-TS revealed that the (meta)vinculin splice isoform-specific FRET difference is maintained in the presence of both vinculin and metavinculin in FAs and can also be observed in cell–cell junctions (Kanoldt et al. 2020). HL-1 cells are derived from mouse atrial cardiomyocytes and naturally express metavinculin (Claycomb et al. 1998; Kanoldt et al. 2020). Future experiments, including additional linkers of different force-sensitivities, will allow the investigation of potential alterations in force distribution on (meta)vinculin in this physiologically more relevant setting. Additionally, the possibility to knock-in the TS modules into the endogenous genome locus of (meta)vinculin by the CRISPR/Cas9 system is an intriguing possibility to facilitate the interpretation of FRET data, as confounding factors such as overexpression or endogenous (meta)vinculin background would be eliminated. Easier to implement, these experiments could be complemented with an analysis of vinculin and metavinculin force distribution in FAs of V-TS and M-TS expressing vinc$^{(-/-)}$ cells additionally co-expressing either fluorescently tagged vinculin or metavinculin. An experiment performed by Dr. Carleen Kluger using F40-based tension sensors, revealed that co-expression of V-B and M-B both increased force levels on V-TS but not on M-TS (Kluger 2016). In light of the model presented in this study, the increase in V-TS FRET efficiency could indicate an increased number of vinculin molecules under lower tension due to either an increase in protein concentration at the FA and/or e.g. changes in actin bundling capacity induced by the presence of metavinculin. Alternative co-expression of specifically mutated vinculin or metavinculin (see 4.1.4) could further help to discern the reason for the altered force transduction. Further supporting this analysis, similar experiments analyzing the effect of the presence of both vinculin and metavinculin together on talin tension could be performed.

Overall, the data discussed above supports a model, in which changes in engagement ratios and force per molecule counteract each other to maintain force homeostasis. Furthermore, the importance of employing a range of mechanosensitive linker peptides suitable to the examined forces to examine force distributions, instead of relying solely on individual probes, is emphasized and will contribute to the perception of the whole picture of how molecular linkages transmit forces.

4.3 SIMILAR NUMBERS OF TALIN-1 AND TALIN-2 MOLECULES TRANSDUCE FORCE

A previous study of the Grashoff laboratory revealed elevated tension levels on talin-2 as compared to its isoform talin-1, which were ablated upon expression of the Tln-TS in vinculin-deficient cells (Austen et al. 2015). In accordance with this work, a more pronounced decrease in the FRET efficiency of Tln2-TS could be observed upon re-expression of fluorescently-tagged vinculin in vinc$^{(-/-)}$ cells. Note that conversely to the previous study a small FRET efficiency difference between the two talin isoforms

was maintained also in the absence of vinculin. This vinculin-independent force level difference was also reflected in engagement ratio analysis, which eliminates the variations in the no-force control FRET efficiencies.

Next to different molecular engagement, cells can regulate the number of molecules available in the FA by altering expression or recruitment. To include this aspect of cellular regulation in the analysis, the relative number of molecules in FAs was estimated based on the fluorescence intensity. As each TS comprises exactly one YPet fluorophore, the number of photons recorded during the FLIM experiment can be used as an approximation for the number of molecules emitting the fluorescent signal after correcting for the photon counts lost due to FRET. Comparison of the resulting FRET corrected photon counts detected during the FLIM experiments revealed a strikingly consistent reduction in intensity levels of Tln2-TS as compared Tln1-TS data, indicating a smaller recruitment of talin-2 molecules to FAs.

Calculation of the relative number of mechanically engaged Tln-TS molecules, by combining engagement ratios and FRET corrected photon counts, suggested that the same number of talin-1 and talin-2 molecules experience forces of at least 6–8 pN in the presence and absence of vinculin, even though many more talin-1 molecules would be available. Whether this difference in talin engagement is caused by differences in talin isoform activation or whether it can be altered by integrin isoform-specific expression, remains to be determined (see 1.1.5). Of note, whereas the number of tensed talin-1 molecules was equally elevated by both proteins, metavinculin expression increased the number of tensed talin-2 molecules less than vinculin. This talin isoform-specific difference is small and therefore requires further investigation, for example, by measurements with Tln-TS containing linker peptides with different force sensitivities. However, since expression levels of talin-2 and metavinculin are both contemporarily upregulated during muscle development and talin-2 displays a higher binding affinity to the muscle-specific integrin isoform integrin β1D as well as actin (Anthis et al. 2010; Koteliansky et al. 1991; Senetar et al. 2007), a specific role in modulation of force transduction involving both proteins seems reasonable.

Of note, using the FRET-corrected photon count as an approximation for the number of molecules has limitations. Variations in molecular environment of the donor fluorophore in the two talin isoforms could result in different photon counts per YPet fluorophore and therefore per molecule. In addition, the comparison of number of tensed tension sensor molecules is further complicated, because the current analysis workflow relies on an intensity-based thresholding to extract the FA-specific signal, and is thus affected by differences in signal intensity and particularly changes in signal–to–noise ratio. Furthermore, the talin-1 and talin-2 data sets were recorded at different timepoints and by different

experimentators. Consequently, unspecific secondary technical effects, such as a loss of laser power over time or different transfection efficiencies, are possible. Future experiments should therefore minimize potential sources of differences, for example, by performing the experiments in parallel. Furthermore, the precise number of photons per YPet molecule in the two talin isoform tension sensors could be determined by FCS, concomitantly enabling the calculation of the absolute number of tensed molecules in FAs. This has been done in a recent study on talin tension in the flight muscle of *Drospohila*, in which the exact number of photons corresponding to one tension sensor molecule was determined to quantify talin tension during different developmental stages characterized by increasing talin concentrations (Lemke et al. 2019). Lastly, the development of a fluorophore FRET pair with a fluorescently more active acceptor would greatly improve the sensitivity of the FRET measurements, since due to non-FRETing tension sensors currently 50–60% of the recorded signal has to be discarded during analysis of the fraction or number of engaged molecule analysis.

In conclusion, even though the new evaluation method still needs some refinements, the possibility to estimate the actual number of molecules under tension opens a new perspective on how mechanical linkages transmit forces and will enable future studies to investigate the influence of concentration differences on tension *in cellulo* as well as *in vivo*.

4.4 (META)VINCULIN ACTIVATION IS INDEPENDENT FROM ITS MECHANICAL ENGAGEMENT

A number of biochemical and structural studies established that the presence of the 68 aa metavinculin insert in the vinculin tail domain alters some of its characteristics such as activation, actin interaction and oligomerization, and cell culture studies confirmed that the two splice isoforms regulate a range of cellular process differently (see 1.2). Therefore, the question arises, which of the unique characteristics is responsible for the differences observed in force transduction of vinculin and metavinculin. In the present study, the influence of activation on differential force transduction of (meta)vinculin was examined by introducing two different sets of point mutations known to alter the head to tail interaction of vinculin, i.e. the deactivating point mutation A50I and the activating HTI mutation (see 1.2.2).

The introduction of the deactivating point mutation A50I resulted in decreased FRET efficiencies of V-TS-A50I and M-TS-A50I measured with the two different mechanosensitive linker peptides F40 and FL, indicating an increased fraction of engaged (meta)vinculin molecules transducing tension of up to 6 pN. Note, that in contrast to the here presented data, Rothenberg et al. (2018) observed a small increase in FRET efficiency in F40-based V-TS expressing cells upon introduction of the A50I mutation. The FRET efficiency reduction observed in the presented study is in accordance with a simplified

model, in which (meta)vinculin activation is regulated independently of force transmission across the two splice isoforms (Figure 30): Deactivation by A50I mutation of (meta)vinculin leads to reduced recruitment and, therefore, to a smaller number of deactivated metavinculin molecules at the FA. Contemporarily, the force per molecule ($\vec{F}$(M) = $\vec{F}$(M-A50I)) and the number of stretched molecules (# tensed molecules (M-TS) = # tensed molecules (M-TS-A50I)) remains unchanged. The combination of altered recruitment levels and unaltered force transmission, results in the measured enhanced engagement ratio of deactivated metavinculin (% tensed molecules (M-TS) < % tensed molecules (M-TS-A50I)). Of note, this hypothesis is in accordance with *in vitro* studies, demonstrating that vinculin binding requires force-induced stretch on talin but not on vinculin (del Rio et al. 2009; Yao et al. 2014a) and that a force-independent release of talin/vinculin auto-inhibition is sufficient to induce a tight interaction between the two proteins (Atherton et al. 2015). Moreover, a previous study combining FRAP with tension sensor experiments in FAs could not observe a correlation between the mobile fraction and FRET efficiency as well as turnover rates and signal intensity of V-TS, indicating that mechanical load on vinculin is not necessary to maintain the protein in the FA (Rothenberg et al. 2018). Furthermore, the observation of independent FRET efficiency changes of the V-TS and of a FRET-based vinculin conformation sensor in FAs and AJs upon reduction of actomyosin contractility by ROCK-inhibitor treatment further supports the hypothesis that (meta)vinculin activation and mechanical engagement are not directly correlated (Grashoff et al. 2010; Leerberg et al. 2014).

Since the data is currently based on measurements with the FL and the F40 linker peptide, which is not ideally suited for engagement ratio analysis due to its gradual force response (see 1.3.2), the presented model needs to be verified with analogous experiments evaluated bi-exponentially, using additional linker peptides displaying sensitivities to higher molecular forces and a more digital force-response, such as the HP35 and the HP35st linker. The measurement of an equal alteration of the fractions of tensed V- and M-TS-A50I across a wider force range would indicate a force-independent change in FRET efficiency, thereby indirectly supporting the model. Since especially the recruitment rates, visualized as fluorescence intensity in the FA, play a pivotal role in these experiments, a more direct comparison of the number of tensed molecules is preferable (see 3.1.4 and 4.1.3). However, beforehand the according data analysis workflow needs to be refined, as the current FA thresholding algorithm is not able to equally extract the FA signal from cells with too different signal–to–noise ratios, as is the case for V- and M-TS-A50I expressing vinc$^{(-/-)}$ cells.

Notably, the A50I mutation not only reduces the head to tail interaction within (meta)vinculin but also the binding affinity of (meta)vinculin for talin, as was shown in a calorimetric experiment *in vitro* using the isolated A50I-mutated vinculin head and the talin rod (Bakolitsa et al. 2004). This reduced binding

affinity likely results in a diminished ability of deactivated (meta)vinculin molecules to transmit force. According to the model presented in 4.1.2, lower force transmitted per deactivated (meta)vinculin molecule is counteracted by an increased fraction of engaged deactivated (meta)vinculin to maintain force homeostasis, thus resulting in a reduction in FRET efficiency of V- and M-TS-A50I, as well. The analysis of V- and M-TS-A50I expressing vinc$^{(-/-)}$ cells based on linker peptides with higher force sensitivities could help to differentiate between effects caused by altered talin binding affinity or by activation-dependent recruitment, since only the first are expected to result in a reduction of high forces experienced by (meta)vinculin. More likely however, both effects contributed to the measured FRET-efficiency drop, therefore emphasizing the importance of using clean separation–of–function mutations whenever possible.

The introduction of the HTI mutation into (meta)vinculin led to an aggregation phenotype, which was strongly pronounced for V-TS-HTI and only moderately observed for M-TS-HTI. This splice isoform specific difference originates presumably from a divergent oligomerization behavior of vinculin and metavinculin, whereby the ability and the conditions under which the two proteins form oligomers are controversially debated (see 1.2.3). However, the less marked aggregation phenotype of activated metavinculin is in accordance with its presumed inability to form dimers in the presence of actin. Alternatively, the distinct V-TS-HTI aggregates could also be a means of the cell to confine potentially detrimental amounts of overly activated vinculin. Further investigation of the aggregates could be conducted, to better understand their nature and emergence. The aggregation phenotype complicated FRET evaluation and added an additional layer of complexity. Fluorophore lifetimes are likely influenced by an altered molecular environment and more likely intermolecular FRET effects in tension sensor aggregates, and, therefore, the exclusion of the aggregates from FLIM-FRET analysis was decided. However, the clear identification of the aggregates was difficult in M-TS-HTI expressing vinc$^{(-/-)}$ cells due to their small size and similar fluorescence intensity compared to the regular FA signal. Furthermore, the exclusion most likely biased the calculated median FRET efficiency values by artificially altering the recruitment level of activated (meta)vinculin to the FA. Therefore, conclusions need to be drawn with reservation from the resulting FRET values and require additional independent experimental proof.

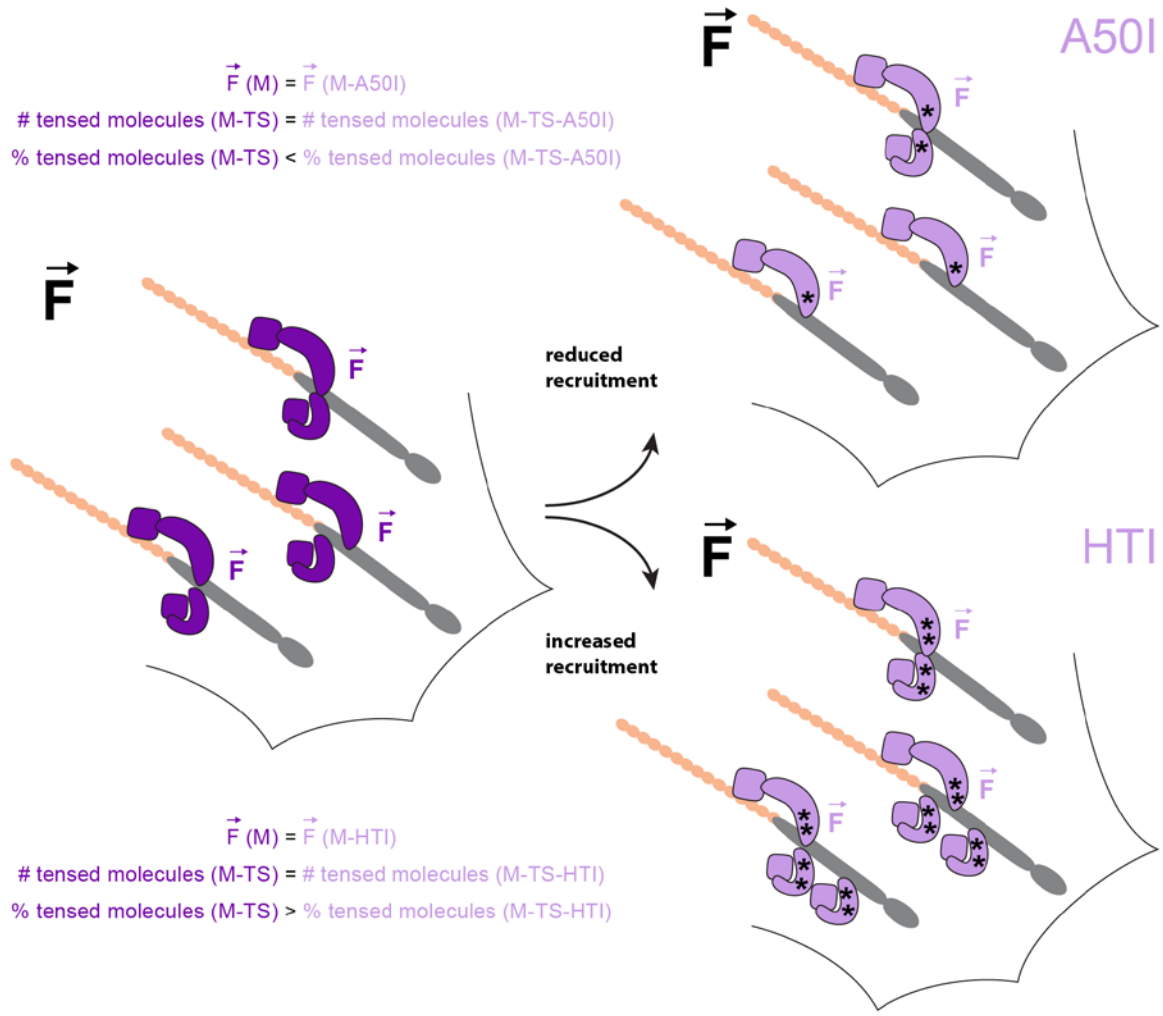

FIGURE 30: MODEL OF INDEPENDENT CHANGES IN ACTIVATION AND FORCE TRANSMISSION ON METAVINCULIN. Schematic depiction of a FA in cells with the same overall cell tension. Metavinculin (dark purple) reinforces the talin–actin linkages. Introduction of the deactivating point mutation A50I (*) into metavinculin leads to reduced recruitment of the deactivated protein to the FA, whereas force transmission remains unaltered, resulting in an increased engagement ratio. In contrast, the activating HTI mutation (**) in metavinculin induces increased recruitment of activated metavinculin to FAs. Together with unaltered force transmission, the increased number of activated metavinculin molecules lead to a reduced engagement ratio. Talin (grey), actin (orange), mutated metavinculin (light purple).

According to the previously presented model (Figure 30), the introduction of the activating HTI mutation is expected to lead to an increased recruitment of (meta)vinculin to the FA, whereas force transmission across the mutant is not altered ($\vec{F}$(M) = $\vec{F}$(M-HTI); # tensed molecules (M-TS) = # tensed molecules (M-TS-HTI)). In combination with an increased number of activated (meta)vinculin molecules present at the FA, this results in a diminished engagement ratio (% tensed molecules (M-TS) > % tensed molecules (M-TS-HTI)). Indeed, the FL-based M-TS-HTI expressing vinc$^{(-/-)}$ cells displayed an increased FRET efficiency, indicating enhanced engagement ratios of the activated protein. Contrarily, V-TS-HTI expressing cells show a strongly diminished fluorescent signal at the FAs, clearly indicating that the number of activated vinculin molecules is not increased as predicted upon the introduction of the HTI mutation. However, the decrease in FRET efficiency measured in F40-based

V-TS-HTI expressing vinc$^{(-/-)}$ cells is in accordance with the scenario predicted for reduced (meta)vinculin recruitment (compare to A50I mutation). Nevertheless, unaltered FRET efficiencies of F40-based M-TS-HTI and FL-based V-TS-HTI cannot be explained by the model.

Before further conclusions can be drawn, the HTI-based experiments need to be optimized and further controlled. To my knowledge, the aggregation phenotype of HTI-mutated vinculin was not previously reported, even though personal communication indicated that also other laboratories have encountered this issue before. Of note, an analogous experiment was performed by Dr. Carleen Kluger using F40-based V- and M-TS-HTI expressed in vinc$^{(-/-)}$ cells, but no aggregation phenotype was reported and reduced FRET efficiencies for both tension sensors upon mutation were demonstrated. Thus, first it should be tested, whether the aggregation phenotype can be avoided by controlling the expression levels of activated (meta)vinculin using e.g. an altered transfection protocol, a different promotor or genomic integration of HTI-mutated (meta)vinculin by e.g. CRISPR/Cas9. Next, the aggregation phenotype and the FRET efficiency changes observed in V- and M-TS-HTI expressing vinc$^{(-/-)}$ cells could be confirmed with the T12-mutant, which contains four corresponding charge–to–alanine mutations within the (meta)vinculin tail domain, and is the more commonly used activation mutant (see 1.2.2). Similarly to A50I-mutation experiments, the possibility to determine the actual number of molecules under tension in the FAs could further facilitate the interpretation of these experiments.

Overall, the results of the deactivating A50I and the activating HTI mutation experiments agree with a model in which (meta)vinculin is independently regulated from (meta)vinculin activation, although especially the HTI-based experiments need to be further improved and controlled. Concomitantly, since neither the activating nor the deactivating mutations ablated the vinculin splice isoform-specific FRET difference, activation does not seem to be the cause for differential force transduction of vinculin and metavinculin. To identify the root cause for this difference, several additional specific characteristics could be addressed in future tension sensor studies. Generally, the importance of certain elements, such as the H1 and H1’ helix, in the metavinculin-specific 68 aa sequence for (meta)vinculin-specific force transduction could be analyzed by systematically exchanging their sequence with the corresponding analog in vinculin and vice versa. More specifically, the difference in actin bundling capacity of the two splice isoforms has been attributed to the displaced H1 helix within the metavinculin structure (Rangarajan et al. 2010) and, therefore, the influence of deleting the sequence of this helix on metavinculin tension should be analyzed. Concomitantly, FRET-FLIM experiments could include the analysis of V-TS (and as a control M-TS) including the point mutation M898A, which was shown to ablate the bundling capacity of vinculin while preserving its ability to

bind actin (Kim et al. 2016). The cardiomyopathy associated mutations R976W, A934V and the 3-bp deletion L954del (see 1.2.1) should be included in future tension sensor experiments, as well. Furthermore, the presence of metavinculin has been shown to reduce the ability of vinculin to bundle actin filaments, whereas M-R975W failed to do so (Sarker et al. 2019). Consequently, the effect of co-expression of fluorescently tagged metavinculin or M-R975W on V-TS, and as a control M-TS, could be investigated using an experimental set-up described in 4.1.2.. Moreover, several mutations are published which would be suited to investigate the influence of differential membrane as well as Raver-1 binding on (meta)vinculin force transduction (Lee et al. 2012; Chinthalapudi et al. 2016). It is important to note, that all mutants, and especially larger truncations, should be controlled for their structural integrity by e.g. circular dichroism spectroscopy and predicted changes in binding affinity should be verified by e.g. actin co-sedimentation. Together, these experiments will enable the identification of the characteristics of (meta)vinculin responsible for differential force transduction and thereby shed light on how (meta)vinculin transduces tension.

4.5 METAVINCULIN IS DISPENSABLE FOR HEART FUNCTION

The functional role of vinculin has long been studied and vinculin expression was demonstrated to be essential in a homozygous knockout mouse study (Xu et al. 1998). Also, global as well as cardiomyocyte-specific reduction of (meta)vinculin expression levels predispose mice to development of cardiomyopathy emphasizing the importance of (meta)vinculin for heart function (Zemljic-Harpf et al. 2007; Zemljic-Harpf et al. 2004). However, these studies did not allow to differentiate between isoform-specific effects, as metavinculin was ablated or reduced together with vinculin. To overcome this limitation, the role of metavinculin in pathophysiology of the muscle was analyzed in a metavinculin knockout mouse model. Histological and biochemical characterization of these $M^{(-/-)}$ animals with a focus on the heart muscle, demonstrated that heart muscle development and function are not impaired upon loss of metavinculin alone. Additional experiments including ultrastructural analysis might still reveal subtle differences in ICD and costamere structure; however, it can be concluded that metavinculin loss is not detrimental for mice under the tested conditions.

Since metavinculin transduces high forces per molecule, a role in force transduction under muscle stress conditions was anticipated. However, $M^{(-/-)}$ animals displayed an indistinguishable hypertrophy response to left ventricular pressure overload induced by TAC. Of note, metavinculin expression levels did not seem to be upregulated upon TAC. However, resolving the small difference in molecular weight with an antibody recognizing both isoforms by Western blot analysis in heart muscle tissue proved to be challenging, due to a very low expression level ratio of metavinculin to vinculin combined with a tendency of metavinculin to degrade in these samples. Development of a functional metavinculin-

specific antibody together with short storage times before analysis would improve the reliability of Western blot analysis and further allow the investigation of currently potentially disguised small expression and recruitment level changes as well as isoform-specific localization in muscle tissue sections in future experiments.

Next to pathologically induced cardiac hypertrophy, also physiological stimuli, such as exercise or pregnancy, can induce mechanical stress on the heart each inducing distinct cellular signaling pathways. While the former generally progresses into a maladaptive phase resulting in heart failure, physiological hypertrophy is reversible and characterized by a normal or even enhanced cardiac function (Chung and Leinwand 2014; Abbas et al. 2005). $M^{(-/-)}$ female mice did not seem to display problems during birth and individuals mated several times during their lifespan seemed to reproduce at inconspicuous rates similar to their wild-type littermates. A targeted investigation of heart structure and function of pregnant $M^{(-/-)}$ or the examination of knockout animals subdued to a treadmilling protocol, could help to exclude an essential function of metavinculin specific to the physiological stress response in future studies.

Besides metavinculin deficiency, studies on human patient cohorts associated mostly mutations in the metavinculin-specific insert with cardiomyopathy. Because humans with the R975W mutation displayed the pathologically most severe cardiac phenotype, the effect of this mutation was investigated in the $M^{(R975W)}$ mouse model. While $M^{(R975W)}$ mice displayed unaltered heart tissue architecture and were viable and fertile, M-R975W was down-regulated in the muscle tissue of the heart and the uterus. In line with the observations of the metavinculin knock-out mouse line, the results suggest that loss or reduction of metavinculin protein levels is beneficial over the presence of M-R975W in muscle tissue and might compensate for a potentially detrimental effect of the mutated protein. Whether M-R975W down-regulation is caused by reduced expression or an increased degradation of the protein remains to be investigated, and should be complemented by analysis of force distribution on M-R975W in tension sensor experiments in cells. Even though heart tissue architecture of $M^{(R975W)}$ was intact, heart function should be analyzed by e.g. echocardiography and in a pathological, and potentially also physiological, cardiac stress condition model such as TAC. Notably, the highest expression level of metavinculin with up to 40% of total (meta)vinculin is found in the uterus (see 1.2.1), which during pregnancy is subjected to a profound mechanical challenge, since embryonic growth requires constant adaptation in passive tension, whereas at maximum extension strong contractile forces are required at birth. Therefore, future studies could investigate the importance of metavinculin and the R975W mutation for the myometrium, potentially revealing a specific role of metavinculin for passive or active muscle tension.

Note that the power of studies on heart function in mice are limited, as mice differ strongly from humans in terms of body and heart size (Milani-Nejad and Janssen 2014). Nonetheless, it can be concluded, that metavinculin seems to play only a minor role in heart muscle disease especially compared to established cardiomyopathy genes like titin (Herman et al. 2012) or desmoplakin (Yang et al. 2006). Indeed, this observation is supported by the *in cellulo* experiments of this study, in which the consistent differences in force transduction of (meta)vinculin are not accompanied by obvious morphological changes of the cells under steady state conditions. Still, a more subtle function of loss of metavinculin in cardiopathology remains possible and might cause a genetic predisposition requiring additional modifier genes or environmental stressors to result in cardiomyopathy. The significance of the R975W mutation in metavinculin still needs to be fully evaluated; however, in case that M-R975W is involved in cardiomyopathy, the absent to potentially very mild effect of metavinculin loss could be exploited for gene therapy.

5 ACKNOWLEDGMENTS

I would like to thank Prof. Dr. Carsten Grashoff for the opportunity to do my PhD thesis in his laboratory at the Max-Planck-Institute of Biochemistry in Martinsried and later the Westfälische Wilhelms-Universität in Münster. Thank you for always being interested in discussing my experiments and helping me to keep the big picture in sight by asking the critical questions. I am further grateful for your support for me to finish my thesis in Munich and for the fruitful exchange during the publication of our paper – it was an experience that I would not like to miss.

Furthermore, I would like to thank Prof. Dr. Dr. Stefan Engelhardt, who agreed to supervise me and was together with Prof. Dr. Matthias Rief and Dr. Markus Moser part of my Thesis Advisory Committee (TAC). The TAC meetings gave me the opportunity to sort and concisely present my finding to a team of experts, whose input I greatly appreciated. Additionally, the collaboration with Prof. Engelhardt and his laboratory further helped me to solidify my findings on the Metavinculin knock-out mouse model. Special thank goes to Vanessa, Deepak, Julia, Anton and Sabine. Moreover, I would like to thank Prof. Reinhard Fässler for generously providing access to the facilities of his department and constructive criticism during Department Seminars. Additionally, I would like to thank the members of the Fässler Department and especially Sarah, Shengzhen, Peter, Armin, Michael and Klaus as well as friends and colleagues throughout the MPIB for your scientific and moral support.

Most importantly, I would like to thank the members of the Grashoff laboratory. Thank you, Anna, for your excellent supervision in mouse handling as well as your organization of not only the mice but also the entire laboratory. It was a pleasure to have you as a bench neighbor and I enjoyed our time in the mouse house together. Thank you, Anna-Lena, for your great and important moral support as well as your willingness to discuss my scientific thoughts and theories any time - my project and I benefited greatly. Thank you, Carleen, from which I took over the metavinculin project, for sticking around and supporting me and the project any time I needed even years after you have moved on to new shores which cannot be taken for granted. Thank you, Lisa and Christoph for fun stress-releasing game inventions and the rest of the lab Chris, Andrea, Kathi and Pia for a supporting lab atmosphere. Big thank goes to the von Blume lab with Biggi, Natalia, Gisela, Tobi, Mehrshad and Mai Ly, who were a great escape haven and had chocolate whenever needed most. Not to forget, thank you to the new Grashoff laboratory, for your kind reception and support during my revision experiments in Münster.

Lastly, I would like to thank my family, my partner and friends. You inspired, encouraged and supported me throughout my thesis and gave me the strength never to give up.

6 PUBLICATION BIBLIOGRAPHY

Abbas, A. E.; Lester, S. J.; Connolly, H. (2005): Pregnancy and the cardiovascular system. In *International journal of cardiology* 98 (2), pp. 179–189. DOI: 10.1016/j.ijcard.2003.10.028.

Abe, K.; Takeichi, M. (2008): EPLIN mediates linkage of the cadherin catenin complex to F-actin and stabilizes the circumferential actin belt. In *Proceedings of the National Academy of Sciences of the United States of America* 105 (1), pp. 13–19. DOI: 10.1073/pnas.0710504105.

Acharya, B. R.; Wu, S. K.; Lieu, Z. Z.; Parton, R. G.; Grill, S. W.; Bershadsky, A. D. et al. (2017): Mammalian Diaphanous 1 Mediates a Pathway for E-cadherin to Stabilize Epithelial Barriers through Junctional Contractility. In *Cell Rep* 18 (12), pp. 2854–2867. DOI: 10.1016/j.celrep.2017.02.078.

Adams, D. J.; Quail, M. A.; Cox, T.; van der Weyden, L.; Gorick, B. D.; Su, Q. et al. (2005): A genome-wide, end-sequenced 129Sv BAC library resource for targeting vector construction. In *Genomics* 86 (6), pp. 753–758. DOI: 10.1016/j.ygeno.2005.08.003.

Anthis, N. J.; Wegener, K. L.; Critchley, D. R.; Campbell, I. D. (2010): Structural diversity in integrin/talin interactions. In *Structure (London, England : 1993)* 18 (12), pp. 1654–1666. DOI: 10.1016/j.str.2010.09.018.

Atherton, P.; Stutchbury, B.; Wang, D. Y.; Jethwa, D.; Tsang, R.; Meiler-Rodriguez, E. et al. (2015): Vinculin controls talin engagement with the actomyosin machinery. In *Nat Commun* 6. DOI: 10.1038/ncomms10038.

Austen, K.; Kluger, C.; Freikamp, A.; Chrostek-Grashoff, A.; Grashoff, C. (2013): Generation and analysis of biosensors to measure mechanical forces within cells. In *Methods in molecular biology (Clifton, N.J.)* 1066, pp. 169–184. DOI: 10.1007/978-1-62703-604-7_15.

Austen, K.; Ringer, P.; Mehlich, A.; Chrostek-Grashoff, A.; Kluger, C.; Klingner, C. et al. (2015): Extracellular rigidity sensing by talin isoform-specific mechanical linkages. In *Nat Cell Biol* 17 (12), pp. 1597–1606. DOI: 10.1038/ncb3268.

Bakolitsa, C.; Cohen, D. M.; Bankston, L. A.; Bobkov, A. A.; Cadwell, G. W.; Jennings, L. et al. (2004): Structural basis for vinculin activation at sites of cell adhesion. In *Nature* 430 (6999), pp. 583–586. DOI: 10.1038/nature02610.

Bakolitsa, C.; Pereda, J. M. de; Bagshaw, C. R.; Critchley, D. R.; Liddington, R. C. (1999): Crystal structure of the vinculin tail suggests a pathway for activation. In *Cell* 99 (6), pp. 603–613. DOI: 10.1016/s0092-8674(00)81549-4.

Barry, A. K.; Tabdili, H.; Muhamed, I.; Wu, J.; Shashikanth, N.; Gomez, G. A. et al. (2014): α-catenin cytomechanics--role in cadherin-dependent adhesion and mechanotransduction. In *J Cell Sci* 127 (Pt 8), pp. 1779–1791. DOI: 10.1242/jcs.139014.

Barstead, R. J.; Waterston, R. H. (1991): Vinculin is essential for muscle function in the nematode. In *J Cell Biol* 114 (4), pp. 715–724. DOI: 10.1083/jcb.114.4.715.

Bays, J. L.; DeMali, K. A. (2017): Vinculin in cell-cell and cell-matrix adhesions. In *Cellular and molecular life sciences : CMLS* 74 (16), pp. 2999–3009. DOI: 10.1007/s00018-017-2511-3.

Bays, J. L.; Peng, X.; Tolbert, C. E.; Guilluy, C.; Angell, A. E.; Pan, Y. et al. (2014): Vinculin phosphorylation differentially regulates mechanotransduction at cell-cell and cell-matrix adhesions. In *J Cell Biol* 205 (2), pp. 251–263. DOI: 10.1083/jcb.201309092.

Belkin, A. M.; Ornatsky, O. I.; Glukhova, M. A.; Koteliansky, V. E. (1988a): Immunolocalization of meta-vinculin in human smooth and cardiac muscles. In *J Cell Biol* 107 (2), pp. 545–553. DOI: 10.1083/jcb.107.2.545.

Belkin, A. M.; Ornatsky, O. I.; Kabakov, A. E.; Glukhova, M. A.; Koteliansky, V. E. (1988b): Diversity of vinculin/meta-vinculin in human tissues and cultivated cells. Expression of muscle specific variants of vinculin in human aorta smooth muscle cells. In *J Biol Chem* 263 (14), pp. 6631–6635.

Benoit, M.; Gabriel, D.; Gerisch, G.; Gaub, H. E. (2000): Discrete interactions in cell adhesion measured by single-molecule force spectroscopy. In *Nat Cell Biol* 2 (6), pp. 313–317. DOI: 10.1038/35014000.

Bertocchi, C.; Wang, Y.; Ravasio, A.; Hara, Y.; Wu, Y.; Sailov, T. et al. (2017): Nanoscale architecture of cadherin-based cell adhesions. In *Nat Cell Biol* 19 (1), pp. 28–37. DOI: 10.1038/ncb3456.

Betz, U. A.; Vosshenrich, C. A.; Rajewsky, K.; Müller, W. (1996): Bypass of lethality with mosaic mice generated by Cre-loxP-mediated recombination. In *Curr Biol* 6 (10), pp. 1307–1316. DOI: 10.1016/s0960-9822(02)70717-3.

Borghi, N.; Sorokina, M.; Shcherbakova, O. G.; Weis, W. I.; Pruitt, B. L.; Nelson, W. J.; Dunn, A. R. (2012): E-cadherin is under constitutive actomyosin-generated tension that is increased at cell-cell contacts upon externally applied stretch. In *Proceedings of the National Academy of Sciences of the United States of America* 109 (31), pp. 12568–12573. DOI: 10.1073/pnas.1204390109.

Brangwynne, C. P.; MacKintosh, F. C.; Weitz, D. A. (2007): Force fluctuations and polymerization dynamics of intracellular microtubules. In *P Natl Acad Sci USA* 104 (41), pp. 16128–16133. DOI: 10.1073/pnas.0703094104.

Brindle, N. P.; Holt, M. R.; Davies, J. E.; Price, C. J.; Critchley, D. R. (1996): The focal-adhesion vasodilator-stimulated phosphoprotein (VASP) binds to the proline-rich domain in vinculin. In *The Biochemical journal* 318 (Pt 3) (Pt 3), pp. 753–757. DOI: 10.1042/bj3180753.

Buckley, C. D.; Tan, J. Y.; Anderson, K. L.; Hanein, D.; Volkmann, N.; Weis, W. I. et al. (2014): The minimal cadherin-catenin complex binds to actin filaments under force. In *Science (New York, N.Y.)* 346 (6209), 600-+. DOI: 10.1126/science.1254211.

Cai, D.; Chen, S.-C.; Prasad, M.; He, L.; Wang, X.; Choesmel-Cadamuro, V. et al. (2014): Mechanical feedback through E-cadherin promotes direction sensing during collective cell migration. In *Cell* 157 (5), pp. 1146–1159. DOI: 10.1016/j.cell.2014.03.045.

Carisey, A.; Tsang, R.; Greiner, A. M.; Nijenhuis, N.; Heath, N.; Nazgiewicz, A. et al. (2013): Vinculin regulates the recruitment and release of core focal adhesion proteins in a force-dependent manner. In *Curr Biol* 23 (4), pp. 271–281. DOI: 10.1016/j.cub.2013.01.009.

Chang, C.-W.; Kumar, S. (2013): Vinculin tension distributions of individual stress fibers within cell-matrix adhesions. In *J Cell Sci* 126 (Pt 14), pp. 3021–3030. DOI: 10.1242/jcs.119032.

Chen, H.; Cohen, D. M.; Choudhury, D. M.; Kioka, N.; Craig, S. W. (2005): Spatial distribution and functional significance of activated vinculin in living cells. In *The Journal of cell biology* 169 (3), pp. 459–470. DOI: 10.1083/jcb.200410100.

Chinthalapudi, K.; Rangarajan, E. S.; Brown, D. T.; Izard, T. (2016): Differential lipid binding of vinculin isoforms promotes quasi-equivalent dimerization. In *Proceedings of the National Academy of Sciences of the United States of America* 113 (34), pp. 9539–9544. DOI: 10.1073/pnas.1600702113.

Chinthalapudi, K.; Rangarajan, E. S.; Patil, D. N.; George, E. M.; Brown, D. T.; Izard, T. (2014): Lipid binding promotes oligomerization and focal adhesion activity of vinculin. In *The Journal of cell biology* 207 (5), pp. 643–656. DOI: 10.1083/jcb.201404128.

Chopard, A.; Pons, F.; Marini, J.-F. (2002): Vinculin and meta-vinculin in fast and slow rat skeletal muscle before and after hindlimb suspension. In *Pflugers Archiv : European journal of physiology* 444 (5), pp. 627–633. DOI: 10.1007/s00424-002-0872-3.

Chorev, D. S.; Volberg, T.; Livne, A.; Eisenstein, M.; Martins, B.; Kam, Z. et al. (2018): Conformational states during vinculin unlocking differentially regulate focal adhesion properties. In *Scientific reports* 8 (1), p. 2693. DOI: 10.1038/s41598-018-21006-8.

Chung, E.; Leinwand, L. A. (2014): Pregnancy as a cardiac stress model. In *Cardiovascular research* 101 (4), pp. 561–570. DOI: 10.1093/cvr/cvu013.

Claycomb, W. C.; Lanson, N. A., JR; Stallworth, B. S.; Egeland, D. B.; Delcarpio, J. B.; Bahinski, A.; Izzo, N. J., JR (1998): HL-1 cells: a cardiac muscle cell line that contracts and retains phenotypic characteristics of the adult cardiomyocyte. In *Proceedings of the National Academy of Sciences of the United States of America* 95 (6), pp. 2979–2984. DOI: 10.1073/pnas.95.6.2979.

Cohen, D. M.; Chen, H.; Johnson, R. P.; Choudhury, B.; Craig, S. W. (2005): Two distinct head-tail interfaces cooperate to suppress activation of vinculin by talin. In *The Journal of biological chemistry* 280 (17), pp. 17109–17117. DOI: 10.1074/jbc.M414704200.

Cohen, D. M.; Kutscher, B.; Chen, H.; Murphy, D. B.; Craig, S. W. (2006): A conformational switch in vinculin drives formation and dynamics of a talin-vinculin complex at focal adhesions. In *J Biol Chem* 281 (23), pp. 16006–16015. DOI: 10.1074/jbc.M600738200.

Conti, F. J.; Monkley, S. J.; Wood, M. R.; Critchley, D. R.; Müller, U. (2009): Talin 1 and 2 are required for myoblast fusion, sarcomere assembly and the maintenance of myotendinous junctions. In *Development (Cambridge, England)* 136 (21), pp. 3597–3606. DOI: 10.1242/dev.035857.

Conway, D. E.; Breckenridge, M. T.; Hinde, E.; Gratton, E.; Chen, C. S.; Schwartz, M. A. (2013): Fluid shear stress on endothelial cells modulates mechanical tension across VE-cadherin and PECAM-1. In *Curr Biol* 23 (11), pp. 1024–1030. DOI: 10.1016/j.cub.2013.04.049.

Cost, A.-L. (2019): Molecular force measurements in desmosomes. Ludwig-Maximilians-Universität München.

Cost, A.-L.; Khalaji, S.; Grashoff, C. (2019): Genetically Encoded FRET-Based Tension Sensors. In *Current protocols in cell biology* 83 (1), e85. DOI: 10.1002/cpcb.85.

Cost, A.-L.; Ringer, P.; Chrostek-Grashoff, A.; Grashoff, C. (2015): How to Measure Molecular Forces in Cells: A Guide to Evaluating Genetically-Encoded FRET-Based Tension Sensors. In *Cellular and molecular bioengineering* 8 (1), pp. 96–105. DOI: 10.1007/s12195-014-0368-1.

del Rio, A.; Perez-Jimenez, R.; Liu, R.; Roca-Cusachs, P.; Fernandez, J. M.; Sheetz, M. P. (2009): Stretching single talin rod molecules activates vinculin binding. In *Science (New York, N.Y.)* 323 (5914), pp. 638–641. DOI: 10.1126/science.1162912.

DeMali, K. A.; Barlow, C. A.; Burridge, K. (2002): Recruitment of the Arp2/3 complex to vinculin. coupling membrane protrusion to matrix adhesion. In *The Journal of cell biology* 159 (5), pp. 881–891. DOI: 10.1083/jcb.200206043.

DeMali, K. A.; Jue, A. L.; Burridge, K. (2006): IpaA targets beta1 integrins and rho to promote actin cytoskeleton rearrangements necessary for Shigella entry. In *J Biol Chem* 281 (51), pp. 39534–39541. DOI: 10.1074/jbc.M605939200.

Demeautis, C.; Sipieter, F.; Roul, J.; Chapuis, C.; Padilla-Parra, S.; Riquet, F. B.; Tramier, M. (2017): Multiplexing PKA and ERK1&2 kinases FRET biosensors in living cells using single excitation wavelength dual colour FLIM. In *Scientific reports* 7, p. 41026. DOI: 10.1038/srep41026.

Diez, G.; Auernheimer, V.; Fabry, B.; Goldmann, W. H. (2011): Head/tail interaction of vinculin influences cell mechanical behavior. In *Biochem Bioph Res Co* 406 (1), pp. 85–88. DOI: 10.1016/j.bbrc.2011.01.115.

Dupont, S.; Morsut, L.; Aragona, M.; Enzo, E.; Giulitti, S.; Cordenonsi, M. et al. (2011): Role of YAP/TAZ in mechanotransduction. In *Nature* 474 (7350), pp. 179–183. DOI: 10.1038/nature10137.

Eder, D.; Basler, K.; Aegerter, C. M. (2017): Challenging FRET-based E-Cadherin force measurements in Drosophila. In *Scientific reports* 7 (1), p. 13692. DOI: 10.1038/s41598-017-14136-y.

Ehler, E. (2016): Cardiac cytoarchitecture - why the "hardware" is important for heart function! In *Biochimica et biophysica acta* 1863 (7 Pt B), pp. 1857–1863. DOI: 10.1016/j.bbamcr.2015.11.006.

Elsherif, L.; Huang, M. S.; Shai, S.-Y.; Yang, Y.; Li, R. Y.; Chun, J. et al. (2008): Combined deficiency of dystrophin and beta1 integrin in the cardiac myocyte causes myocardial dysfunction, fibrosis and calcification. In *Circ Res* 102 (9), pp. 1109–1117. DOI: 10.1161/CIRCRESAHA.108.173153.

Engler, A. J.; Sen, S.; Sweeney, H. L.; Discher, D. E. (2006): Matrix elasticity directs stem cell lineage specification. In *Cell* 126 (4), pp. 677–689. DOI: 10.1016/j.cell.2006.06.044.

Fässler, R.; Meyer, M. (1995): Consequences of lack of beta 1 integrin gene expression in mice. In *Genes & development* 9 (15), pp. 1896–1908. DOI: 10.1101/gad.9.15.1896.

Feramisco, J. R.; Smart, J. E.; Burridge, K.; Helfman, D. M.; Thomas, G. P. (1982): Co-existence of vinculin and a vinculin-like protein of higher molecular weight in smooth muscle. In *J Biol Chem* 257 (18), pp. 11024–11031.

Fomovsky, G. M.; Thomopoulos, S.; Holmes, J. W. (2010): Contribution of extracellular matrix to the mechanical properties of the heart. In *Journal of molecular and cellular cardiology* 48 (3), pp. 490–496. DOI: 10.1016/j.yjmcc.2009.08.003.

Freeman, P. M.; Natarajan, R. N.; Kimura, J. H.; Andriacchi, T. P. (1994): Chondrocyte cells respond mechanically to compressive loads. In *Journal of orthopaedic research : official publication of the Orthopaedic Research Society* 12 (3), pp. 311–320. DOI: 10.1002/jor.1100120303.

Freikamp, A.; Cost, A.-L.; Grashoff, C. (2016): The Piconewton Force Awakens: Quantifying Mechanics in Cells. In *Trends Cell Biol* 26 (11), pp. 838–847. DOI: 10.1016/j.tcb.2016.07.005.

Freikamp, A.; Mehlich, A.; Klingner, C.; Grashoff, C. (2017): Investigating piconewton forces in cells by FRET-based molecular force microscopy. In *Journal of structural biology* 197 (1), pp. 37–42. DOI: 10.1016/j.jsb.2016.03.011.

Gaetani, R.; Zizzi, E. A.; Deriu, M. A.; Morbiducci, U.; Pesce, M.; Messina, E. (2020): When Stiffness Matters: Mechanosensing in Heart Development and Disease. In *Frontiers in cell and developmental biology* 8, p. 334. DOI: 10.3389/fcell.2020.00334.

Gauthier, N. C.; Masters, T. A.; Sheetz, M. P. (2012): Mechanical feedback between membrane tension and dynamics. In *Trends Cell Biol* 22 (10), pp. 527–535. DOI: 10.1016/j.tcb.2012.07.005.

Geiger, B.; Spatz, J. P.; Bershadsky, A. D. (2009): Environmental sensing through focal adhesions. In *Nature reviews. Molecular cell biology* 10 (1), pp. 21–33. DOI: 10.1038/nrm2593.

Gibson, D. G.; Young, L.; Chuang, R.-Y.; Venter, J. C.; Hutchison, C. A. 3.; Smith, H. O. (2009): Enzymatic assembly of DNA molecules up to several hundred kilobases. In *Nat Methods* 6 (5), pp. 343–345. DOI: 10.1038/nmeth.1318.

Gilbert, P. M.; Havenstrite, K. L.; Magnusson, K. E.; Sacco, A.; Leonardi, N. A.; Kraft, P. et al. (2010): Substrate elasticity regulates skeletal muscle stem cell self-renewal in culture. In *Science (New York, N.Y.)* 329 (5995), pp. 1078–1081. DOI: 10.1126/science.1191035.

Gingras, A. R.; Ziegler, W. H.; Frank, R.; Barsukov, I. L.; Roberts, G. C. K.; Critchley, D. R.; Emsley, J. (2005): Mapping and consensus sequence identification for multiple vinculin binding sites within the talin rod. In *J Biol Chem* 280 (44), pp. 37217–37224. DOI: 10.1074/jbc.M508060200.

González, A.; López, B.; Ravassa, S.; San José, G.; Díez, J. (2019): The complex dynamics of myocardial interstitial fibrosis in heart failure. Focus on collagen cross-linking. In *Biochimica et biophysica acta. Molecular cell research* 1866 (9), pp. 1421–1432. DOI: 10.1016/j.bbamcr.2019.06.001.

Gough, R. E.; Goult, B. T. (2018): The tale of two talins - two isoforms to fine-tune integrin signalling. In *FEBS letters* 592 (12), pp. 2108–2125. DOI: 10.1002/1873-3468.13081.

Grashoff, C.; Hoffman, B. D.; Brenner, M. D.; Zhou, R.; Parsons, M.; Yang, M. T. et al. (2010): Measuring mechanical tension across vinculin reveals regulation of focal adhesion dynamics. In *Nature* 466 (7303), pp. 263–266. DOI: 10.1038/nature09198.

Gross, L. A.; Baird, G. S.; Hoffman, R. C.; Baldridge, K. K.; Tsien, R. Y. (2000): The structure of the chromophore within DsRed, a red fluorescent protein from coral. In *Proceedings of the National Academy of Sciences of the United States of America* 97 (22), pp. 11990–11995. DOI: 10.1073/pnas.97.22.11990.

Gudipaty, S. A.; Lindblom, J.; Loftus, P. D.; Redd, M. J.; Edes, K.; Davey, C. F. et al. (2017): Mechanical stretch triggers rapid epithelial cell division through Piezo1. In *Nature* 543 (7643), 118-+. DOI: 10.1038/nature21407.

Haegel, H.; Larue, L.; Ohsugi, M.; Fedorov, L.; Herrenknecht, K.; Kemler, R. (1995): Lack of beta-catenin affects mouse development at gastrulation. In *Development (Cambridge, England)* 121 (11), pp. 3529–3537.

Hahn, C.; Schwartz, M. A. (2009): Mechanotransduction in vascular physiology and atherogenesis. In *Nature reviews. Molecular cell biology* 10 (1), pp. 53–62. DOI: 10.1038/nrm2596.

Halbleib, J. M.; Nelson, W. J. (2006): Cadherins in development: cell adhesion, sorting, and tissue morphogenesis. In *Genes & development* 20 (23), pp. 3199–3214. DOI: 10.1101/gad.1486806.

Harris, A. R.; Jreij, P.; Fletcher, D. A. (2018): Mechanotransduction by the Actin Cytoskeleton. Converting Mechanical Stimuli into Biochemical Signals. In *Annu Rev Biophys* 47, pp. 617–631. DOI: 10.1146/annurev-biophys-070816-033547.

Harrison, O. J.; Jin, X.; Hong, S.; Bahna, F.; Ahlsen, G.; Brasch, J. et al. (2011): The extracellular architecture of adherens junctions revealed by crystal structures of type I cadherins. In *Structure (London, England : 1993)* 19 (2), pp. 244–256. DOI: 10.1016/j.str.2010.11.016.

Hartsock, A.; Nelson, W. J. (2008): Adherens and tight junctions: structure, function and connections to the actin cytoskeleton. In *Biochimica et biophysica acta* 1778 (3), pp. 660–669. DOI: 10.1016/j.bbamem.2007.07.012.

Hemmatian, H.; Bakker, A. D.; Klein-Nulend, J.; van Lenthe, G. H. (2017): Aging, Osteocytes, and Mechanotransduction. In *Current osteoporosis reports* 15 (5), pp. 401–411. DOI: 10.1007/s11914-017-0402-z.

Hendrix, J.; Flors, C.; Dedecker, P.; Hofkens, J.; Engelborghs, Y. (2008): Dark states in monomeric red fluorescent proteins studied by fluorescence correlation and single molecule spectroscopy. In *Biophysical journal* 94 (10), pp. 4103–4113. DOI: 10.1529/biophysj.107.123596.

Herman, D. S.; Lam, L.; Taylor, M. R. G.; Wang, L.; Teekakirikul, P.; Christodoulou, D. et al. (2012): Truncations of titin causing dilated cardiomyopathy. In *The New England journal of medicine* 366 (7), pp. 619–628. DOI: 10.1056/NEJMoa1110186.

Hernández-Varas, P.; Berge, U.; Lock, J. G.; Strömblad, S. (2015): A plastic relationship between vinculin-mediated tension and adhesion complex area defines adhesion size and lifetime. In *Nat Commun* 6, p. 7524. DOI: 10.1038/ncomms8524.

Hirschy, A.; Croquelois, A.; Perriard, E.; Schoenauer, R.; Agarkova, I.; Hoerstrup, S. P. et al. (2010): Stabilised beta-catenin in postnatal ventricular myocardium leads to dilated cardiomyopathy and premature death. In *Basic research in cardiology* 105 (5), pp. 597–608. DOI: 10.1007/s00395-010-0101-8.

Hirschy, A.; Schatzmann, F.; Ehler, E.; Perriard, J.-C. (2006): Establishment of cardiac cytoarchitecture in the developing mouse heart. In *Developmental biology* 289 (2), pp. 430–441. DOI: 10.1016/j.ydbio.2005.10.046.

Hoffman, B. D.; Grashoff, C.; Schwartz, M. A. (2011): Dynamic molecular processes mediate cellular mechanotransduction. In *Nature* 475 (7356), pp. 316–323. DOI: 10.1038/nature10316.

Hoffman, L. M.; Jensen, C. C.; Chaturvedi, A.; Yoshigi, M.; Beckerle, M. C. (2012): Stretch-induced actin remodeling requires targeting of zyxin to stress fibers and recruitment of actin regulators. In *Molecular biology of the cell* 23 (10), pp. 1846–1859. DOI: 10.1091/mbc.E11-12-1057.

Huang, D. L.; Bax, N. A.; Buckley, C. D.; Weis, W. I.; Dunn, A. R. (2017): Vinculin forms a directionally asymmetric catch bond with F-actin. In *Science (New York, N.Y.)* 357 (6352), pp. 703–706. DOI: 10.1126/science.aan2556.

Humphries, J. D.; Wang, P.; Streuli, C.; Geiger, B.; Humphries, M. J.; Ballestrem, C. (2007): Vinculin controls focal adhesion formation by direct interactions with talin and actin. In *J Cell Biol* 179 (5), pp. 1043–1057. DOI: 10.1083/jcb.200703036.

Hüttelmaier, S.; Bubeck, P.; Rüdiger, M.; Jockusch, B. M. (1997): Characterization of two F-actin-binding and oligomerization sites in the cell-contact protein vinculin. In *European journal of biochemistry* 247 (3), pp. 1136–1142. DOI: 10.1111/j.1432-1033.1997.01136.x.

Hüttelmaier, S.; Illenberger, S.; Grosheva, I.; Rüdiger, M.; Singer, R. H.; Jockusch, B. M. (2001): Raver1, a dual compartment protein, is a ligand for PTB/hnRNPI and microfilament attachment proteins. In *J Cell Biol* 155 (5), pp. 775–786. DOI: 10.1083/jcb.200105044.

Huveneers, S.; Oldenburg, J.; Spanjaard, E.; van der Krogt, G.; Grigoriev, I.; Akhmanova, A. et al. (2012): Vinculin associates with endothelial VE-cadherin junctions to control force-dependent remodeling. In *J Cell Biol* 196 (5), pp. 641–652. DOI: 10.1083/jcb.201108120.

Hynes, R. O. (2002): Integrins: bidirectional, allosteric signaling machines. In *Cell* 110 (6), pp. 673–687. DOI: 10.1016/s0092-8674(02)00971-6.

Irianto, J.; Pfeifer, C. R.; Xia, Y.; Discher, D. E. (2016): SnapShot. Mechanosensing Matrix. In *Cell* 165 (7), 1820-1820.e1. DOI: 10.1016/j.cell.2016.06.002.

Jannie, K. M.; Ellerbroek, S. M.; Zhou, D. W.; Chen, S.; Crompton, D. J.; García, A. J.; DeMali, K. A. (2015): Vinculin-dependent actin bundling regulates cell migration and traction forces. In *The Biochemical journal* 465 (3), pp. 383–393. DOI: 10.1042/BJ20140872.

Janssen, M. E. W.; Kim, E.; Liu, H.; Fujimoto, L. M.; Bobkov, A.; Volkmann, N.; Hanein, D. (2006): Three-dimensional structure of vinculin bound to actin filaments. In *Mol Cell* 21 (2), pp. 271–281. DOI: 10.1016/j.molcel.2005.11.020.

Janssen, M. E. W.; Liu, H.; Volkmann, N.; Hanein, D. (2012): The C-terminal tail domain of metavinculin, vinculin's splice variant, severs actin filaments. In *J Cell Biol* 197 (5), pp. 585–593. DOI: 10.1083/jcb.201111046.

Johnson, R. P.; Craig, S. W. (1994): An intramolecular association between the head and tail domains of vinculin modulates talin binding. In *The Journal of biological chemistry* 269 (17), pp. 12611–12619.

Johnson, R. P.; Craig, S. W. (2000): Actin activates a cryptic dimerization potential of the vinculin tail domain. In *J Biol Chem* 275 (1), pp. 95–105. DOI: 10.1074/jbc.275.1.95.

Jurchenko, C.; Salaita, K. S. (2015): Lighting Up the Force: Investigating Mechanisms of Mechanotransduction Using Fluorescent Tension Probes. In *Molecular and cellular biology* 35 (15), pp. 2570–2582. DOI: 10.1128/MCB.00195-15.

Kanchanawong, P.; Shtengel, G.; Pasapera, A. M.; Ramko, E. B.; Davidson, M. W.; Hess, H. F.; Waterman, C. M. (2010): Nanoscale architecture of integrin-based cell adhesions. In *Nature* 468 (7323), pp. 580–584. DOI: 10.1038/nature09621.

Kanoldt, V.; Fischer, L.; Grashoff, C. (2019): Unforgettable force - crosstalk and memory of mechanosensitive structures. In *Biol Chem* 400 (6), pp. 687–698. DOI: 10.1515/hsz-2018-0328.

Kanoldt, V.; Kluger, C.; Barz, C.; Schweizer, A.-L.; Ramanujam, D.; Windgasse, L. et al. (2020): Metavinculin modulates force transduction in cell adhesion sites. In *Nat Commun* 11 (1), p. 6403. DOI: 10.1038/s41467-020-20125-z.

Kaushik, G.; Spenlehauer, A.; Sessions, A. O.; Trujillo, A. S.; Fuhrmann, A.; Fu, Z. et al. (2015): Vinculin network-mediated cytoskeletal remodeling regulates contractile function in the aging heart. In *Science translational medicine* 7 (292), 292ra99. DOI: 10.1126/scitranslmed.aaa5843.

Kim, L. Y.; Thompson, P. M.; Lee, H. T.; Pershad, M.; Campbell, S. L.; Alushin, G. M. (2016): The Structural Basis of Actin Organization by Vinculin and Metavinculin. In *Journal of molecular biology* 428 (1), pp. 10–25. DOI: 10.1016/j.jmb.2015.09.031.

Kioka, N.; Sakata, S.; Kawauchi, T.; Amachi, T.; Akiyama, S. K.; Okazaki, K. et al. (1999): Vinexin. a novel vinculin-binding protein with multiple SH3 domains enhances actin cytoskeletal organization. In *The Journal of cell biology* 144 (1), pp. 59–69. DOI: 10.1083/jcb.144.1.59.

Kirby, T. J.; Lammerding, J. (2018): Emerging views of the nucleus as a cellular mechanosensor. In *Nat Cell Biol* 20 (4), pp. 373–381. DOI: 10.1038/s41556-018-0038-y.

Kluger, C. (2016): The role of metavinculin in molecular mechanotransduction. Ludwig-Maximilians-Universität München.

Kluger, C.; Braun, L.; Sedlak, S. M.; Pippig, D. A.; Bauer, M. S.; Miller, K. et al. (2020): Different Vinculin Binding Sites Use the Same Mechanism to Regulate Directional Force Transduction. In *Biophysical journal* 118 (6), pp. 1344–1356. DOI: 10.1016/j.bpj.2019.12.042.

Kostetskii, I.; Li, J.; Xiong, Y.; Zhou, R.; Ferrari, V. A.; Patel, V. V. et al. (2005): Induced deletion of the N-cadherin gene in the heart leads to dissolution of the intercalated disc structure. In *Circ Res* 96 (3), pp. 346–354. DOI: 10.1161/01.RES.0000156274.72390.2c.

Koteliansky, V. E.; Belkin, A. M.; Frid, M. G.; Glukhova, M. A. (1991): Developmental changes in expression of adhesion-mediating proteins in human aortic smooth muscle. In *Biochemical Society transactions* 19 (4), pp. 1072–1076. DOI: 10.1042/bst0191072.

Koteliansky, V. E.; Ogryzko, E. P.; Zhidkova, N. I.; Weller, P. A.; Critchley, D. R.; Vancompernolle, K. et al. (1992): An additional exon in the human vinculin gene specifically encodes meta-vinculin-specific difference peptide. Cross-species comparison reveals variable and conserved motifs in the meta-vinculin insert. In *European journal of biochemistry* 205 (3), p. 1218. DOI: 10.1111/j.1432-1033.1992.tb16893.x_3.

Kroemker, M.; Rüdiger, A. H.; Jockusch, B. M.; Rüdiger, M. (1994): Intramolecular interactions in vinculin control alpha-actinin binding to the vinculin head. In *FEBS letters* 355 (3), pp. 259–262. DOI: 10.1016/0014-5793(94)01216-4.

Kumar, A.; Ouyang, M.; van den Dries, K.; McGhee, E. J.; Tanaka, K.; Anderson, M. D. et al. (2016): Talin tension sensor reveals novel features of focal adhesion force transmission and mechanosensitivity. In *J Cell Biol* 213 (3), pp. 371–383. DOI: 10.1083/jcb.201510012.

Kuo, S. C.; Sheetz, M. P. (1993): Force of single kinesin molecules measured with optical tweezers. In *Science (New York, N.Y.)* 260 (5105), pp. 232–234. DOI: 10.1126/science.8469975.

Kuriyama, S.; Theveneau, E.; Benedetto, A.; Parsons, M.; Tanaka, M.; Charras, G. et al. (2014): In vivo collective cell migration requires an LPAR2-dependent increase in tissue fluidity. In *J Cell Biol* 206 (1), pp. 113–127. DOI: 10.1083/jcb.201402093.

LaCroix, A. S.; Lynch, A. D.; Berginski, M. E.; Hoffman, B. D. (2018): Tunable molecular tension sensors reveal extension-based control of vinculin loading. In *Elife* 7. DOI: 10.7554/eLife.33927.

Lagendijk, A. K.; Gomez, G. A.; Baek, S.; Hesselson, D.; Hughes, W. E.; Paterson, S. et al. (2017): Live imaging molecular changes in junctional tension upon VE-cadherin in zebrafish. In *Nat Commun* 8 (1), p. 1402. DOI: 10.1038/s41467-017-01325-6.

Lakowicz, J. R. (2006): Principles of Fluorescence Spectroscopy. 3rd ed. Boston, MA: Springer US.

Le, S.; Yu, M.; Yan, J. (2019): Direct single-molecule quantification reveals unexpectedly high mechanical stability of vinculin-talin/α-catenin linkages. In *Science advances* 5 (12), eaav2720. DOI: 10.1126/sciadv.aav2720.

Le Clainche, C.; Dwivedi, S. P.; Didry, D.; Carlier, M.-F. (2010): Vinculin is a dually regulated actin filament barbed end-capping and side-binding protein. In *J Biol Chem* 285 (30), pp. 23420–23432. DOI: 10.1074/jbc.M110.102830.

Le Duc, Q.; Shi, Q.; Blonk, I.; Sonnenberg, A.; Wang, N.; Leckband, D.; Rooij, J. de (2010): Vinculin potentiates E-cadherin mechanosensing and is recruited to actin-anchored sites within adherens junctions in a myosin II-dependent manner. In *J Cell Biol* 189 (7), pp. 1107–1115. DOI: 10.1083/jcb.201001149.

Lee, H. T.; Sharek, L.; O'Brien, E. T.; Urbina, F. L.; Gupton, S. L.; Superfine, R. et al. (2019): Vinculin and metavinculin exhibit distinct effects on focal adhesion properties, cell migration, and mechanotransduction. In *Plos One* 14 (9), e0221962. DOI: 10.1371/journal.pone.0221962.

Lee, J. H.; Rangarajan, E. S.; Vonrhein, C.; Bricogne, G.; Izard, T. (2012): The metavinculin tail domain directs constitutive interactions with raver1 and vinculin RNA. In *Journal of molecular biology* 422 (5), pp. 697–704. DOI: 10.1016/j.jmb.2012.06.015.

Lee, J. H.; Rangarajan, E. S.; Yogesha, S. D.; Izard, T. (2009): Raver1 interactions with vinculin and RNA suggest a feed-forward pathway in directing mRNA to focal adhesions. In *Structure (London, England : 1993)* 17 (6), pp. 833–842. DOI: 10.1016/j.str.2009.04.010.

Lee, S.; Otto, J. J. (1997): Vinculin and talin. kinetics of entry and exit from the cytoskeletal pool. In *Cell motility and the cytoskeleton* 36 (2), pp. 101–111. DOI: 10.1002/(sici)1097-0169(1997)36:2<101::Aid-cm1>3.0.Co;2-c.

Leerberg, J. M.; Gomez, G. A.; Verma, S.; Moussa, E. J.; Wu, S. K.; Priya, R. et al. (2014): Tension-sensitive actin assembly supports contractility at the epithelial zonula adherens. In *Curr Biol* 24 (15), pp. 1689–1699. DOI: 10.1016/j.cub.2014.06.028.

Lemke, S. B.; Weidemann, T.; Cost, A.-L.; Grashoff, C.; Schnorrer, F. (2019): A small proportion of Talin molecules transmit forces at developing muscle attachments in vivo. In *PLoS biology* 17 (3), e3000057. DOI: 10.1371/journal.pbio.3000057.

Levental, K. R.; Yu, H.; Kass, L.; Lakins, J. N.; Egeblad, M.; Erler, J. T. et al. (2009): Matrix crosslinking forces tumor progression by enhancing integrin signaling. In *Cell* 139 (5), pp. 891–906. DOI: 10.1016/j.cell.2009.10.027.

Li, F.; Chen, A.; Reeser, A.; Wang, Y.; Fan, Y.; Liu, S. et al. (2019): Vinculin Force Sensor Detects Tumor-Osteocyte Interactions. In *Scientific reports* 9 (1), p. 5615. DOI: 10.1038/s41598-019-42132-x.

Li, R.; Narici, M. V.; Erskine, R. M.; Seynnes, O. R.; Rittweger, J.; Pišot, R. et al. (2013): Costamere remodeling with muscle loading and unloading in healthy young men. In *Journal of anatomy* 223 (5), pp. 525–536. DOI: 10.1111/joa.12101.

Ling, K.; Schill, N. J.; Wagoner, M. P.; Sun, Y.; Anderson, R. A. (2006): Movin' on up: the role of PtdIns(4,5)P(2) in cell migration. In *Trends Cell Biol* 16 (6), pp. 276–284. DOI: 10.1016/j.tcb.2006.03.007.

Lipfert, J.; Kerssemakers, J. W. J.; Jager, T.; Dekker, N. H. (2010): Magnetic torque tweezers: measuring torsional stiffness in DNA and RecA-DNA filaments. In *Nat Methods* 7 (12), pp. 977–980. DOI: 10.1038/nmeth.1520.

Livak, K. J.; Schmittgen, T. D. (2001): Analysis of relative gene expression data using real-time quantitative PCR and the 2(-Delta Delta C(T)) Method. In *Methods (San Diego, Calif.)* 25 (4), pp. 402–408. DOI: 10.1006/meth.2001.1262.

Lombardi, M. L.; Jaalouk, D. E.; Shanahan, C. M.; Burke, B.; Roux, K. J.; Lammerding, J. (2011): The Interaction between Nesprins and Sun Proteins at the Nuclear Envelope Is Critical for Force Transmission between the Nucleus and Cytoskeleton. In *J Biol Chem* 286 (30), pp. 26743–26753. DOI: 10.1074/jbc.M111.233700.

Maeda, M.; Holder, E.; Lowes, B.; Valent, S.; Bies, R. D. (1997): Dilated cardiomyopathy associated with deficiency of the cytoskeletal protein metavinculin. In *Circulation* 95 (1), pp. 17–20. DOI: 10.1161/01.cir.95.1.17.

Magid, A.; Law, D. J. (1985): Myofibrils bear most of the resting tension in frog skeletal muscle. In *Science (New York, N.Y.)* 230 (4731), pp. 1280–1282. DOI: 10.1126/science.4071053.

Majkut, S.; Dingal, P C Dave P; Discher, D. E. (2014): Stress sensitivity and mechanotransduction during heart development. In *Curr Biol* 24 (10), R495-501. DOI: 10.1016/j.cub.2014.04.027.

Majkut, S.; Idema, T.; Swift, J.; Krieger, C.; Liu, A.; Discher, D. E. (2013): Heart-specific stiffening in early embryos parallels matrix and myosin expression to optimize beating. In *Curr Biol* 23 (23), pp. 2434–2439. DOI: 10.1016/j.cub.2013.10.057.

Mandai, K.; Nakanishi, H.; Satoh, A.; Takahashi, K.; Satoh, K.; Nishioka, H. et al. (1999): Ponsin/SH3P12. an l-afadin- and vinculin-binding protein localized at cell-cell and cell-matrix adherens junctions. In *The Journal of cell biology* 144 (5), pp. 1001–1017. DOI: 10.1083/jcb.144.5.1001.

Manring, H. R.; Dorn, L. E.; Ex-Willey, A.; Accornero, F.; Ackermann, M. A. (2018): At the heart of inter- and intracellular signaling: the intercalated disc. In *Biophys Rev* 10 (4), pp. 961–971. DOI: 10.1007/s12551-018-0430-7.

Manso, A. M.; Li, R.; Monkley, S. J.; Cruz, N. M.; Ong, S.; Lao, D. H. et al. (2013): Talin1 has unique expression versus talin 2 in the heart and modifies the hypertrophic response to pressure overload. In *J Biol Chem* 288 (6), pp. 4252–4264. DOI: 10.1074/jbc.M112.427484.

Manso, A. M.; Okada, H.; Sakamoto, F. M.; Moreno, E.; Monkley, S. J.; Li, R. et al. (2017): Loss of mouse cardiomyocyte talin-1 and talin-2 leads to β-1 integrin reduction, costameric instability, and dilated cardiomyopathy. In *Proceedings of the National Academy of Sciences of the United States of America* 114 (30), E6250-E6259. DOI: 10.1073/pnas.1701416114.

Martinac, B. (2011): Bacterial Mechanosensitive Channels as a Paradigm for Mechanosensory Transduction. In *Cell Physiol Biochem* 28 (6), pp. 1051–1060. DOI: 10.1159/000335842.

McCain, M. L.; Parker, K. K. (2011): Mechanotransduction: the role of mechanical stress, myocyte shape, and cytoskeletal architecture on cardiac function. In *Pflugers Archiv : European journal of physiology* 462 (1), pp. 89–104. DOI: 10.1007/s00424-011-0951-4.

Milani-Nejad, N.; Janssen, P. M. L. (2014): Small and large animal models in cardiac contraction research: advantages and disadvantages. In *Pharmacology & therapeutics* 141 (3), pp. 235–249. DOI: 10.1016/j.pharmthera.2013.10.007.

Moiseyeva, E. P.; Weller, P. A.; Zhidkova, N. I.; Corben, E. B.; Patel, B.; Jasinska, I. et al. (1993): Organization of the human gene encoding the cytoskeletal protein vinculin and the sequence of the vinculin promoter. In *The Journal of biological chemistry* 268 (6), pp. 4318–4325.

Monkley, S. J.; Pritchard, C. A.; Critchley, D. R. (2001): Analysis of the mammalian talin2 gene TLN2. In *Biochem Bioph Res Co* 286 (5), pp. 880–885. DOI: 10.1006/bbrc.2001.5497.

Monkley, S. J.; Zhou, X. H.; Kinston, S. J.; Giblett, S. M.; Hemmings, L.; Priddle, H. et al. (2000): Disruption of the talin gene arrests mouse development at the gastrulation stage. In *Developmental dynamics : an official publication of the American Association of Anatomists* 219 (4), pp. 560–574. DOI: 10.1002/1097-0177(2000)9999:9999<::AID-DVDY1079>3.0.CO;2-Y.

Mueller, J.; Szep, G.; Nemethova, M.; Vries, I. de; Lieber, A. D.; Winkler, C. et al. (2017): Load Adaptation of Lamellipodial Actin Networks. In *Cell* 171 (1), 188-200 e16. DOI: 10.1016/j.cell.2017.07.051.

Neuman, K. C.; Nagy, A. (2008): Single-molecule force spectroscopy: optical tweezers, magnetic tweezers and atomic force microscopy. In *Nat Methods* 5 (6), pp. 491–505. DOI: 10.1038/nmeth.1218.

Nordenfelt, P.; Elliott, H. L.; Springer, T. A. (2016): Coordinated integrin activation by actin-dependent force during T-cell migration. In *Nat Commun* 7, p. 13119. DOI: 10.1038/ncomms13119.

Olson, T. M.; Illenberger, S.; Kishimoto, N. Y.; Huttelmaier, S.; Keating, M. T.; Jockusch, B. M. (2002): Metavinculin mutations alter actin interaction in dilated cardiomyopathy. In *Circulation* 105 (4), pp. 431–437. DOI: 10.1161/hc0402.102930.

Orr, A. W.; Helmke, B. P.; Blackman, B. R.; Schwartz, M. A. (2006): Mechanisms of mechanotransduction. In *Developmental cell* 10 (1), pp. 11–20. DOI: 10.1016/j.devcel.2005.12.006.

Oztug Durer, Z. A.; McGillivary, R. M.; Kang, H.; Elam, W. A.; Vizcarra, C. L.; Hanein, D. et al. (2015): Metavinculin Tunes the Flexibility and the Architecture of Vinculin-Induced Bundles of Actin Filaments. In *Journal of molecular biology* 427 (17), pp. 2782–2798. DOI: 10.1016/j.jmb.2015.07.005.

Pardo, J. V.; Siliciano, J. D.; Craig, S. W. (1983): A vinculin-containing cortical lattice in skeletal muscle: transverse lattice elements ("costameres") mark sites of attachment between myofibrils and sarcolemma. In *Proceedings of the National Academy of Sciences of the United States of America* 80 (4), pp. 1008–1012. DOI: 10.1073/pnas.80.4.1008.

Pasapera, A. M.; Schneider, I. C.; Rericha, E.; Schlaepfer, D. D.; Waterman, C. M. (2010): Myosin II activity regulates vinculin recruitment to focal adhesions through FAK-mediated paxillin phosphorylation. In *J Cell Biol* 188 (6), pp. 877–890. DOI: 10.1083/jcb.200906012.

Pennekamp, P.; Menchen, T.; Dworniczak, B.; Hamada, H. (2015): Situs inversus and ciliary abnormalities: 20 years later, what is the connection? In *Cilia* 4 (1), p. 1. DOI: 10.1186/s13630-014-0010-9.

Price, A. J.; Cost, A.-L.; Ungewiß, H.; Waschke, J.; Dunn, A. R.; Grashoff, C. (2018): Mechanical loading of desmosomes depends on the magnitude and orientation of external stress. In *Nat Commun* 9 (1), p. 5284. DOI: 10.1038/s41467-018-07523-0.

Puranam, Ishaan; Urs, Aarti; Kirk, Brenna; Newell-Litwa, Karen A.; Hoffman, Brenton (2019): A Molecular Tension Sensor for N-Cadherin Reveals Distinct Forms of Mechanosensitive Adhesion Assembly in Adherens and Synaptic Junctions: Cold Spring Harbor Laboratory.

Radice, G. L.; Rayburn, H.; Matsunami, H.; Knudsen, K. A.; Takeichi, M.; Hynes, R. O. (1997): Developmental defects in mouse embryos lacking N-cadherin. In *Developmental biology* 181 (1), pp. 64–78. DOI: 10.1006/dbio.1996.8443.

Rangarajan, E. S.; Izard, T. (2012): The cytoskeletal protein α-catenin unfurls upon binding to vinculin. In *J Biol Chem* 287 (22), pp. 18492–18499. DOI: 10.1074/jbc.M112.351023.

Rangarajan, E. S.; Lee, J. H.; Yogesha, S. D.; Izard, T. (2010): A helix replacement mechanism directs metavinculin functions. In *Plos One* 5 (5), e10679. DOI: 10.1371/journal.pone.0010679.

Ringer, P.; Colo, G.; Fässler, R.; Grashoff, C. (2017a): Sensing the mechano-chemical properties of the extracellular matrix. In *Matrix Biol* 64, pp. 6–16. DOI: 10.1016/j.matbio.2017.03.004.

Ringer, P.; Weissl, A.; Cost, A. L.; Freikamp, A.; Sabass, B.; Mehlich, A. et al. (2017b): Multiplexing molecular tension sensors reveals piconewton force gradient across talin-1. In *Nat Methods* 14 (11), 1090-+. DOI: 10.1038/Nmeth.4431.

Ringer, P.; Weissl, A.; Cost, A. L.; Freikamp, A.; Sabass, B.; Mehlich, A. et al. (2017c): Multiplexing molecular tension sensors reveals piconewton force gradient across talin-1. In *Nat Methods* 14 (11), pp. 1090–1096. DOI: 10.1038/nmeth.4431.

Riveline, D.; Zamir, E.; Balaban, N. Q.; Schwarz, U. S.; Ishizaki, T.; Narumiya, S. et al. (2001): Focal contacts as mechanosensors. Externally applied local mechanical force induces growth of focal contacts by an mDia1-dependent and ROCK-independent mechanism. In *J Cell Biol* 153 (6), pp. 1175–1185. DOI: 10.1083/jcb.153.6.1175.

Roberts, G. C. K.; Critchley, D. R. (2009): Structural and biophysical properties of the integrin-associated cytoskeletal protein talin. In *Biophys Rev* 1 (2), pp. 61–69. DOI: 10.1007/s12551-009-0009-4.

Rockman, H. A.; Ross, R. S.; Harris, A. N.; Knowlton, K. U.; Steinhelper, M. E.; Field, L. J. et al. (1991): Segregation of atrial-specific and inducible expression of an atrial natriuretic factor transgene in an in vivo murine model of cardiac hypertrophy. In *Proceedings of the National Academy of Sciences of the United States of America* 88 (18), pp. 8277–8281. DOI: 10.1073/pnas.88.18.8277.

Rodríguez, C. I.; Buchholz, F.; Galloway, J.; Sequerra, R.; Kasper, J.; Ayala, R. et al. (2000): High-efficiency deleter mice show that FLPe is an alternative to Cre-loxP. In *Nature genetics* 25 (2), pp. 139–140. DOI: 10.1038/75973.

Rothenberg, K. E.; Scott, D. W.; Christoforou, N.; Hoffman, B. D. (2018): Vinculin Force-Sensitive Dynamics at Focal Adhesions Enable Effective Directed Cell Migration. In *Biophysical journal* 114 (7), pp. 1680–1694. DOI: 10.1016/j.bpj.2018.02.019.

Rubsam, M.; Broussard, J. A.; Wickstrom, S. A.; Nekrasova, O.; Green, K. J.; Niessen, C. M. (2017): Adherens Junctions and Desmosomes Coordinate Mechanics and Signaling to Orchestrate Tissue Morphogenesis and Function. An Evolutionary Perspective. In *Cold Spring Harb Perspect Biol*. DOI: 10.1101/cshperspect.a029207.

Rüdiger, M.; Korneeva, N.; Schwienbacher, C.; Weiss, E. E.; Jockusch, B. M. (1998): Differential actin organization by vinculin isoforms: implications for cell type-specific microfilament anchorage. In *FEBS letters* 431 (1), pp. 49–54. DOI: 10.1016/s0014-5793(98)00723-6.

Saga, S.; Hamaguchi, M.; Hoshino, M.; Kojima, K. (1985): Expression of meta-vinculin associated with differentiation of chicken embryonal muscle cells. In *Exp Cell Res* 156 (1), pp. 45–56. DOI: 10.1016/0014-4827(85)90260-5.

Sarkar, A.; Zhao, Y.; Wang, Y.; Wang, X. (2018): Force-activatable coating enables high-resolution cellular force imaging directly on regular cell culture surfaces. In *Physical biology* 15 (6), p. 65002. DOI: 10.1088/1478-3975/aac69d.

Sarker, M.; Lee, H. T.; Mei, L.; Krokhotin, A.; de Los Reyes, Santiago Espinosa; Yen, L. et al. (2019): Cardiomyopathy Mutations in Metavinculin Disrupt Regulation of Vinculin-Induced F-Actin Assemblies. In *Journal of molecular biology* 431 (8), pp. 1604–1618. DOI: 10.1016/j.jmb.2019.02.024.

Schindelin, J.; Arganda-Carreras, I.; Frise, E.; Kaynig, V.; Longair, M.; Pietzsch, T. et al. (2012): Fiji: an open-source platform for biological-image analysis. In *Nat Methods* 9 (7), pp. 676–682. DOI: 10.1038/nmeth.2019.

Schwartz, M. A.; Assoian, R. K. (2001): Integrins and cell proliferation: regulation of cyclin-dependent kinases via cytoplasmic signaling pathways. In *J Cell Sci* 114 (Pt 14), pp. 2553–2560.

Senetar, M. A.; Moncman, C. L.; McCann, R. O. (2007): Talin2 is induced during striated muscle differentiation and is targeted to stable adhesion complexes in mature muscle. In *Cell motility and the cytoskeleton* 64 (3), pp. 157–173. DOI: 10.1002/cm.20173.

Sequeira, V.; Nijenkamp, Louise L A M; Regan, J. A.; van der Velden, J. (2014): The physiological role of cardiac cytoskeleton and its alterations in heart failure. In *Biochimica et biophysica acta* 1838 (2), pp. 700–722. DOI: 10.1016/j.bbamem.2013.07.011.

Shai, S.-Y.; Harpf, A. E.; Babbitt, C. J.; Jordan, M. C.; Fishbein, M. C.; Chen, J. et al. (2002): Cardiac myocyte-specific excision of the beta1 integrin gene results in myocardial fibrosis and cardiac failure. In *Circ Res* 90 (4), pp. 458–464. DOI: 10.1161/hh0402.105790.

Sheikh, F.; Chen, Y.; Liang, X.; Hirschy, A.; Stenbit, A. E.; Gu, Y. et al. (2006): alpha-E-catenin inactivation disrupts the cardiomyocyte adherens junction, resulting in cardiomyopathy and susceptibility to wall rupture. In *Circulation* 114 (10), pp. 1046–1055. DOI: 10.1161/CIRCULATIONAHA.106.634469.

Shen, K.; Tolbert, C. E.; Guilluy, C.; Swaminathan, V. S.; Berginski, M. E.; Burridge, K. et al. (2011): The vinculin C-terminal hairpin mediates F-actin bundle formation, focal adhesion, and cell mechanical properties. In *J Biol Chem* 286 (52), pp. 45103–45115. DOI: 10.1074/jbc.M111.244293.

Stephens, L. E.; Sutherland, A. E.; Klimanskaya, I. V.; Andrieux, A.; Meneses, J.; Pedersen, R. A.; Damsky, C. H. (1995): Deletion of beta 1 integrins in mice results in inner cell mass failure and peri-implantation lethality. In *Genes & development* 9 (15), pp. 1883–1895. DOI: 10.1101/gad.9.15.1883.

Sun, Z.; Guo, S. S.; Fässler, R. (2016): Integrin-mediated mechanotransduction. In *J Cell Biol* 215 (4), pp. 445–456. DOI: 10.1083/jcb.201609037.

Swift, S.; Lorens, J.; Achacoso, P.; Nolan, G. P. (2001): Rapid production of retroviruses for efficient gene delivery to mammalian cells using 293T cell-based systems. In *Current protocols in immunology* Chapter 10, Unit 10.17C. DOI: 10.1002/0471142735.im1017cs31.

Tao, H.; Zhu, M.; Lau, K.; Whitley, O. K. W.; Samani, M.; Xiao, X. et al. (2019): Oscillatory cortical forces promote three dimensional cell intercalations that shape the murine mandibular arch. In *Nat Commun* 10 (1), p. 1703. DOI: 10.1038/s41467-019-09540-z.

Theodosiou, M.; Widmaier, M.; Böttcher, R. T.; Rognoni, E.; Veelders, M.; Bharadwaj, M. et al. (2016): Kindlin-2 cooperates with talin to activate integrins and induces cell spreading by directly binding paxillin. In *Elife* 5, e10130. DOI: 10.7554/eLife.10130.

Thievessen, I.; Thompson, P. M.; Berlemont, S.; Plevock, K. M.; Plotnikov, S. V.; Zemljic-Harpf, A. et al. (2013): Vinculin-actin interaction couples actin retrograde flow to focal adhesions, but is dispensable for focal adhesion growth. In *J Cell Biol* 202 (1), pp. 163–177. DOI: 10.1083/jcb.201303129.

Thomas, W. A.; Boscher, C.; Chu, Y.-S.; Cuvelier, D.; Martinez-Rico, C.; Seddiki, R. et al. (2013): α-Catenin and vinculin cooperate to promote high E-cadherin-based adhesion strength. In *J Biol Chem* 288 (7), pp. 4957–4969. DOI: 10.1074/jbc.M112.403774.

Thompson, P. M.; Tolbert, C. E.; Campbell, S. L. (2013): Vinculin and metavinculin: oligomerization and interactions with F-actin. In *FEBS letters* 587 (8), pp. 1220–1229. DOI: 10.1016/j.febslet.2013.02.042.

Thompson, P. M.; Tolbert, C. E.; Shen, K.; Kota, P.; Palmer, S. M.; Plevock, K. M. et al. (2014): Identification of an actin binding surface on vinculin that mediates mechanical cell and focal adhesion properties. In *Structure (London, England : 1993)* 22 (5), pp. 697–706. DOI: 10.1016/j.str.2014.03.002.

Thoss, F.; Dietrich, F.; Punkt, K.; Illenberger, S.; Rottner, K.; Himmel, M.; Ziegler, W. H. (2013): Metavinculin: New insights into functional properties of a muscle adhesion protein. In *Biochem Bioph Res Co* 430 (1), pp. 7–13. DOI: 10.1016/j.bbrc.2012.11.013.

Twiss, F.; Le Duc, Q.; van der Horst, S.; Tabdili, H.; van der Krogt, G.; Wang, N. et al. (2012): Vinculin-dependent Cadherin mechanosensing regulates efficient epithelial barrier formation. In *Biology open* 1 (11), pp. 1128–1140. DOI: 10.1242/bio.20122428.

Vasile, V. C.; Will, M. L.; Ommen, S. R.; Edwards, W. D.; Olson, T. M.; Ackerman, M. J. (2006): Identification of a metavinculin missense mutation, R975W, associated with both hypertrophic and dilated cardiomyopathy. In *Molecular genetics and metabolism* 87 (2), pp. 169–174. DOI: 10.1016/j.ymgme.2005.08.006.

Vreeker, A.; van Stuijvenberg, L.; Hund, T. J.; Mohler, P. J.; Nikkels, P. G. J.; van Veen, Toon A B (2014): Assembly of the cardiac intercalated disk during pre- and postnatal development of the human heart. In *Plos One* 9 (4), e94722. DOI: 10.1371/journal.pone.0094722.

Wallrabe, H.; Periasamy, A. (2005): Imaging protein molecules using FRET and FLIM microscopy. In *Current opinion in biotechnology* 16 (1), pp. 19–27. DOI: 10.1016/j.copbio.2004.12.002.

Weiss, E. E.; Kroemker, M.; Rüdiger, A. H.; Jockusch, B. M.; Rüdiger, M. (1998): Vinculin is part of the cadherin-catenin junctional complex. complex formation between alpha-catenin and vinculin. In *The Journal of cell biology* 141 (3), pp. 755–764. DOI: 10.1083/jcb.141.3.755.

Wen, K.-K.; Rubenstein, P. A.; DeMali, K. A. (2009): Vinculin nucleates actin polymerization and modifies actin filament structure. In *J Biol Chem* 284 (44), pp. 30463–30473. DOI: 10.1074/jbc.M109.021295.

Witt, S.; Zieseniss, A.; Fock, U.; Jockusch, B. M.; Illenberger, S. (2004): Comparative biochemical analysis suggests that vinculin and metavinculin cooperate in muscular adhesion sites. In *The Journal of biological chemistry* 279 (30), pp. 31533–31543. DOI: 10.1074/jbc.M314245200.

Wood, C. K.; Turner, C. E.; Jackson, P.; Critchley, D. R. (1994): Characterisation of the paxillin-binding site and the C-terminal focal adhesion targeting sequence in vinculin. In *Journal of cell science* 107 (Pt 2), pp. 709–717.

Wozniak, M. A.; Chen, C. S. (2009): Mechanotransduction in development: a growing role for contractility. In *Nature reviews. Molecular cell biology* 10 (1), pp. 34–43. DOI: 10.1038/nrm2592.

Xia, T.; Liu, W.; Yang, L. (2017): A review of gradient stiffness hydrogels used in tissue engineering and regenerative medicine. In *Journal of biomedical materials research. Part A* 105 (6), pp. 1799–1812. DOI: 10.1002/jbm.a.36034.

Xu, W.; Baribault, H.; Adamson, E. D. (1998): Vinculin knockout results in heart and brain defects during embryonic development. In *Development (Cambridge, England)* 125 (2), pp. 327–337.

Yamada, S.; Pokutta, S.; Drees, F.; Weis, W. I.; Nelson, W. J. (2005): Deconstructing the cadherin-catenin-actin complex. In *Cell* 123 (5), pp. 889–901. DOI: 10.1016/j.cell.2005.09.020.

Yang, Z.; Bowles, N. E.; Scherer, S. E.; Taylor, M. D.; Kearney, D. L.; Ge, S. et al. (2006): Desmosomal dysfunction due to mutations in desmoplakin causes arrhythmogenic right ventricular

dysplasia/cardiomyopathy. In *Circ Res* 99 (6), pp. 646–655. DOI: 10.1161/01.RES.0000241482.19382.c6.

Yao, M.; Goult, B. T.; Chen, H.; Cong, P.; Sheetz, M. P.; Yan, J. (2014a): Mechanical activation of vinculin binding to talin locks talin in an unfolded conformation. In *Scientific reports* 4, p. 4610. DOI: 10.1038/srep04610.

Yao, M.; Qiu, W.; Liu, R.; Efremov, A. K.; Cong, P.; Seddiki, R. et al. (2014b): Force-dependent conformational switch of alpha-catenin controls vinculin binding. In *Nat Commun* 5, p. 4525. DOI: 10.1038/ncomms5525.

Yonemura, S.; Wada, Y.; Watanabe, T.; Nagafuchi, A.; Shibata, M. (2010): alpha-Catenin as a tension transducer that induces adherens junction development. In *Nat Cell Biol* 12 (6), 533-U35. DOI: 10.1038/ncb2055.

Zemljic-Harpf, A. E.; Miller, J. C.; Henderson, S. A.; Wright, A. T.; Manso, A. M.; Elsherif, L. et al. (2007): Cardiac-myocyte-specific excision of the vinculin gene disrupts cellular junctions, causing sudden death or dilated cardiomyopathy. In *Molecular and cellular biology* 27 (21), pp. 7522–7537. DOI: 10.1128/MCB.00728-07.

Zemljic-Harpf, A. E.; Ponrartana, S.; Avalos, R. T.; Jordan, M. C.; Roos, K. P.; Dalton, N. D. et al. (2004): Heterozygous inactivation of the vinculin gene predisposes to stress-induced cardiomyopathy. In *The American journal of pathology* 165 (3), pp. 1033–1044. DOI: 10.1016/S0002-9440(10)63364-0.

Zhao, G.; Qiu, Y.; Zhang, H. M.; Yang, D. (2019): Intercalated discs: cellular adhesion and signaling in heart health and diseases. In *Heart failure reviews* 24 (1), pp. 115–132. DOI: 10.1007/s10741-018-9743-7.

Ziegler, W. H.; Liddington, R. C.; Critchley, D. R. (2006): The structure and regulation of vinculin. In *Trends in cell biology* 16 (9), pp. 453–460. DOI: 10.1016/j.tcb.2006.07.004.